THESIS

PN TOMOGRAPHY AND TEMPERATURES OF SCANDINAVIA

Submitted by

Josh Watzak

Department of Geosciences

In partial fulfillment of the requirements

For the Degree of Master of Science

Colorado State University

Fort Collins, Colorado

Summer 2025

Master's Committee:

Advisor: Derek Schutt

Lisa Stright
Wolfgang Bangerth

ABSTRACT

PN TOMOGRAPHY AND TEMPERATURES OF SCANDINAVIA

We present a new high resolution tomographic study of the Scandinavian uppermost mantle from Pn traveltime tomography. This is accomplished by iteratively inverting for P-wave speeds using the Fast Marching Tomography package "FMTOMO", and using nearly 170,000 International Seismological Centre Pn picks as observational data. We map velocities to thermal structure derived from depth and temperature dependent metamorphic mineralogical variations of subcontinental lithospheric mantle. From resolution analysis, we achieve excellent raypath coverage and recovery of model structures at scales $2 \times 2^{\circ}$ or better. We present V_P and temperature results for the uppermost mantle at 60 and 70 km depths and find remarkable heterogeneity. In addressing the question of what sustains the enigmatic topography of the Scandes Mountains, we confirm the existence of low velocities beneath the southern Scandes and find elevated temperatures indicative of upper mantle dynamic support. Curiously, we also find similar high temperatures beneath the Lofoten Peninsula. However, for the northern Scandes, the dissimilar extent of elevated temperatures instead points towards shallower compensation of the topographic load, likely in the crust. We further validate the existence of a generally eastward thickening high density lower crustal layer from a pronounced low velocity ribbon we image beneath Finland. Our model's extent and resolution capabilities allow us to also identify thermal structures relating to the Cenozoic opening of the North Atlantic and Jurassic thermal doming in the North Sea.

ACKNOWLEDGEMENTS

Words seem an insufficient means of expressing my immense gratitude towards the people and support they provided me throughout my Master's project. But as with everything else, I will try my best. I would like to first thank my advisor Derek Schutt for believing in me and for always going the extra mile to provide me growth and learning opportunities. These past two years have meant a lot to me, and I am very proud of the work we could accomplish together. I would also like to express my sincerest gratitude to my committee member Lisa Stright, for constant moral support and for providing me with such incredible and unique experiences to explore my passion for teaching. I blossomed under your guidance. Thank you as well to my other committee member Wolfgang Bangerth for insightful conversations and for feedback that aided in the design of my project as part of the FRES group. Also, thank you to Nick Rawlinson for helping me to navigate FMTOMO. From our conversations, switches and dials (that now seem obvious to turn-on) made all the difference.

A big thank you to my lab mates Aziz, Sherif, and Tomalika. These past two years I have had the opportunity to learn and grow with y'all, and it has meant the world to me. Thank you too, to the people of the geoscience department for helping make CSU my home. The coffee hours, geojogs, and lunchroom banter has filled my life with joy. Thank you also to Warner College for providing support in the way of Scholarships. This project was also partially funded by NSF proposal EAR-1925595, thank you. Finally, I owe my biggest thanks to my partner Wesley. You have stood beside me and offered countless hours of selfless support by way of coffee, walks in the park, and late-night ice-cream runs. This journey would have been incomplete without you and our dog Apollo. Thank you.

TABLE OF CONTENTS

Chapter 1

1.1 Organization of Thesis

The following Master of Science Thesis is organized across six chapters and an appendix. In Chapter 1, we introduce the scope of the project as well as provide its motivation. For Chapter 2, we give further context for our study design by presenting an extended literature review of Scandinavia's tectonic background with geodynamics perspectives regarding modern topographic expression of the Scandes Mountains. From this context, in Chapter 3 we present methodology aimed at addressing questions raised in the motivations. This will cover both the theoretical background necessary to understand our chosen modeling approach and how we specifically achieve this in the Fast Marching Tomography package "FMTOMO" (Rawlinson & Urvoy, 2006). In Chapter 4, we present the inversion results for a new high-resolution tomographic study of Scandinavian lithosphere as well as quantify its thermal structure. We then provide qualification of the results by way of resolution tests and comparison with prior studies in Chapter 5. Also in Chapter 5, we interpret structures within their tectonic framework. Chapter 6 presents our final project conclusions and future work to be done. Following are appendices aimed at addressing initialization and troubleshooting of the sophisticated academic software FMTOMO. Finally, we include relevant codes written for this project and alluded to in the appendix documentation as well.

1.2 Project Scope and Motivation

The Scandinavian region located in Northern Europe and shown in the hemispheric base map of Figure 1.1, comprises the countries of Norway, Sweden, and Finland. We present a new high-resolution targeted study of the Scandinavian uppermost mantle with lateral extent denoted by the red bounds in Figure 1.1, and observational data used in the tomographic inversion by the burgundy. For context, all of our presented depth slices throughout this thesis correspond to these lateral extents.

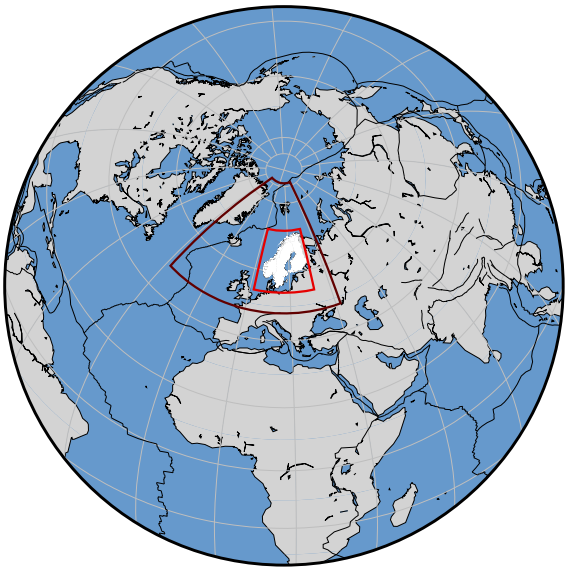

Figure 1.1: Hemisphere view of project area with tectonic boundaries overlain. Model/data bounds and final model presentation lateral extents are outlined by burgundy and red, respectively; Scandinavian countries are highlighted in white.

Motivation for understanding the Scandinavian lithosphere comes from its high topography in the Scandes Mountains (see Figure 1.2). Concentrated in northern and southern domes, elevations exceeding 2 km far from modern tectonic boundaries is contrary to areas of expected high topography. Moreover, a debate exists about the fate of the Scandes Mountains post orogenic formation with present elevations best described as enigmatic. This is best illustrated in Figure 1.3 reproduced from Ebbing (2007) with colored contours showing the theoretical depth of an Airy isostatic root needed to sustain the Scandes topographic load. The theoretical depth of the crustal root describes a surface in hydrostatic equilibrium with surrounding mantle material. Colored contour depths noticeably increase towards the west, beneath the Scandes. Black contours are overlain depicting Moho depths as measured by seismic methods which increase in depth towards the east, the interior of the craton. That these are different suggests Airy Isostasy is violated, and some other mechanism responsible for uplift. Much of the prior geophysical work has sought an explanation for the enigmatic topography of the Scandes Mountains, often invoking further characterization of the region's upper mantle as a mode of explanation. In the uppermost mantle, Scandinavian lithosphere exhibits remarkable seismic velocity changes, from low velocities beneath southern

Norway, to high velocities beneath Finland. Additionally, a review of geophysical investigations by Mauerberger et al. (2022) highlight significant lithospheric inhomogeneities even within lithosphere that is Archean in age. Temperatures are generally considered to be a primary modulator of upper mantle velocities and play an important role in both the forces that create tectonic deformation and the strengths that resist it. Thermal structure of the uppermost mantle is therefore a fundamental parameter we are looking to constrain.

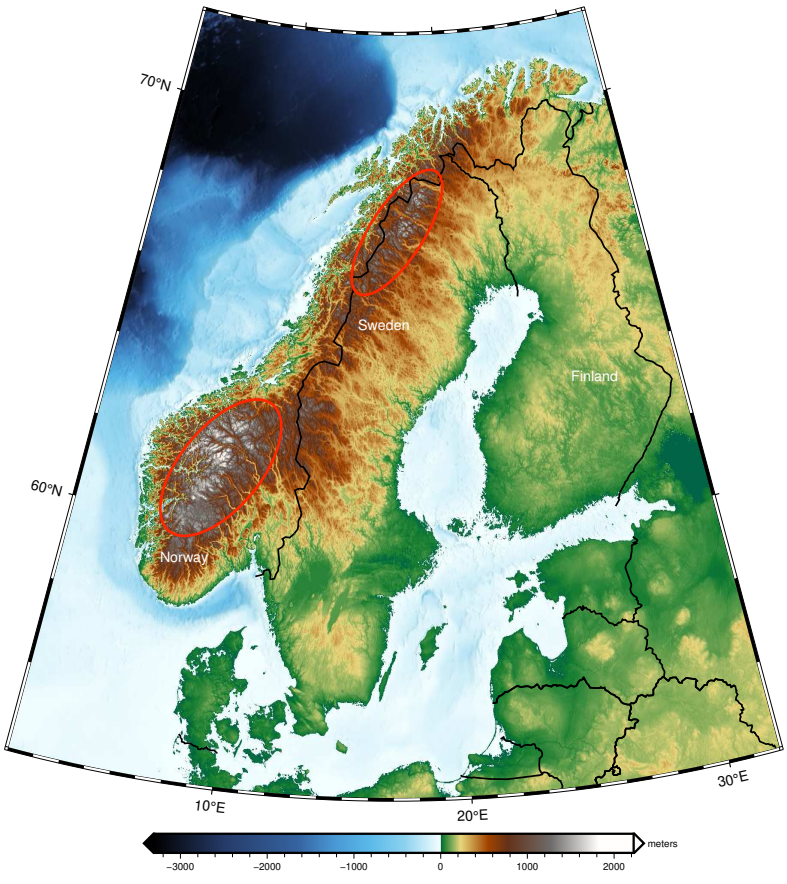

Figure 1.2: Topographic and bathymetric base map of Scandinavia; black lines denote political boundaries; red ovals outline the Scandes Mountains' northern and southern domes.

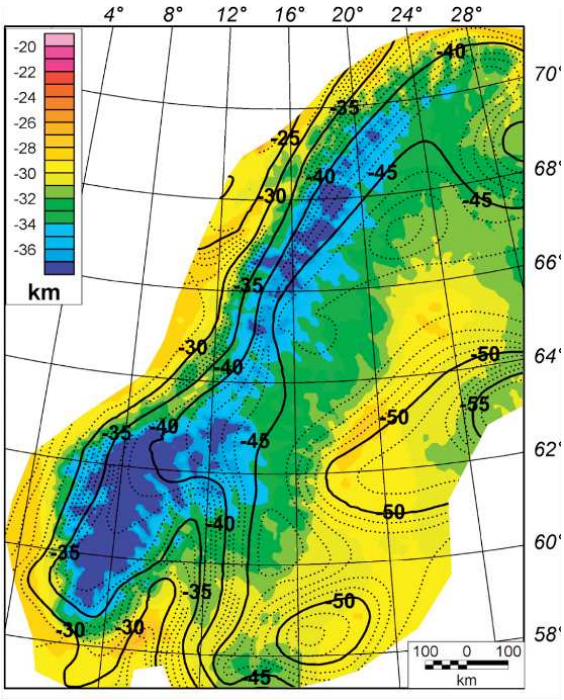

Figure 1.3: Airy isostatic depth to the Moho shown as colored contours with overlain seismic Moho depths as black contour intervals. Reprinted from Ebbing (2007, Figure 2a).

To investigate the thermal structure of Scandinavia's uppermost mantle, we perform high resolution Pn traveltime tomography using FMTOMO and convert inverted-for-velocities to temperatures. Pn tomography is quite well suited for imaging the uppermost mantle. The Pn wave originates in the crust, and travels as a head wave near the base of the Moho until it returns upwards and is recorded at a seismic station. Because Pn is nearly horizontal in the uppermost mantle, the steep vertical incidence of the wave is limited to the overlying crust and it can therefore resolve finer lateral scale structures in the uppermost mantle not imaged by other seismic phases. While many Pn studies assume Pn waves propagate along the base of the crust, FMTOMO's fast marching method of waveform tracing allows for depth dependent structure to be resolved.

We obtain results for both velocity and converted-temperature structures and present the depths of highest determined resolution, 60 and 70 km. We then interpret the velocity and thermal structure within the regional tectonic framework. This necessitates an understanding of the complex tectonic history of Scandinavia and modern geodynamic perspectives for sustained Scandes topography, which we cover in Chapter 2. The targeted depths we present in this study are an attempt

at reconciling a generous body of upper mantle work by connecting our higher resolution imagery about the base of the Moho with more coarsely resolved structures that extend to greater depths. With that goal in mind, our results are shown to further validate such prior work while providing new higher-order imaging of upper mantle heterogeneities. Furthermore, our temperature results with defined depths can provide a basis for future isostatic modeling aimed at addressing dynamic support of the Scandes Mountains.

Finally, because of the sophisticated nature of FMTOMO, we provide an exhaustive set of documentation that details implementing our inversions. These include common troubleshooting errors and clarifications not addressed in the package installation manual, and scripts easily adaptable for generating necessary FMTOMO read-in files. All of this makes for an interesting tomographic problem, one with an adaptable methodology for understanding lithospheres of other cratonic regions and other remnant fossil mountain chains.

Chapter 2

2.1 Introduction to Scandinavia Tectonics

Scandinavia sits along a modern passive margin but contains a complex tectonic history. Today, areas of elevation exceeding 2100 m and 2500 m can be found concentrated in its northern and southern domes (Mauerberger et al., 2022). Such high elevations far from a plate boundary oppose convention, though may be explained as either remnant from orogenesis or from dynamic support of the mantle (Maupin et al., 2013). Dynamic support from temperature-caused density variations would be capable of sustaining the Scandes topography. Further characterization of Scandinavia's lithosphere, with Pn tomography quite well suited for doing so, is necessary to more fully understand the geodynamic response of the region. Prior to that, we begin by presenting a literature review of most current understanding regarding Scandinavian tectonic background, upper mantle structures, and geodynamic perspectives.

In attempting to review more than 3 Ga of tectonic history, we give precedence to broad lithospheric points of view, i.e. arguments that can be extended to depths where Pn has resolving power. Additionally, the presented tectonic discussions are limited to scales regional in size to limit an already verbose chronology. It should also be noted that invoking modern plate tectonic processes that far back in time also requires a greater degree of generality. Figure 2.1 presents the modern crustal expression of the tectonic domains defined throughout this chapter.

2.2 Tectonic Background

This project aims to address uppermost lithospheric mantle structures beneath Scandinavia. *Fennoscandia* (alternatively, *Baltic Shield*) is the exposed Archean and Proterozoic crystalline basement of Scandinavia that also comprises the westernmost extent of the Eastern European Craton (EEC) (Figure 2.2). The Precambrian basement is largely Archean and Paleoproterozoic in age, generally trending younger towards the west (Gaál & Gorbatschev, 1987) (see Figure 2.1). A craton is the oldest and most stable part of a continent, often not experiencing deformation for

Figure 2.1: Tectonic base map; Geologic map of major tectonic domains with units defined in bottom right legend; after Högdahl et al. (2004), and prominent suture zones after Wylegalla et al. (1999) and Weidle and Maupin (2008). Political boundaries are denoted as black lines between countries. *CDF = Caledonian Deformation Front, CM = Continental Margin, ISZ = Iapetus Suture Zone, OG = Oslo Graben, ThorS = Thor Suture, STZ = Sorgenfrei-Tournquist Zone (the northeast extent of the Trans-European Suture Zone between the Precambrian Eastern European Craton and Phanerozoic western Europe).*

over a billion years. The term *Baltica* is most often used by the paleogeographic community and instead denotes Scandinavia and the EEC as a single cohesive continental block.

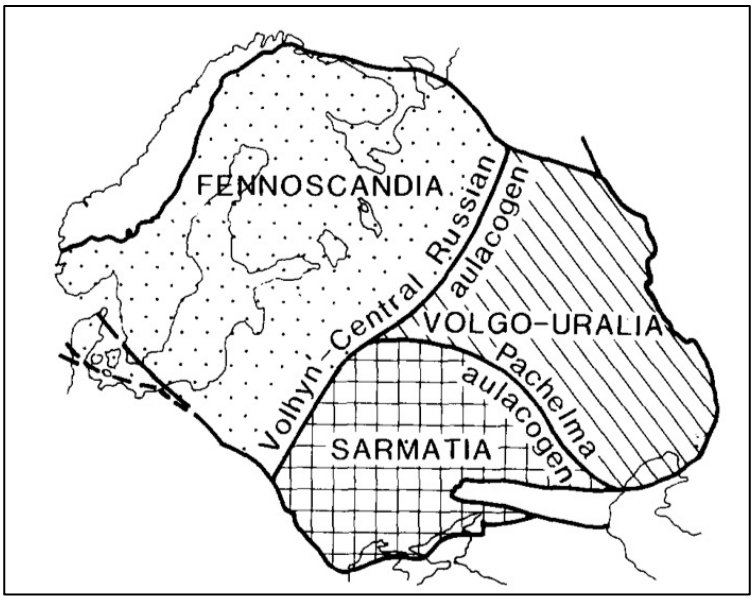

Figure 2.2: Outline of the Eastern European Craton (EEC). Reprinted from Gorbatschev and Bogdanova (1993, Figure 1).

The Archean domain, located in northern Finland and Sweden, is best summarized as a series of dispersed cratonic nuclei re-assembled in the Paleoproterozoic (Lahtinen et al., 2005; Figure 2.3). The Archean Province comprises some of the oldest material on Earth. It contains the Karelia craton (~3.5 Ga starting formation; Figure 2.1) which by Late Archean formed the relatively stable nucleus of proto-Baltica (Gorbatschev & Bogdanova, 1993). Following cratonization of Karelia as the proto-continent, an extensive and complex rifting period commenced ~2.5 – 2.1 Ga leading to its eventual breakup ~2.06 Ga (Gorbatschev & Bogdanova, 1993; Lahtinen et al., 2005). Along the craton's northeast boundary lies the Lapland-Kola mobile belt, a collisional orogeny between the cratons Karelia and Kola (Gorbatschev & Bogdanova, 1993). The Kola (now) peninsula is made of Archean blocks sutured together by belts of strongly deformed Proterozoic terranes (Gorbatschev & Bogdanova, 1993). Final docking of the Kola craton was later refined to ~1.91 Ga (Lahtinen & Huhma, 2019). The ~2.5 – 1.8 Ga complex evolutionary history of the Lapland-Kola mobile belt

affected Karelia by subduction related magmatism within the Inari region, and produced strong crustal reworking along the Belomorian (Lahtinen et al., 2005; Figure 2.3). The Belomorian is interpreted from crustal greenstone belts as an accreted island arc domain originating in the Archean along the Karelia margin (Gaál & Gorbatschev, 1987; Lahtinen et al., 2005). Greenstone belts are so-termed from their green-colored chlorite minerals produced by metamorphism of ocean sediment basins. Although affected by the Paleoproterozoic extensive rifting phases and coeval accretionary processes, the Karelia province remained relatively homogeneous (Lahtinen et al., 2005).

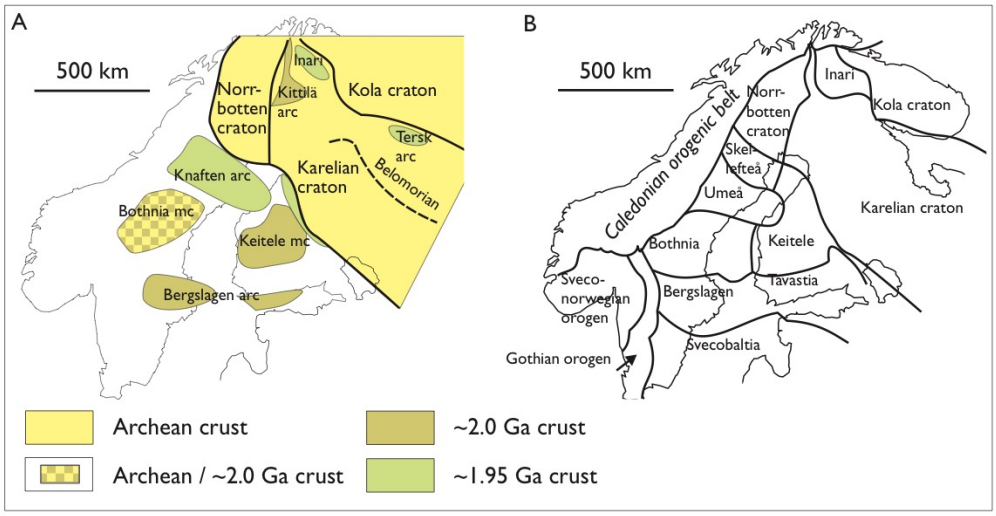

Figure 2.3: Major Proterozoic Terranes. "(A) Exposed and hidden pre-1.92 Ga components...; (B) Major geologic units with Paleoproterozoic and younger boundaries." Reprinted from Lahtinen et al. (2005, Figure 11.9); *"mc" = microcontinent*.

Lahtinen et al. (2005) also introduce an Archean in age Norbotton craton to the west of the Karelian (see Figure 2.3). East-to-west accretion of the Norbotton craton with Karelia occurred ~1.92 Ga (Lahtinen et al., 2005). To its east is a mega shear boundary, but the craton itself is covered by Proterozoic allochthonous supracrustal rocks (see Paleoproterozoic cover in Figure 2.1). Because there is no crustal exposure of the Norbotton craton, its existence is instead inferred from geophysical studies. Though Gorbatschev and Bogdanova (1993) also identify the shear zone as a marked boundary, they do not distinguish the Norbotton as a separate domain.

The Paleoproterozoic Svecofennian domain has classically been explained as an important crustal building episode. It was succeeded by orogenic collapse and stabilization, but largely completed Scandinavia's Precambrian basement construction (Gorbatschev and Bogdanova, 1993; Figure 2.1). The Svecofennian describes a semi-continuous period ~1.9 – 1.86 Ga of prolonged continental crust and island arc accretions (Gorbatschev & Bogdanova, 1993). Lahtinen et al. (2005) instead propose five distinct orogenic events spanning 1.92 – 1.75 Ga, partly coeval in time and space and operating at high angles to each other. More generally, the timeline of the province follows a microcontinent accretionary stage (1.92 – 1.87 Ga) and subsequent period of extension (1.86 – 1.84 Ga) (Lahtinen et al., 2005). Onset of continent-continent collision between Fennoscandia and Sarmatia occurred 1.84 – 1.79 Ga, docking the shield with the rest of the EEC (Lahtinen et al., 2005; Figure 2.2).

Regardless of specificities, the Paleoproterozoic was a period of unprecedented crustal growth for the Baltic Shield. Along its western margin, periodic subduction-related magmatism emplaced the north-south trending Transcandinavian Igneous Belt (TIB) ~1.83 – 1.65 Ga (Gorbatschev and Bogdanova, 1993; Figure 2.1). TIB granitoid plutons are easily identifiable in magnetic and heat production maps, and are constrained from isostatic and gravity modeling to depths above 12–20 km (Gradmann & Ebbing, 2015). Partly coeval with TIB emplacement was the final growth stage of the shield termed the Gothian evolution 1.75 – 1.55 Ga (Gorbatschev & Bogdanova, 1993). The Gothian domain has largely been overwritten by subsequent orogenic events (see Figure 2.3), but during its southwest growth of the shield it emplaced the Rapakivi granites far inland from its trench (Lahtinen et al., 2005; Figure 2.1). Cratonization of the Svecofennian province ~1.5 Ga completed the Scandinavian Precambrian basement (Gorbatschev & Bogdanova, 1993).

During the formation of Mesoproterozoic supercontinent Rodinia, southwestern Norway and southern Sweden were largely re-worked by collision with Laurentia and later Amazonia (Gaál & Gorbatschev, 1987). An aspect of Grenvillian evolution, the Sveconorwegian orogeny (~1.2 – 0.9 Ga) comprised an early and late-stage deformation maxima with deformation intensity increasing towards the collision in the west (Gaál and Gorbatschev, 1987; Gorbatschev and Bogdanova,

1993; Figure 2.4). Rotation of Baltica before final continental assembly resulted in the creation of two phases. Eventual collapse of the supercontinent led to the opening of the Iapetus Ocean whose subsequent closure (see "ISZ", Figure 2.1) marked the onset of one final orogenic event, the Caledonian.

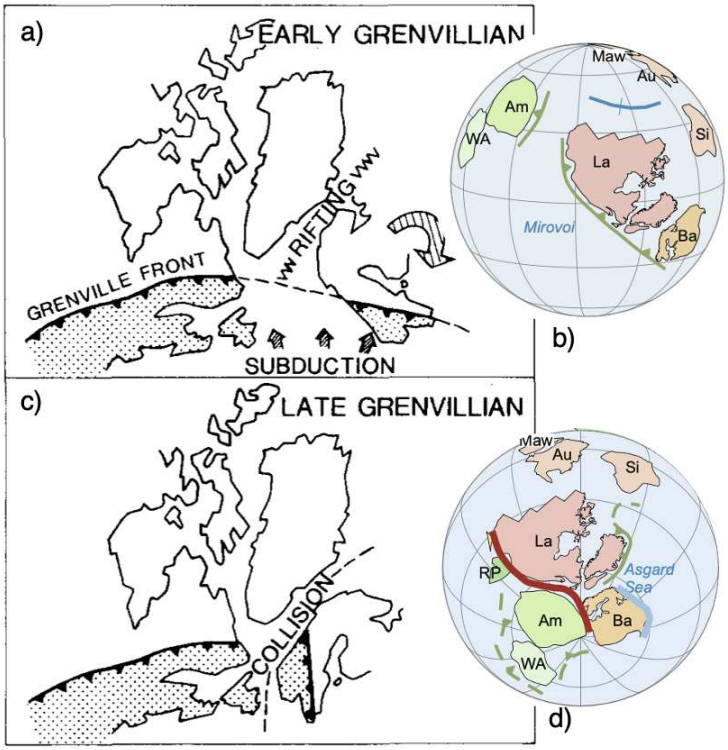

Figure 2.4: Sveconorwegian Orogeny early and late stages. (a,c) Reprinted from Gaál and Gorbatschev (1987, Figure 5) with hemisphere view. (b,d) Reprinted from Cawood and Pisarevsky (2017, Figures 1 and 2); (b,d) *Ba = Baltica, La = Laurentia, Am = Amazoina; (ignore other entries).*

The Caledonian Orogeny occurred from Late Cambrian through the Early Devonian across several stages of contraction/accretion, subduction, and eventual orogenic collapse (Roberts, 2003). The final orogenic stage, the Scandian event (420 - 400 Ma), saw rapid westward subduction of Baltica beneath Laurentia, and is largely responsible for the distribution of allochthonous nappe structures overlying Precambrian basement (Roberts, 2003; Figure 2.5). Gravitational collapse of the over thickened crust is in part responsible for, and coeval with, a period of extension defining the paleo-outline of the present Scandes Mountains (Roberts, 2003). Present topographic relief is

also marked by fjord-lands carved from repeated Neogene Ice ages (Smelror et al., 2007; Figure 1.2).

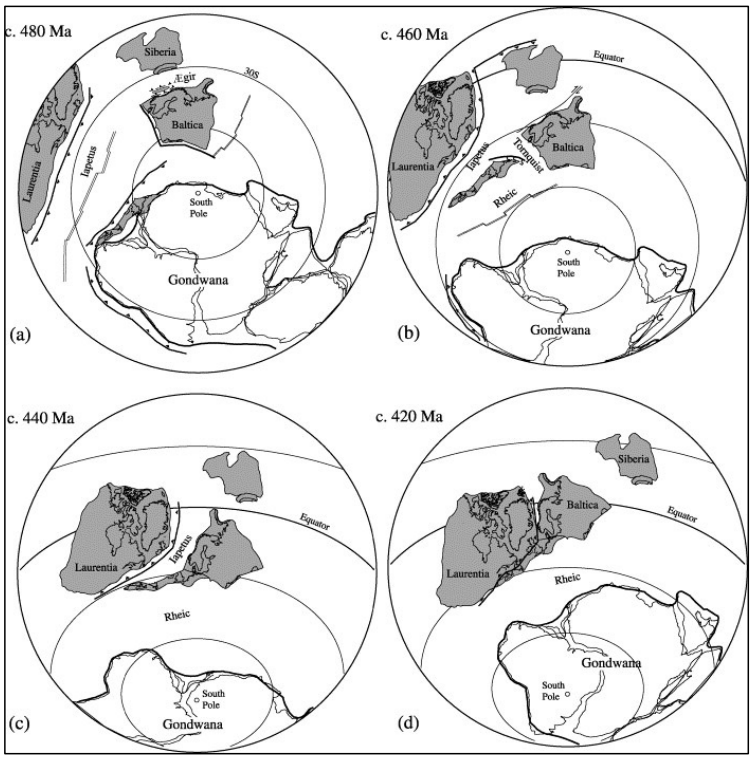

Figure 2.5: Paleogeographic reconstructions. Reprinted from Roberts (2003, Figure 3)

Additionally, an ~450 Ma collision to the south with Avalonia formed the Trans European Suture Zone (TESZ) from closure of the Tornquist Sea (Pharaoh et al., 1997). Avalonia is a Gondwana-derived microcontinent, that later with Gondwana itself, collided with Baltica during the formation of Pangaea (Pharaoh et al., 1997; Figure 2.5). The TESZ is a well-documented geophysical boundary separating relatively older, colder, and seismically faster Precambrian Baltica lithosphere with opposing characteristics of Phanerozoic Western Europe (Shomali et al., 2006). The Sorgenfrei-Tornquist Zone ("STZ", Figure 2.1) is the northwestern-most extension of the TESZ and has been active since its inception in response to regional tectonic stresses (Shomali et al., 2006). The STZ also connects at depth with the Thor Suture ("ThS", Figure 2.1), which has been related to the southward subduction of Baltica beneath Avalonia (Smit et al., 2016).

Regional rifting from gravitational collapse of the Caledonian continued into the Permian with the formation of the Oslo Graben and its associated magmatic intrusions (Neumann et al., 2004). This pattern of heating and extension continued throughout the Triassic, which by Late to Middle Jurassic developed active rifting in the North Sea driven by mantle-derived thermal doming (Underhill & Partington, 1993). The final tectonic event to affect Scandinavia was the Cenozoic opening of the North Atlantic Ocean. More recently, uplift of the Scandes has occurred and is especially pronounced across its northern and southern domes. Conventional understanding would dictate finding regions of highest topography at or near plate boundaries. Thus, a debate remains about the fate of Scandes topography from their orogenesis in the Caledonian through the modern.

2.3 The Scandes Enigmatic Topography

Enigmatic topographies of fossil mountains ranges, like the Scandes, may instead be explained as either remnant from prior orogenesis or due to epeirogeny (Maupin et al., 2013). A remnant topography would, as the term implies, persist to a degree of the heights achieved during mountain formation "orogenesis". Epeirogeny describes broad vertical uplift not associated with orogenesis, and is thus more related to contributions from the mantle; more on this later.

Arguments for remnant topography are generally understood within the "ICE" (isostasy, climate, and erosion) hypothesis synthesized by Nielsen et al. (2009). ICE describes a prolonged denudation of the Scandes Mountains since the Caledonian and argues that signals of uplift in the Neogene are instead attributable to an erosion driven exhumation of the Scandes. Moreover, ICE points to sediment fluxes responding to climatic variations (i.e., ice ages) as the exhuming agent. A significant exhumation event in the Neogene has been suggested from Apatite fission track analysis, though most attribute this to a true uplift signal (see Anell et al., 2009; Gabrielsen et al., 2005, for comprehensive reviews; Figure 2.6). Additionally, as Anell et al. (2009) argues, prolonged sustenance of mountainous topography would require a large crustal root for which the Scandes are lacking. Thus, with respect to principles of Airy Isostasy, the Scandes are considered enigmatic (see Figure 1.3).

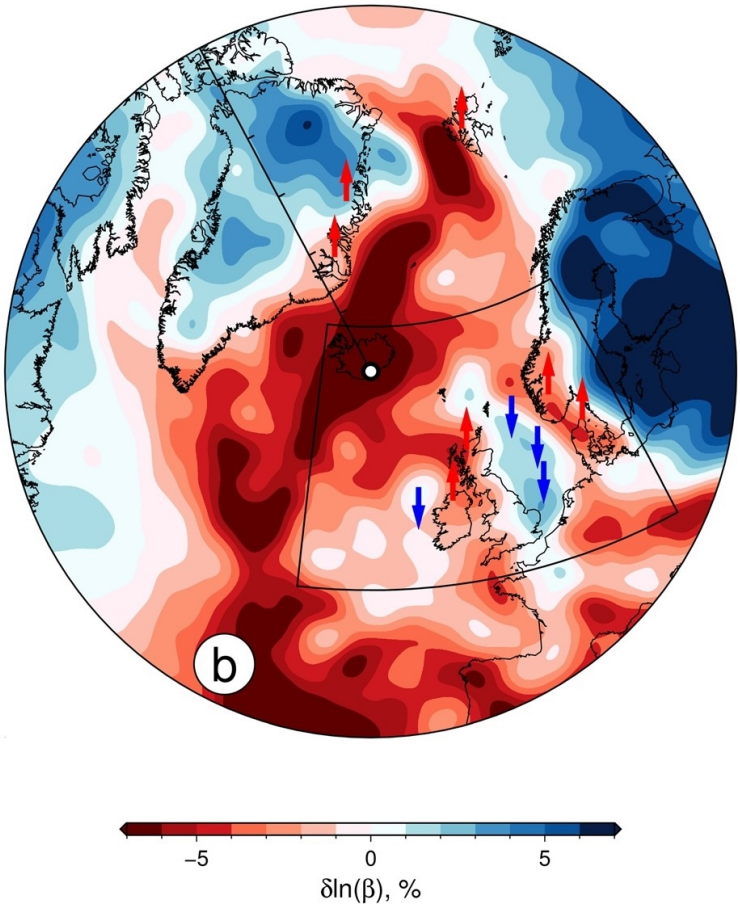

Figure 2.6: Neogene uplift/subsidence signals (arrows) overlaying relative shear wave velocities (color contours) at 150 km depth. Reprinted from Schoonman et al. (2017, Figure 1b).

Seminal work by Ebbing and Olesen (2005) performing gravity and geoid height modeling aimed to understand isostatic compensation of the Scandes at crustal and lithospheric depths. Their modeling results in the northern dome indicated compensation from crustal density variations in a mixed form of Airy-Pratt Isostasy (see also Gradmann and Ebbing, 2015; Ebbing et al., 2012 for review). For the southern dome, a 3D varying density model by Ebbing (2007) instead revealed the presence of a high-density lower crustal layer, generally eastward thickening, that tapers out beneath the southern Scandes in contrast to pure Airy Isostasy. This layer has also been independently found through seismic inversion methods (e.g., Korja et al., 1993; Mauerberger et al., 2022). Receiver functions and active source experiments do however reveal a crustal root as expected from Airy Isostasy (e.g., Stratford et al., 2009; Svenningsen et al., 2007), but only a minor one laterally offset ~50 km from the areas of highest topography.

The apparent lack of a pronounced crustal root supporting Scandes topography is more readily explained by low density material in the upper mantle providing dynamic support (Ebbing & Olesen, 2005; Maupin et al., 2013). The term "*dynamic support*" has a somewhat muddied definition, as Forte and Rowley (2022) point out that semantically mantle convection is inherently dynamic. Regardless, it describes thermal convective transport of less dense materials which act to support crustal topographic loads (Molnar et al., 2015). Moreover, a flat 410 discontinuity as imaged by Makushkina et al. (2019) implies a responsible mechanism to be found at shallower depths since the 410 discontinuity is thought to bow to greater depths if crossed by higher temperatures. Further characterization of the uppermost mantle, which Pn tomography is quite well suited for doing, is therefore likely to contribute greatly to a more complete understanding of the geodynamic response of the region.

Proposed mantle driven sources include asthenospheric diapirism, lithospheric delamination, magmatic underplating, thermal instability causing convection, and dynamic uplift (Anell et al., 2009). Following the asthenospheric diapirism model by Rohrman and van der Beek (1996), elevated asthenospheric temperatures from the Iceland plume interacting with cold cratonic lithosphere could produce diapirs from a Rayleigh-Taylor instability (Figure 2.7). This instability is the same phenomena as what produces thunderclouds between layers of warm/buoyant air and cold/-dense air (Rohrman & van der Beek, 1996). Moreover, the Cenozoic opening of the North Atlantic is well documented from plume activity by NAIP (North Atlantic Igneous Province) basalts now found across the ocean's conjugate margin (Saunders et al., 1997).

If sufficiently hot, lithospheric delamination or partial melt-producing magmatic underplating could occur (Anell et al., 2009; Figure 2.7). Delamination describes the removal of basal lithospheric material which if not impinged by hotter "more-buoyant" material would cause foundering/sinking. Underplating occurs when impinging magma bodies stall out during ascent due to density contrasts with the surrounding host rock. If emplaced near the base of the crust, this could provide isostatic compensation akin to an Airy-type root. Though as Anell et al. (2009) argue, there is a surprising lack of igneous activity in areas of significant uplift, and invoking the Iceland

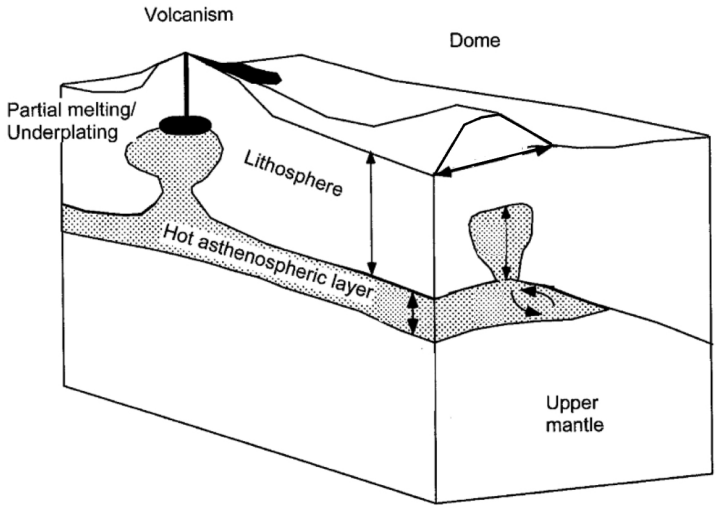

Figure 2.7: Asthenospheric diapirism model. Modified after Rohrman and van der Beek (1996, Figure 2).

Plume as the responsible thermal source is ~30 Myr temporally offset from effects caused during initial rifting.

Still, many global and regional shear wave models image a low velocity body extending from the Iceland plume to beneath the Scandes (e.g., Schaeffer and Lebedev, 2013; Weidle and Maupin, 2008; Figure 2.6). More recent work by Mauerberger et al. (2022) also suggests edge-driven convection in part responsible for sustaining the northern Scandes along with dynamic support in the southern. Edge-driven convection forms in response to discontinuities in the lithosphere affecting mantle flow and induces convective upwelling of hotter materials (King & Anderson, 1998). Mauerberger et al. (2022) identify lithospheric steps (sharp increases in thickness) roughly coincident with the Caledonian Deformation Front ("CDF", Figure 2.1).

Gabrielsen et al. (2005) present the opinion that support of the Scandes topography is likely a composite of multiple overprinting geodynamic processes resulting from its long and complex tectonic history. We address the question of what sustains the enigmatic topography of the Scandes by performing Pn traveltime tomography. Pn is capable of resolving finer scale uppermost mantle structures not imaged by other tomographic methods. Our project presents a targeted view of uppermost mantle structures, connecting already imaged deeper-seated structures to their potential geodynamic implications.

Chapter 3

3.1 Methods: Introduction to Traveltime Tomography

A traveltime tomography problem consists of inverting for velocity structure in an effort to satisfy some observational data. Though many different methods exist for achieving this, the underlying principle remains as satisfying the time it takes for seismic phases to arrive at recording stations by adjusting the medium through which they propagate. For example, a time-delayed phase arrival would indicate said ray propagating through a slower-velocity body with many crossing rays more clearly defining the body's shape and magnitude.

In this project we construct a tomographic image of Scandinavian uppermost mantle V_P structure from International Seismological Centre "ISC" observed Pn traveltimes. We accomplish this in the Fast Marching Tomography package "FMTOMO" by solving both the forward traveltime predictor and then iteratively inverting for velocity structure (Rawlinson & Urvoy, 2006). As shown in the FMTOMO concept design of Figure 3.1, we input observed ISC Pn picks and model (predict) the time it takes for them to travel through the velocity medium. We, in FMTOMO, then iteratively improve the velocity model by minimizing the time difference between our predicted and observed data. Once we achieve significant convergence between the two, we then convert inverted-for velocities to temperatures by way of compositional dependencies.

3.2 ISC Data

Pn traveltime picks we use as observational data in the tomographic inversion come from the ISC reviewed bulletin between 2006 and 2023. ISC-published traveltime data primarily consists of location and time for event hypocenters with corresponding station phase arrival times. We first process the ISC data through a series of culling procedures intended to identify physically reasonable Pn arrival times (Figure 3.2). Consistent with the definition of a first arriving Pn phase, we cull events to originating within the crust and at an epicentral distance of 1.8 – 15° (Kennett, 2005; Storchak et al., 2003). Originating in the crust, Pn travels as a head wave near the base of

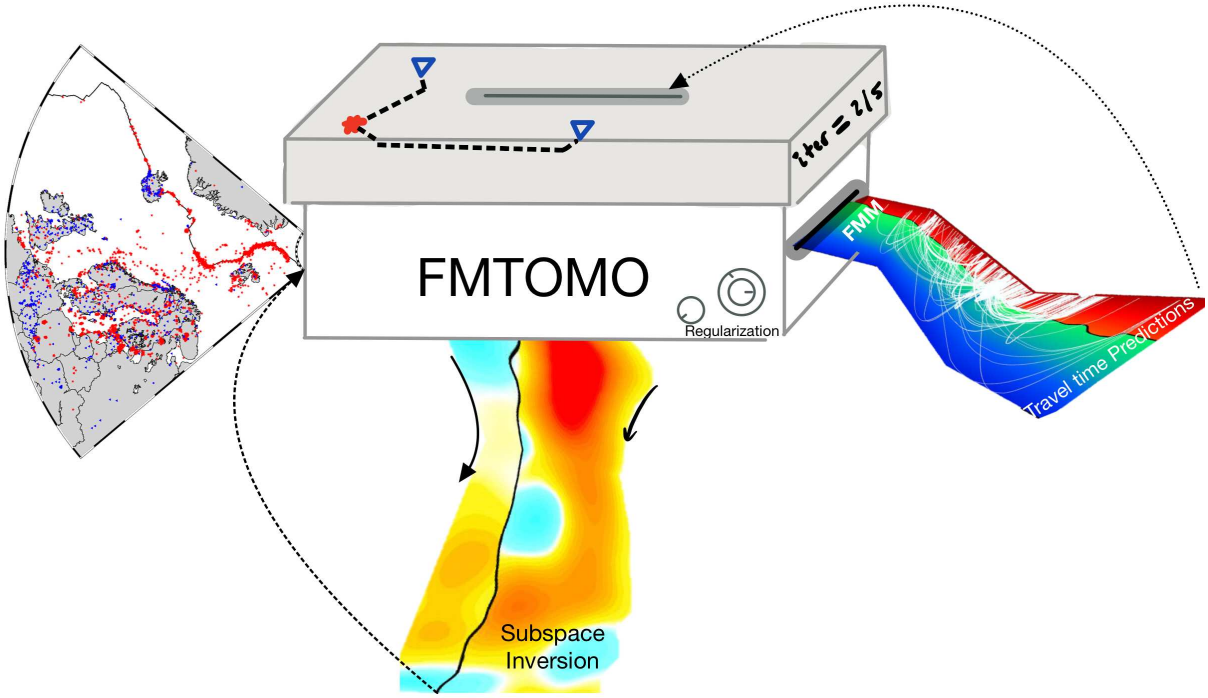

Figure 3.1: FMTOMO concept design. ISC traveltime data (red-events, blue-stations) enters from the left in the form of longitude, latitude, depth, and time. Event-station geometries are then prescribed as Pn path and forward modeled with the traveltime solver "FMM"; shown in right output, with colors corresponding to a simple velocity increase with depth and white raypaths. Predicted traveltimes are then used to update the initial reference model in the inversion; shown in bottom output with hot/cold colors corresponding to positive/negative velocity updates. The inversion is subject to regularization and is depicted by the nobs on the box. This iterative process (the "iter" count on the right side of the box) is repeated until we achieve a satisfactory convergence between observed and predicted traveltimes.

the Moho until velocity gradients cause it to return upwards. We use the Moho model by Grad et al. (2009) to maintain consistency across FMTOMO inputs (this is addressed more fully in section 3.3). Outside epicentral distances of 1.8 – 15°, the first arriving phase may be the crustal Pg-phase or mantle P-phase which would be inaccurate as a Pn-path traveltime (Kennett, 2005). Moreover, we constrain traveltime residuals to 6 seconds about a best fit line (Figure 3.2-insert), and set event-station recordings greater than 5 to mitigate any impact from spurious picks. Finally, we note that our chosen data constraints are consistent with other regional Pn tomographic studies (e.g., Buehler and Shearer, 2010; Hearn et al., 1991; Sun and Kennett, 2016a).

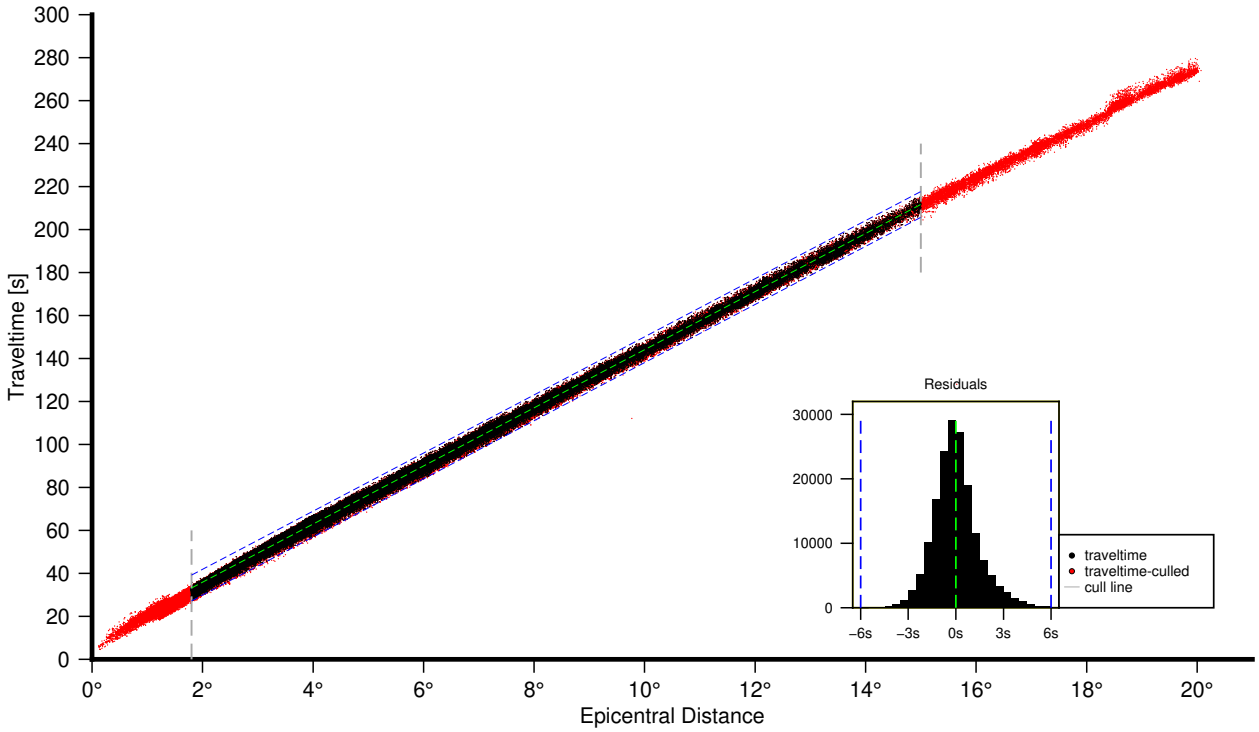

Figure 3.2: Pn traveltimes vs epicentral distance. Cull lines at 1.8° & 15° (grey-hashed) and ±6 seconds (blue-hashed) from the 8.21 km/s average (green-hashed). Inset displays traveltime residuals about the (blue-hashed) average with distribution roughly Gaussian in form.

After we apply the discussed-above culling procedures, our final data coverage consists of 9,393 events, 694 stations, and 169,936 observed traveltimes. Events are primarily shallow and lower in magnitude, originating along the mid-ocean ridges and Scandinavian continental margin (Figure 3.3). Events found within the continental interior are instead more generally from active

source (induced) or mining (Figure 3.4). The event specifics are less important a consideration than achieving significant raypath coverage. We achieve excellent coverage with 850+ crossing rays every 1 x 1° (Figures 3.5 and 3.6). Moreover, we also consider back azimuth distribution because the upper mantle exhibits significant anisotropy and FMTOMO's codebase only considers isotropic wave speed variations. Anisotropy in the upper mantle comes primarily from the preferential alignment of the olivine crystal fast axis. Back azimuths are the directions from the station back-to the source and are published by the ISC. In Figure 3.7, we plot back azimuth distribution for various subregions throughout our model area and scale them by the number of recordings. We consider a relatively uniform distribution of back azimuths of at least a 180° swath, sufficient for assuming good recovery of isotropic structures. Across Scandinavia, we find back azimuth distribution satisfying this assumption.

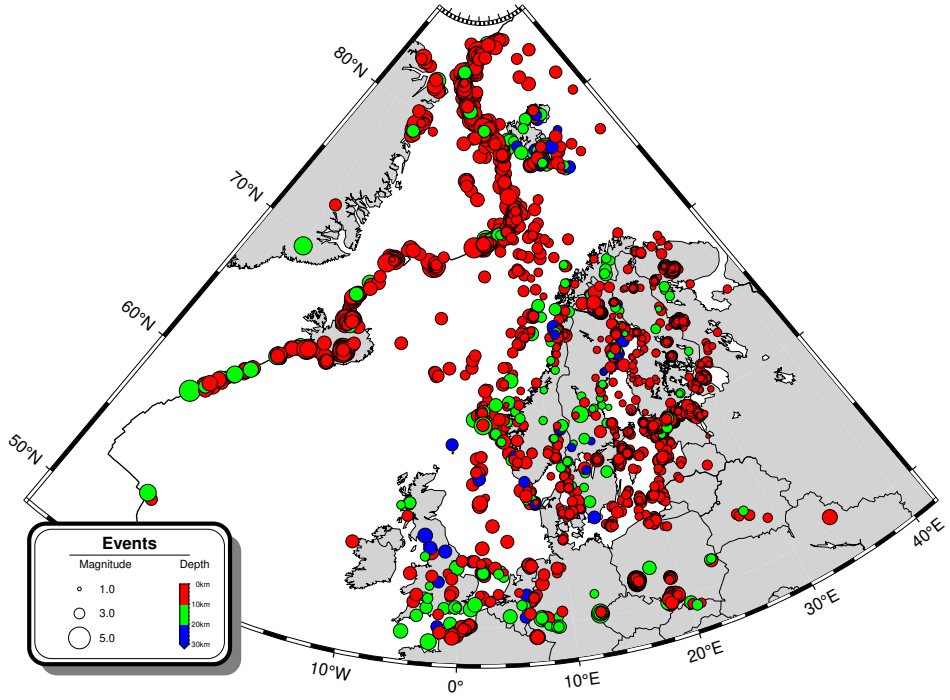

Figure 3.3: Event magnitude and hypocenter depth distribution; (Post culling procedure). Events are scaled by magnitude, with legend entries depicting sample ranges.

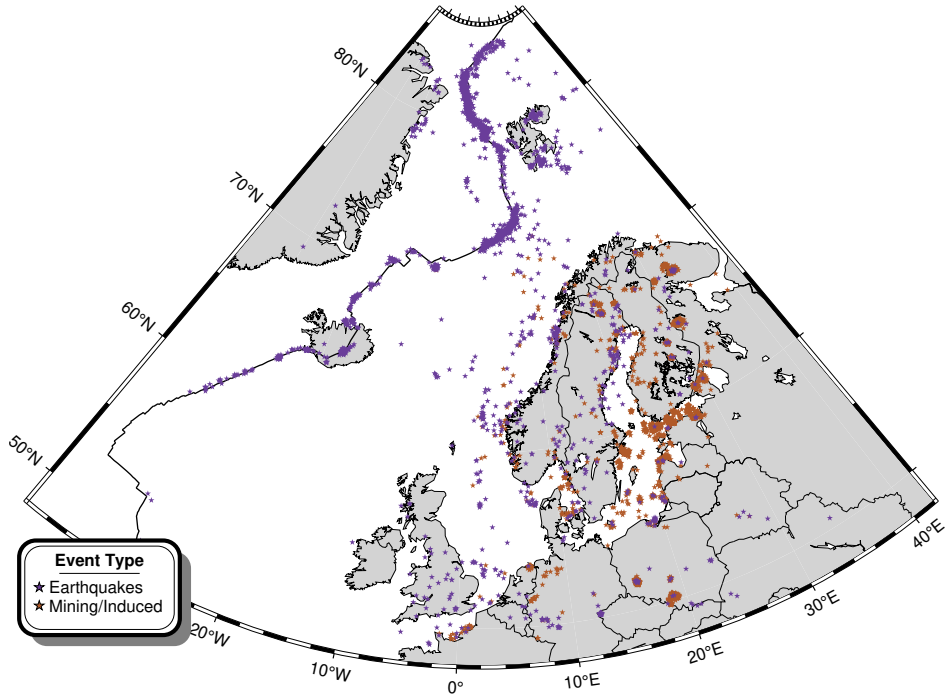

Figure 3.4: Event-type distribution; (Post culling procedure).

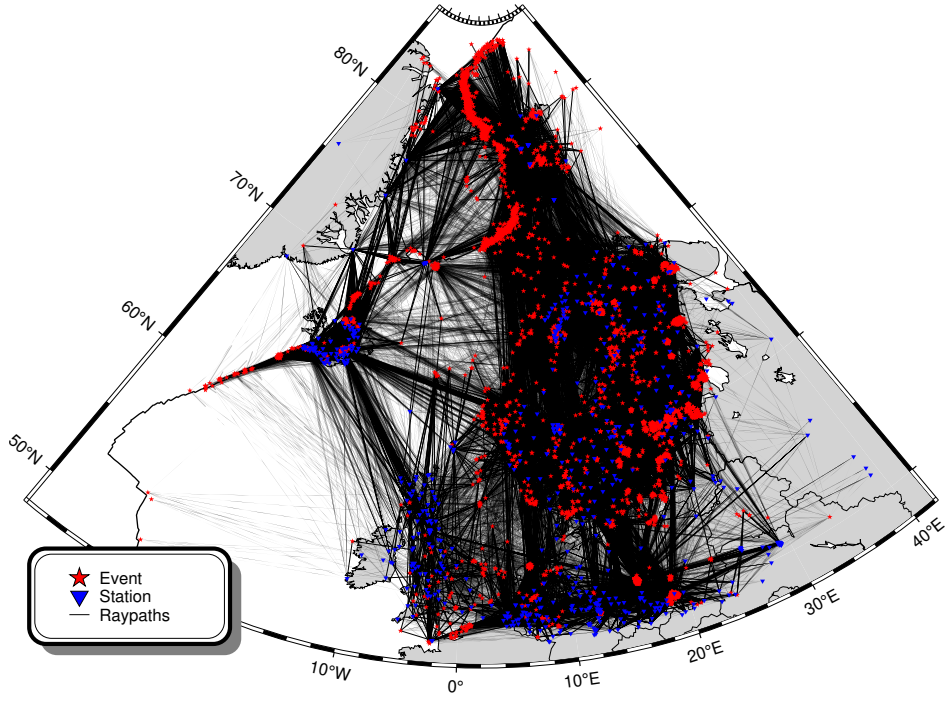

Figure 3.5: Raypath Distribution; (Post culling procedure). Raypaths are drawn as great circle arcs between event to station; Total: 9,393 events, 694 stations, 169,936 rays.

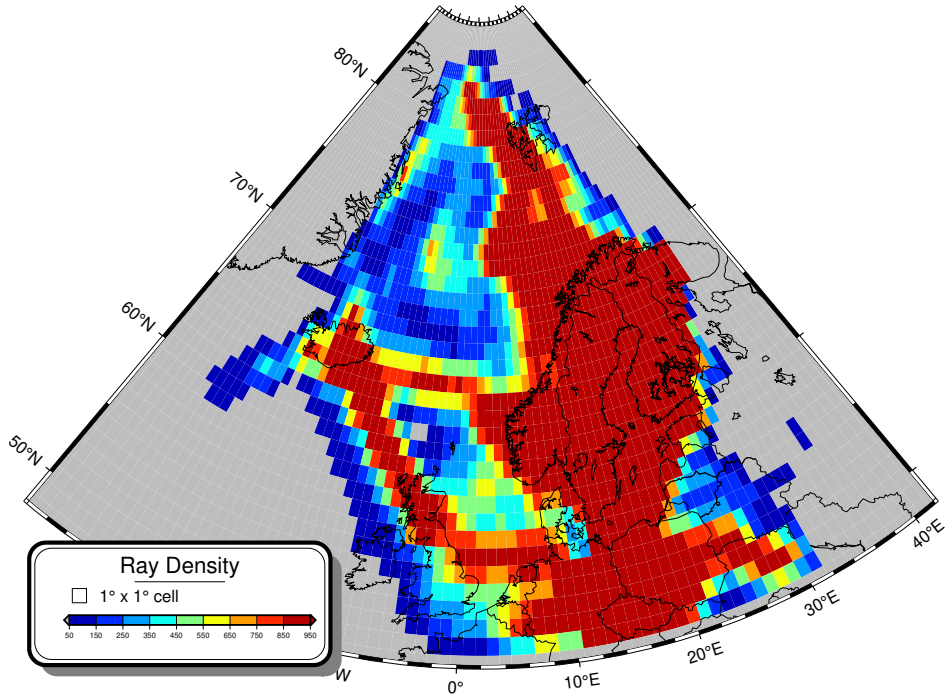

Figure 3.6: Raypath density; (Post culling procedure). Raypaths are drawn as n-great circle arcs between event to station and counted as n++ through each 1 x 1° cell. The total number of crossing rays is n-1.

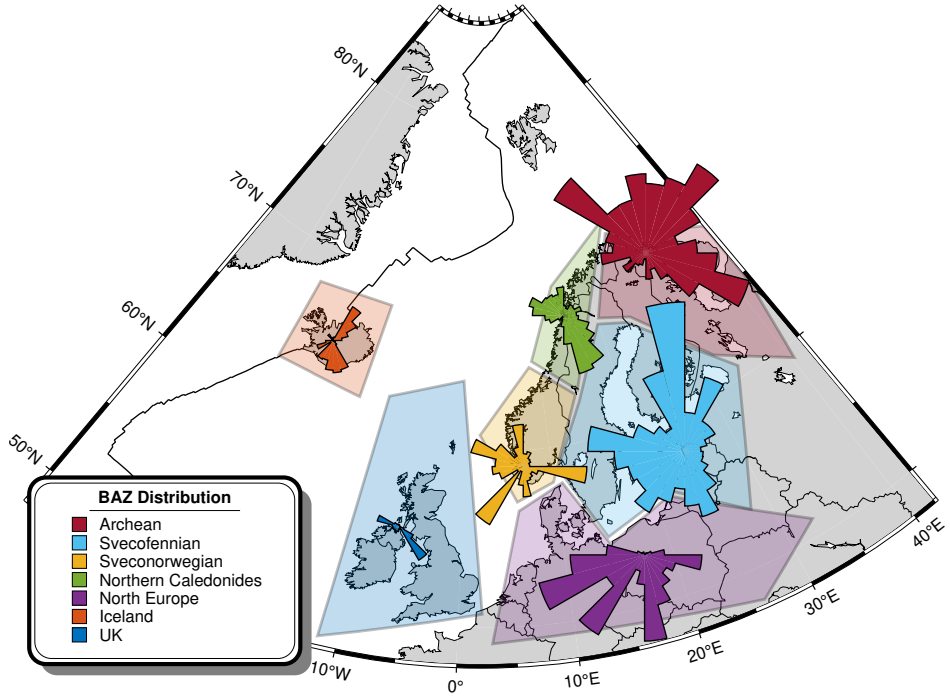

Figure 3.7: Back azimuth distribution "BAZ". (Post culling procedure). Defined for various subregions, mainly after tectonic domains in Figure 2.1. Individual rose diagrams are scaled relative to the total recording-count across all subregions.

3.3 Reference Models

In addition to the ISC event-station geometries, we need to input a reference Moho and velocity model to perform the forward modeling in FMTOMO. The accuracy of FMTOMO's inversion scheme is also greatly benefited by reference models well representative of the regional tectonic characteristics (Sun & Kennett, 2016a).

For the reference Moho model, a first-order approach would be for us to define the Moho at depths equal to P-wave velocities of 7.6 km/s. The Pn ray, as a critically refracted head wave, results from the large velocity contrast at the Moho which is typically 7.6 km/s. However, this approach often fails in a 3D Earth, requiring petrological arguments in support of geophysical evidence to map to its true depths (O'Reilly & Griffin, 2013). We instead consider published open-access models spanning the whole of the model space, and used in similar regional tomographic studies. We choose a high resolution (0.1 x 0.1°) European and North Atlantic Moho model by Grad et al. (2009) made from weighted seismic and gravity studies (reprinted in Figure 3.8). More specifically Grad et al. (2009) combine surface waves (longer periods capable of sampling data-poor oceanic areas), active source surveys (intermediate frequencies at higher resolution), receiver functions (direct imaging of the Moho beneath stations), and Bouguer gravity anomalies (sensitive to density inhomogeneities). Though possible in FMTOMO, we do not consider joint inversion of the Moho interface and instead maintain the model as defined by Grad et al. (2009).

For the reference 3D velocity model, we need to stitch together several regional studies to produce one cohesive model (Figure 3.9). The stitching arises from the majority of ISC event data along mid-ocean ridges and towards the continental interior far from our desired model extents. In choosing reference models we consider similar characteristics as above with the Moho reference. About our desired model extent of Scandinavia proper, we choose a joint inversion of ambient noise and teleseismic surface waves model by Mauerberger et al. (2022) who present a targeted focus of the Scandinavian upper mantle. This model is complemented by the work of Celli et al. (2021), who constrain the data-poor North Atlantic region from longer wavelength surface and S-waves. For any remaining continental Europe, we choose the adjoint tomography model by Zhu et al.

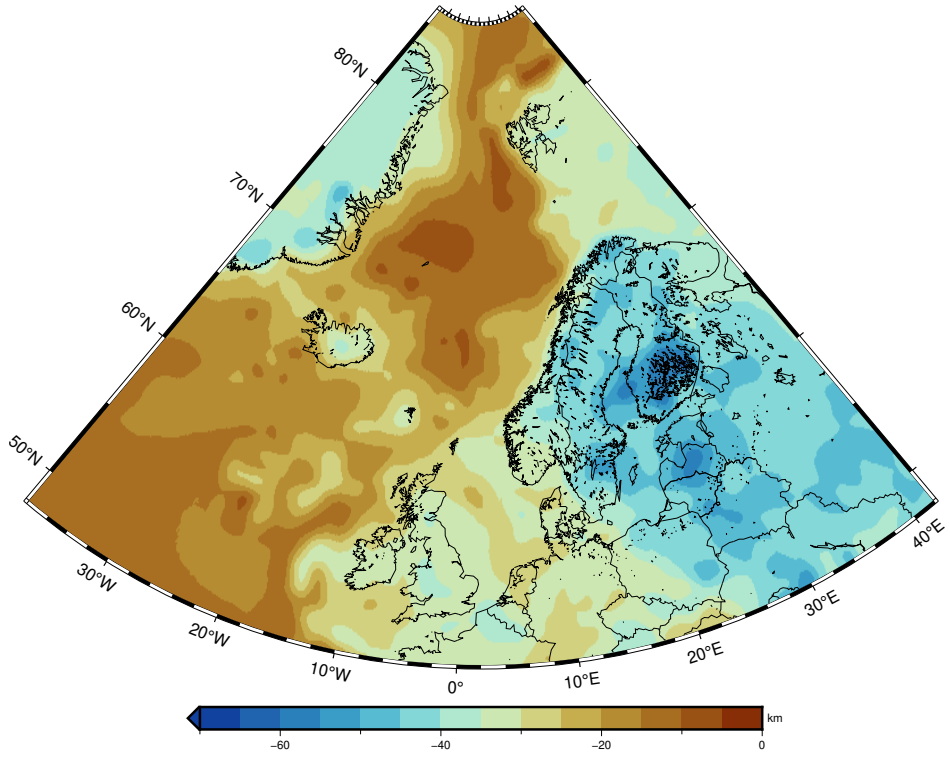

Figure 3.8: Moho depth map. Reproduced from Grad et al. (2009) at published resolution 0.1 x 0.1°. Generally, the Moho trends shallower towards the mid-ocean ridge and deeper towards the cratonic interior. Notably, there is a lack of a pronounced root beneath the Scandes.

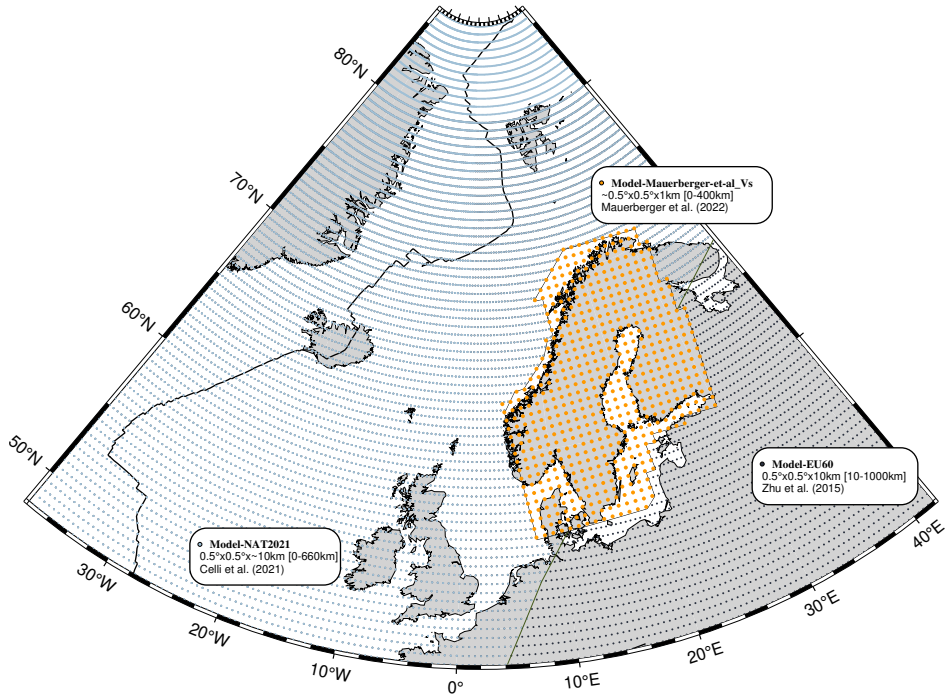

Figure 3.9: Reference 3D velocity model extents and published resolutions. Model values are linearly interpolated "re-gridded" to spherical coordinates at resolution 0.5° x 0.5° x 10 km.

(2015). For continuity, each model is re-gridded for input into FMTOMO as spherical coordinates of same resolution, 0.5° x 0.5° x 10 km. We also take an additional step taken to smooth along model boundaries, though our visual examination across depths revealed no large discontinuities between them.

Because each model's methodology produces shear-wave speeds, we convert the combined reference V_S structure to V_P. Within the crust we use the empirical relations of Brocher (2005). For mantle velocities, we instead relate compositionally derived pressure-temperature effects on seismic velocities through the elastic parameters compiled in Schutt and Lesher (2006) and expanded upon in Schutt and Lesher (2010). First we generate mineral assemblages as functions of pressure and temperature in Perple_X, a Gibbs free energy minimization program (Connolly, 1990). This is accomplished by us inputting to Perple_X sub-continental lithospheric mantle derived xenoliths of western Norway from Beyer et al. (2006) as a normalized whole rock composition. Perple_X is then run with the thermodynamic relations of Jennings and Holland (2015) which best constrain upper mantle mineral and melt compositions, and an anelastic correction accounting for average lithospheric mantle grainsize. Anelasticity is an important consideration for temperatures greater than ~800°C (Jackson & Faul, 2010). Finally, through the compiled elastic parameters of Schutt and Lesher (2006, 2010) we can relate our compositionally derived temperatures to V_S to V_P as a depth (pressure) dependent function. This is also how we will generate our thermal results from our inverted-for V_P structures.

3.4 The Forward Traveltime Solver: FMM

Inputting to FMTOMO the processed ISC data and reference models (see Figure 3.1), we solve for traveltimes using a multistage fast marching method "FMM", a spherical gird-based eikonal solver (de Kool et al., 2006; Rawlinson, Reading, & Kennett, 2006). Fast marching methods were introduced by Sethian (1996), with implementation of FMM in 2D-layered media by Rawlinson and Sambridge (2004a, 2004b), and adapted for spherical coordinates by de Kool et al. (2006). FMTOMO introduces multistage FMM, which "implicitly tracks the evolution of first-arrival wave-

fronts by combining a causal narrow-band evolution scheme with an upwind entropy-satisfying finite difference solution of the eikonal equation" (Rawlinson, de Kool, & Sambridge, 2006). We include this statement from the FMTOMO developers to provide an outline for discussing FMM as we break down what each part means.

The eikonal equation simply relates the gradient of the traveltimes to its slowness (the inverse of velocity). It can be thought of as an approximation of the scalar wave equation, as mapping the propagating wavefront or traveltime surface (SEG, 2014). FMTOMO is defined for spherical coordinates, but we consider the eikonal equation in 2-dimensions for simplicity. From Vidale (1988), the 2D eikonal equation is of the form

$$(\delta \mathbf{t}/\delta \mathbf{x})^2 + (\delta \mathbf{t}/\delta \mathbf{z})^2 = \mathbf{s}(\mathbf{x}, \mathbf{z})^2 \tag{3.1}$$

with spatial variables-$\mathbf{x}$ and -$\mathbf{z}$, time-$\mathbf{t}$, and slowness-$\mathbf{s}$. The raypath (how we typically think about seismic energy propagation) is simply found by integrating along the steepest gradient path (e.g., Figure 3.10).

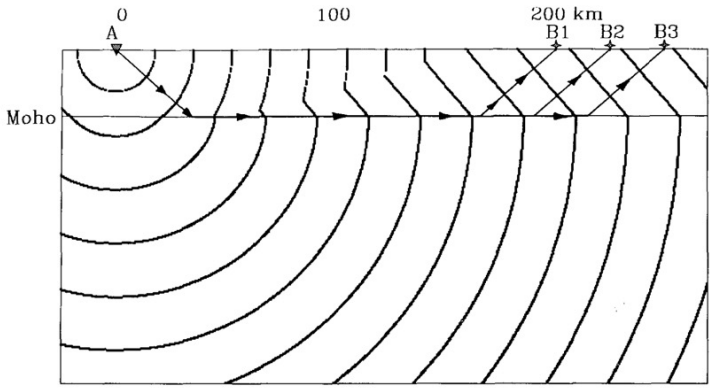

Figure 3.10: Pn ray defined by wavefronts. The source is labeled "A" with recording stations labeled "B". The minimum traveltime path defines the ray. Reprinted from Vidale (1988, Figure 10).

Grid-based eikonal solvers are advantageous for several reasons, the first being traditional ray tracers fail in complex (highly-heterogeneous) media (Vidale, 1988). Also, the underlying assumption for all ray tracing methodologies is satisfying a minimum traveltime governed by the

principles of Snell's laws, which are unable to predict head waves. Pn, an upper mantle head wave, is more readily explained by an application of Huygen's Principle (see arguments below). Finally, working in the higher dimension of tracing the propagating wavefront and not the ray itself introduces stability (Sethian, 1996). We can visualize a moving wavefront as a boundary line of connected buoys in two dimensions and as an outwardly propagating surface in three. In complex media, the buoys may cross over each other in satisfying the minimum traveltime path and create corners or discontinuities, whereas a surface will remain continuous and well-behaved (Sethian, 2006).

FMM is also fast, as the name would imply. As a numerical algorithm, it was introduced by Sethian (1996) for fast computation of the eikonal equation (as presented for the 2D case above). FMM can be conceptualized (in a lower dimension) similarly to other shortest-path algorithms where at each stage the next optimal step is taken (e.g., Dijkstra's algorithm, "greedy" algorithms). We would perhaps most widely recognize this as a feature of Google Maps. FMM works by initializing grid points in a "narrow band" about the propagating wavefront (see Figure 3.11). The traveltime prediction solution is then built out from the source with the shape of the narrow band representing the first-arriving wavefront.

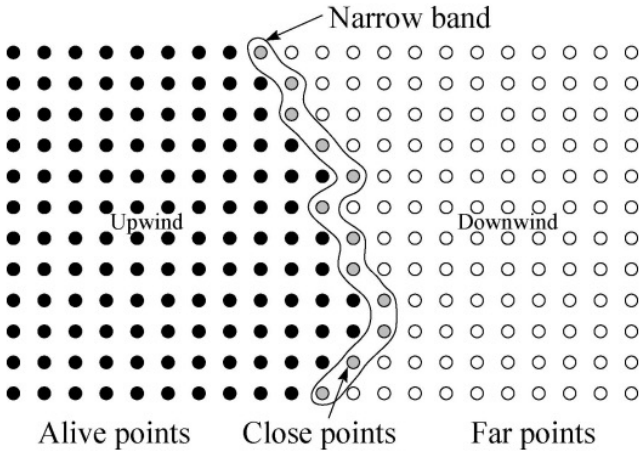

Figure 3.11: The narrowband method. Reprinted from Rawlinson and Sambridge (2004a, Figure 1).

Because this is a discretized (gridded) solution, FMM in FMTOMO uses a finite difference approximation to transform the continuous eikonal equation into a system of numerically solvable equations. A heapsort algorithm is then used to determine a minimum in the narrow band (i.e., the next optimal step) from which marches the narrow band froward like a propagating wavefront (Rawlinson, de Kool, & Sambridge, 2006; Sethian, 1996). We can recognize this as an application of Huygen's principle, where each point in a wavefront serves as a source for new waves, constructively and destructively interfering (Figure 3.12).

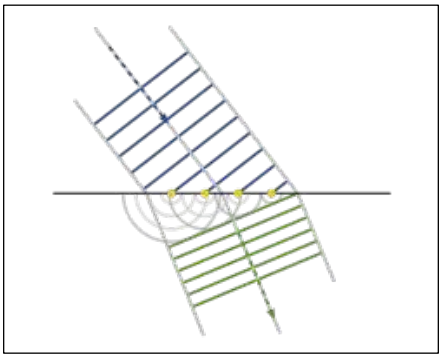

Figure 3.12: Huygens's Principle. Reprinted from Nordmann (2007).

As the narrow band passes, grid points are tagged "alive" and contributing to the narrow band minimum traveltime solution (see Figure 3.11). The narrow band excludes contributions from far field points and defines causality (data order consistency with the directionality of information flow). The narrow band technique in FMTOMO also satisfies entropy as it has a singular outward direction flow. In numerical methods, entropy is alternatively termed upwind where solutions computation is reliant on upstream (prior) solutions. The "multistage" aspect simply refers to the re-initialization of FMM in an adjacent layer once the full wavefront has been mapped to the boundary surface (Rawlinson, de Kool, & Sambridge, 2006).

Immediately about the source, FMM introduces the majority of predicted traveltime error because of the high degree of curvature defining the propagating wave surface (Rawlinson & Sambridge, 2004a). To mitigate this error, in FMTOMO a refined grid is placed about the source which then maps back to the coarser grid as the narrow band approaches. The finer grid is simply a

higher resolution sampling of the defined velocity model. FMTOMO samples the velocity grid with Cubic B-Splines because they exhibit local control and are sufficiently smooth, an important characteristic when solving in the higher dimension (Rawlinson & Sambridge, 2004b). The rationale for introducing a refined grid as opposed to simply defining the whole grid as higher resolution is because computation effort of FMM scales with the number of grid points-$\mathbf{n}$ by $\mathbf{n}log\mathbf{n}$. Because of this we actually switch our sources and receivers to limit solving FMM in FMTOMO to 694 times as opposed to 9,393 (see Figure 3.5). The path integration is the same regardless of source-receiver/receiver-source orientation.

Finally, once the forward travel solver FMM is complete for all events in FMTOMO, its output is used to iteratively improve the velocity model (see Figure 3.1). The inverted-for velocity model is the one which minimizes the difference between the predicted and observed traveltime data.

3.5 The Velocity Inversion Scheme

FMTOMO iteratively adjusts (improves) the velocity model towards satisfying the observed traveltime data by minimizing its misfit with the predicted data FMTOMO generates (see Figure 3.1). More specifically, FMTOMO's inversion is a subspace gradient method that works by minimizing an objective function consisting of data residuals and regularization terms (Rawlinson, Reading, & Kennett, 2006). Data residuals are the difference between the predicted and observed-ISC traveltime data, and the regularization terms necessary to limit the non-uniqueness of the model solution. The iterative nature of the inversion accounts for the nonlinear relationship between traveltimes and velocity structure, and we determine the number of iterations to perform in FMTOMO (Rawlinson, Reading, & Kennett, 2006).

The objective function in FMTOMO for velocity model $\mathbf{m}$ is given by:

$$s(\mathbf{m}) = \frac{1}{2}[\Psi(\mathbf{m}) + \varepsilon\Phi(\mathbf{m}) + \eta\Omega(\mathbf{m})] \tag{3.2}$$

The objective function, defined in Rawlinson and Sambridge (2003), consists of a data residual term $\Psi(\mathbf{m})$; and regularization terms $\Phi(\mathbf{m})$ and $\Omega(\mathbf{m})$ pre-multiplied by factors ε and η respec-

tively. The $\Psi(\mathbf{m})$ term is the heart of the objective function and is a measure of the difference between observed and predicted data. Generally, data d is related to a model $\mathbf{m}$ by an operating function g representing the system's physicality such that $d = g(\mathbf{m})$ (Aster et al., 2018). From Rawlinson and Sambridge (2003), if the observed data represents the true velocity model such that $d_{obs} = g(\mathbf{m}_{true})$, then $\Psi(\mathbf{m})$ is of the form:

$$\Psi(\mathbf{m}) = (g(\mathbf{m}) - d_{obs})^T \, C_d^{-1} \, (g(\mathbf{m}) - d_{obs}) \tag{3.3}$$

The predicted data $d = g(\mathbf{m})$ less d_{obs} is the traveltime misfit, which is weighted by a data weighting matrix with assumed uncorrelated errors C_d (Rawlinson & Sambridge, 2003). Because we prescribe a 0.15 s traveltime error for all ISC picks in C_d (a reasonable assumption), $\Psi(\mathbf{m})$ simplifies to the form $\frac{1}{(0.15\,s)^2} \, ||g(\mathbf{m}) - d_{obs}||^2$, recognizable as a scaled L_2-norm or a Euclidean distance.

The first regularization term imposed in the objective function is the damping term $\Phi(\mathbf{m})$, defined in Rawlinson and Sambridge (2003) and of the form:

$$\Phi(\mathbf{m}) = (\mathbf{m} - \mathbf{m}_0)^T \, C_m^{-1} \, (\mathbf{m} - \mathbf{m}_0) \tag{3.4}$$

Damping works by restricting large wave speed variations produced in the model update, encouraging model solutions $\mathbf{m}$ near the reference model $\mathbf{m}_0$ (Rawlinson & Sambridge, 2003). Therefore, prescribing accurate starting models is paramount to the success of the inversion. Similar to the data weighting matrix C_d, the C_m matrix weights model parameters by a priori imposed uncertainties (Rawlinson & Sambridge, 2003). In an underdetermined system $\Phi(\mathbf{m})$ reduces the non-uniqueness of the model solution. The second imposed regularization $\Omega(\mathbf{m})$ is the smoothing term defined in Rawlinson and Sambridge (2003) and of the form:

$$\Omega(\mathbf{m}) = (\mathbf{m})^T \mathbf{D}^T \mathbf{D} (\mathbf{m}) \tag{3.5}$$

$\Omega(\mathbf{m})$ acts as a minimum structure solution, where matrix $\mathbf{D}$ biases the velocity gradients (Sambridge, 1990). This bias limits local fluctuations, effectively smoothing the resolved structures.

The imposed regularization terms are multiplied in the objective function by the damping and smoothing factors, ε and η. With increasing value, the damping factor ε governs a tradeoff between model and data variance (Rawlinson and Sambridge, 2003; Figure 3.13). This tradeoff can be otherwise thought of as how much we allow the model to update in satisfying our observed traveltime data. The smoothing factor η governs a secondary tradeoff between model roughness and data variance (Rawlinson & Sambridge, 2003). In satisfying the observed traveltime data completely, the model will be noisy and have unrealistic velocity variations, but if the model is too smooth the data is less satisfied. We perform systematic examination of our imposed regularization in FMTOMO by running complete inversions with different values of ε and η to produce tradeoff curves (Figure 3.13). We choose a corner value from the curve we deem satisfactory for data-model misfit, and repeat the process while varying the other factor. We compute three successive tradeoff curves, which as demonstrated by Rawlinson, Reading, and Kennett (2006) and Rawlinson and Sambridge (2003), is quite well suited for determining the optimal zone of imposed regularization.

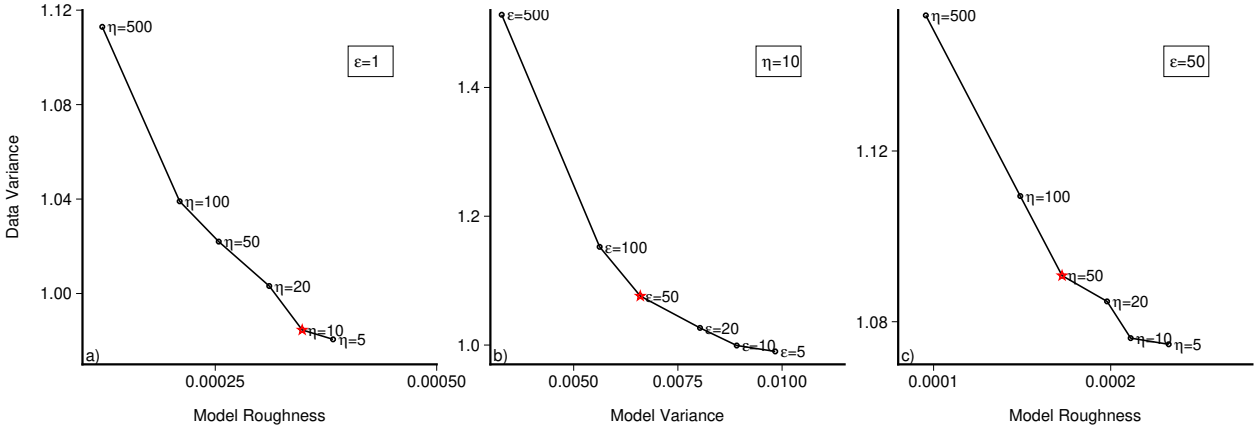

Figure 3.13: Regularization tradeoff curves. (a, c) Modulating the smoothing factor η; (b) modulating the damping factor ε; red stars indicate our chosen corner values used in subsequent tests (left to right) Units: Data variance [s^2]; Model roughness [$(km\ s)^{-1}$]; Model variance [$(km/s)^2$].

The objective function in FMTOMO is minimized by casting its quadratic approximation onto basis vectors spanning a subspace of the model space (Rawlinson & Sambridge, 2003). The moti-

vation for searching within the subspaces is to restrict the dimensionality of the inverted-for matrix to one relatively small for faster calculation. The trick is to determine which subspaces to search through in some intelligible way. In FMTOMO, singular value decomposition "SVD" of model $\mathbf{m}$ produces orthonormal bases ordered by steepest ascent and its subsequent rates of change (Rawlinson, Reading, & Kennett, 2006). We then limit the search direction to 20 subspaces which only considers the greatest contribution to the model update.

A quadratic approximation is simply a higher order extension of the linear approximation which seeks to identify the next point on a curve from its tangent line. For a general function $f(x)$, its quadratic approximation is of the form:

$$f(x) \approx f(x_0) \; + \; f'(x_0)(x - x_0) \; + \; \frac{1}{2} f''(x_0)(x - x_0)^2 \tag{3.6}$$

Equation 3.6 reads that the value at position x is approximately the value at x_0 plus the value contributions from the linear-slope (f') and curvature (f'') defined at x_0. As it relates to the objective function defined in FMTOMO, the difference in positions $(x - x_0)$ of Equation 3.6 can be considered as the model update $\delta\mathbf{m}$. The quadratic approximation of FMTOMO's objective function is defined in Rawlinson and Sambridge (2003) and given by:

$$s(\mathbf{m} + \delta\mathbf{m}) \approx s(\mathbf{m}) \; + \; \gamma(\delta\mathbf{m}) \; + \; \frac{1}{2} \delta\mathbf{m}^T \mathbf{H} \delta\mathbf{m} \tag{3.7}$$

Thus, with each iteration, a model update $\delta\mathbf{m}$ is found from the reference model $\mathbf{m}$ (Figure 3.14). The terms γ and $\mathbf{H}$ are the unit gradient vector and Hessian matrix respectively. The gradient gives the direction of greatest change for the function at a given point, where the Hessian gives direction and rate of change of the gradient itself. Both are conceptually similar to the scalar f' and f'' terms of Equation 3.6, but defined for FMTOMO's multivariate objective function $s(\mathbf{m})$. With each iteration producing a model update $\delta\mathbf{m}$, new predicted traveltimes are generated in FMTOMO's forward traveltime solver more closely matching the observed (Figure 3.1).

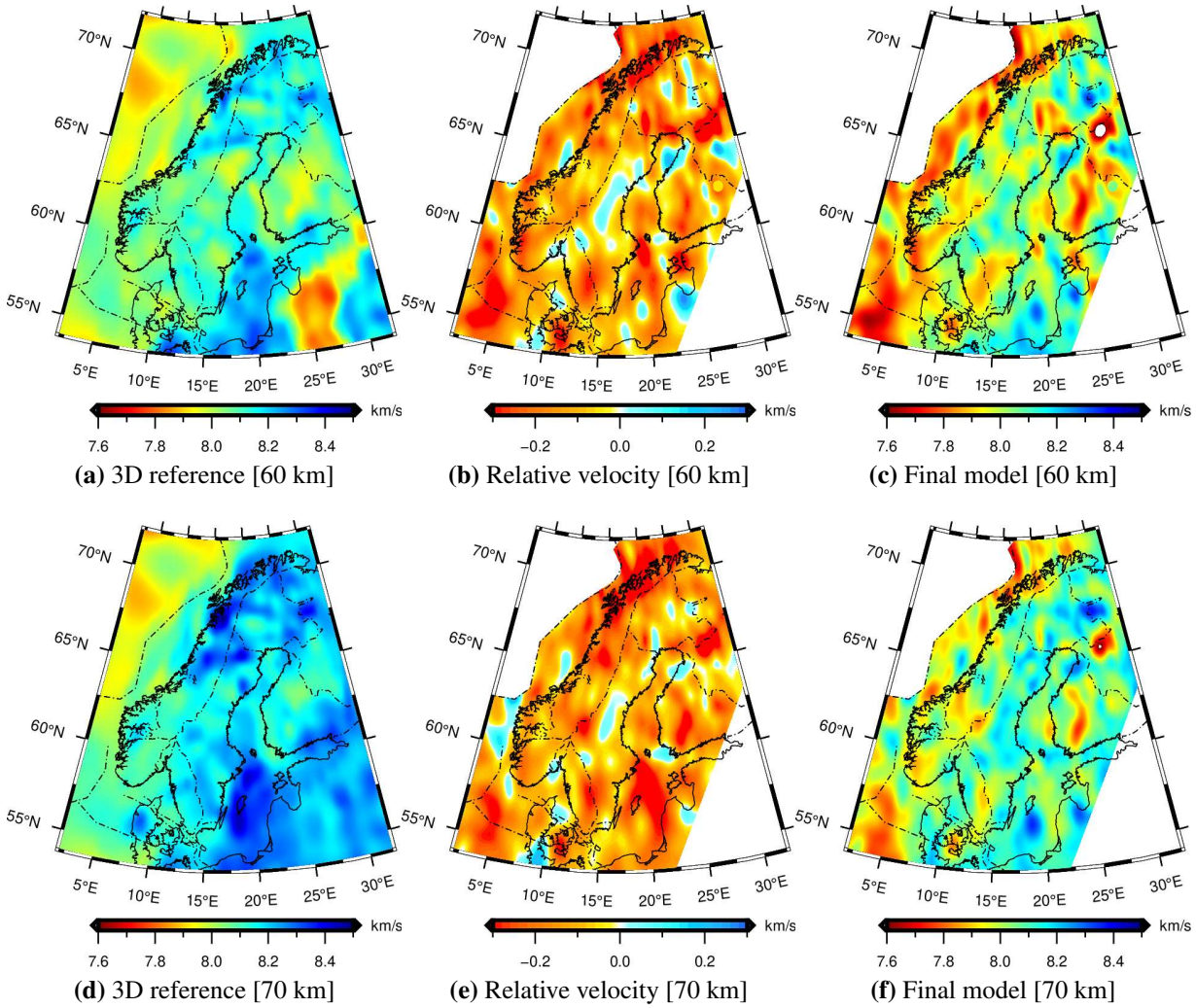

(a) 3D reference [60 km] **(b)** Relative velocity [60 km] **(c)** Final model [60 km]

(d) 3D reference [70 km] **(e)** Relative velocity [70 km] **(f)** Final model [70 km]

Figure 3.14: Velocity model updates from the 3D reference model. Colormaps for the reference (a, d) and final (c, f) are presented for the same 7.6 – 8.5 km/s continuous scale. Lateral extent is clipped to areas of excellent checkerboard recovery (Figure 4.1) for update and final models. Black dot-dash lines are tectonic boundaries and prominent suture zones mapped crustal expressions defined in Figure 2.1.

We perform five iterations of inversion for a spherical grid spaced 0.5° x 0.5° x 10 km, totaling 260,337 nodes. The inversion encompasses the full data region we define in Figure 1.1 with depths extending to 195 km to allow for deeper diving rays at greater epicentral distances (e.g., Sun and Kennett, 2016a). In addition to the uppermost mantle layer, we also invert for the overlying crustal velocities to account for along-path effects.

Chapter 4

4.1 Resolution Tests

Prior to interpreting any inversion results, we perform a series of formal resolution tests to asses the imaging capabilities we prescribe in our FMTOMO model design. Checkerboard and other synthetic resolution tests are quite ubiquitous in inversion problems. They provide a qualitative measure of model capabilities where quantitative measures cannot or do not exist (Rawlinson & Spakman, 2016). These tests are achieved by generating synthetic data through a prescribed series of alternating positive and negative anomalies resembling a checkerboard. The synthetic data is then used as the "observed" data to solve the inversion scheme. The shape and magnitude of the recovered checkers determines the imaging capabilities of the model design and data coverage capabilities.

Following best practices for checkerboard design from Rawlinson and Spakman (2016), we (*a*) maintain the same model design between synthetic data generation and inversion, (*b*) use a sparse checkerboard of discrete spikes to assess smearing, and (*c*) test across checker sizes to assess resolution at multiple scale lengths. However, implementing point-*a* exactly in FMTOMO is unachievable because FMM traces each ray to its minimum travel time with positive (higher) velocity checkers therefore attracting to the ray and modulating its traveltime. We address this by designing three tests of different checker size and layout (points-*b* and *c*) and with qualitative interpretation of their results.

Synthetic traveltime data we produce from the same source-receiver configuration as the ISC data and iteratively invert for velocity structure using the same FMTOMO model parameterization and regularization described in prior sections. We design alternating positive and negative checkers with maximum imposed anomalies of $\pm 2\%$ of the velocities found at ~50 – 80 km (the a priori presumed depth of highest resolution). The checkers overlay the velocity grid for the generation of the synthetic data, but are absent for the inversion. For simplicity we use ak135 from Kennett

(2005), a spherically averaged 1D velocity model, in the generation of synthetic data. Argued below, we find this to be a reasonable substitution.

4.2 Results: Model Resolution

We present our imposed and recovered checkerboards in Figure 4.1. We limit recovery depths shown to those demonstrating excellent recovery, which we determine to be 60 and 70 km. The inversion grid is defined with resolution 0.5° x 0.5° x 10 km and intermediate values defined by cubic B-splines between grid nodes. The series of checkerboards we produce include a 3 x 3° and finer 2 x 2° with sparse testing. As a qualitative assessment, we are capable of resolving the finer 2 x 2° checkers, meaning our velocity inversion results can also be interpreted as resolving structures of 2 x 2° or better.

Overall, the recovered checkerboard patterns demonstrate remarkable resolution across our model region. Velocity perturbations are generally recovered higher than the imposed within the 3 x 3° board, meaning final velocities can be interpreted as slightly under-damped relative to the "true" structure. However, recovered velocities are slightly over-damped in the 2 x 2° indicating a wavelength component to magnitude recovery. Areas of poorer recovery have checkers appearing smeared or conjoined, meaning lack of resolving power at those scales/depths. We can generally attribute areas of poor recovery to a lack of station coverage. This is especially evident towards the northwest corner of the model region (in the Atlantic) where we do not have any station coverage, but do have crossing rays (see Figure 4.1i). We observe the same poor recovery in the southeast model corner (within the Baltic countries) and to a lesser extent in central Norway and Sweden along the Caledonian Deformation Front ("CDF" in Figure 4.1).

The effects of raypath coverage can also be assessed through a sparse checkerboard test. Given sufficient crossing rays, Pn is excellent at discriminating uppermost mantle heterogeneities because it travels nearly horizontal as an upper mantle head wave. Over prescribed raypath geometries can also affect recovery by producing along-path smearing. Our results for the sparse 2 x 2° test reveal lateral smearing especially prevalent within the northernmost land areas (see Figure 4.1f). These

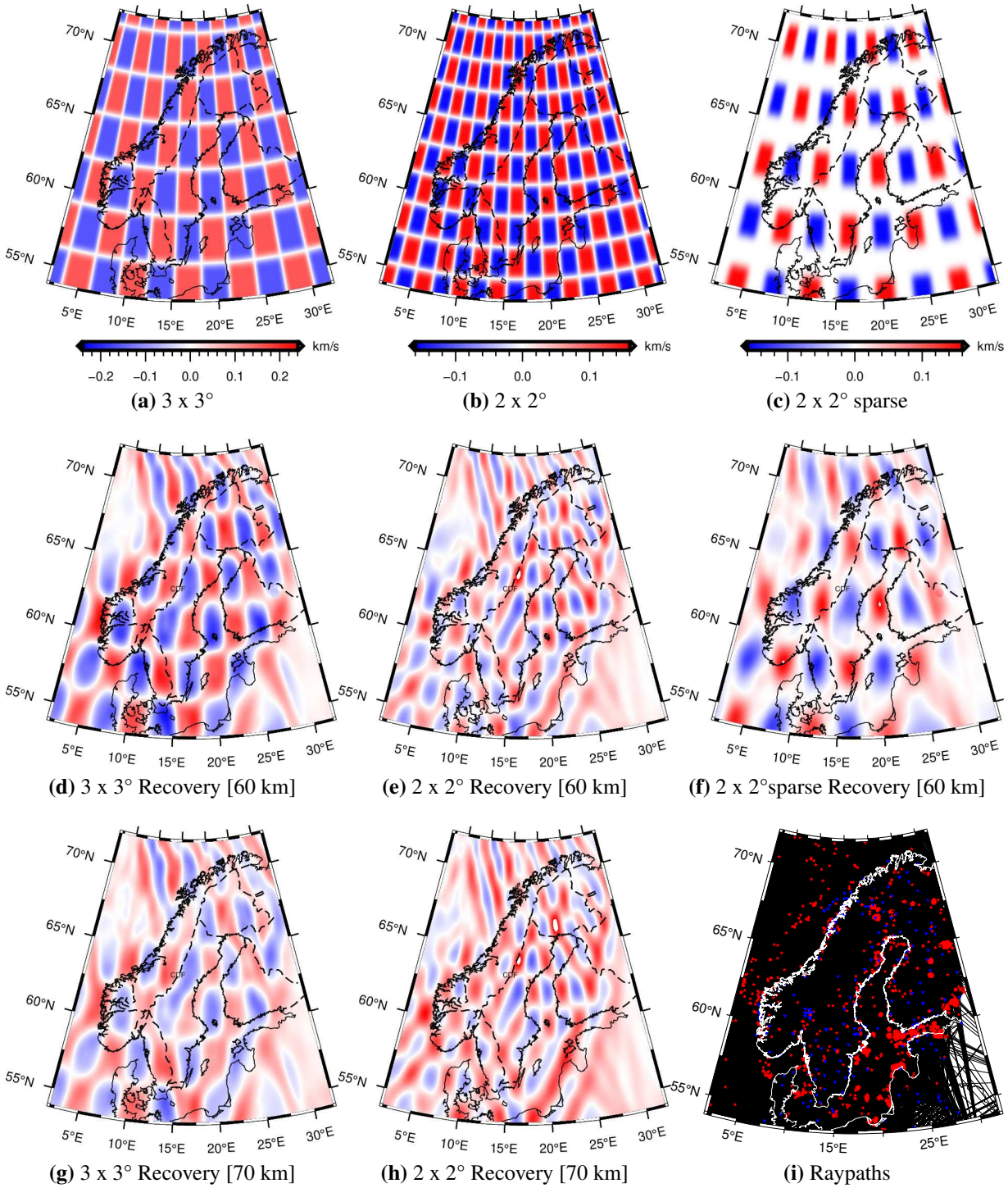

(a) 3 x 3° **(b)** 2 x 2° **(c)** 2 x 2° sparse

(d) 3 x 3° Recovery [60 km] **(e)** 2 x 2° Recovery [60 km] **(f)** 2 x 2°sparse Recovery [60 km]

(g) 3 x 3° Recovery [70 km] **(h)** 2 x 2° Recovery [70 km] **(i)** Raypaths

Figure 4.1: Checkerboard tests; Imposed ±2% velocity perturbations for (a) 3 x 3°, (b) 2 x 2°, and (c) 2 x 2° sparse checkers. Recovered checkers (d-f) at 60 km and (g,h) 70 km after five iterations using final model regularization. Raypaths are shown in (i) as great circle arcs between events (red stars) and stations (blue triangles). Colorbars are consistent vertically but notice the scale change between (a) and (b,c). Black dot-dash lines are tectonic boundaries and prominent suture zones mapped crustal expressions defined in Figure 2.1. *CDF = Caledonian Deformation Front.*

checkers generally trend northwest towards a section of mid ocean ridge with an abundance of observed events. Smearing is also slightly prevalent within the latitudes ~60 – 65° trending south towards several assumed mining operations in Northern Europe.

We also address any a priori assumptions imposed by the 3D reference velocity model by running our tomographic inversion with ak135 as its reference (Kennett, 2005). The location, form, and magnitudes of final velocity structures are quite similar to that of the 3D-referenced final model with the 3D-referenced mapping higher-order/greater complexity (Figure 4.2). Moreover, the data variance reduction across five iterations for both the 3D and 1D referenced final models are nearly the same (Figure 4.3). This validates our choice of 3D reference velocity model and also showcases our model parametrization and data coverage capable of resolving similar structures from a simple reference. We determine five iterations sufficient to achieve satisfactory convergence between modeled and observed traveltime data. Across the five iterations with our imposed regularization, we achieve an overall 63.3% reduction in data variance in FMTOMO (see Figure 4.3a).

4.3 Results: Velocity Inversion and Temperatures

We present our final tomographic images of absolute P-wave velocity and temperature structures for 60 and 70 km depths in Figure 4.4. Results are colormapped to equal ranges and presented for longitudes of 2 – 32° and latitudes 54 – 72°.

At uppermost mantle depths of 60 and 70 km, we observe a high degree of heterogeneity across the model region. Broadly however, we observe velocities increasing with depth and east towards the interior of the craton. Our derived temperatures for the upper mantle map according to our inverted-for velocity structures and so exhibit the same trends of general "cooling" with higher velocities. From the global 1D velocity model ak135, the average velocity for our model depths is 8.045 km/s (Kennett, 2005). From our methodology, 8.045 km/s is quantified as an average uppermost mantle temperature of ~880°C. Because of the level of heterogeneity we observe, we instead refer to velocities about the global average as anomalously low or high with corresponding high/low respective quantified temperatures.

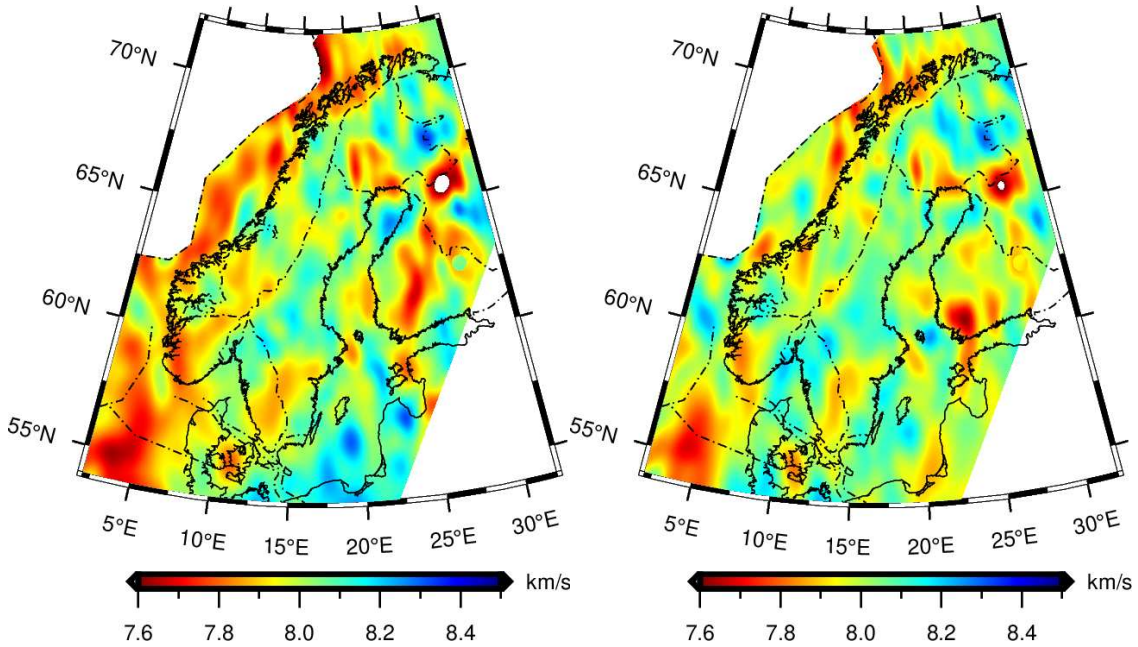

(a) 3D referenced Final Model [60 km]

(b) 1D referenced Final Model [60 km]

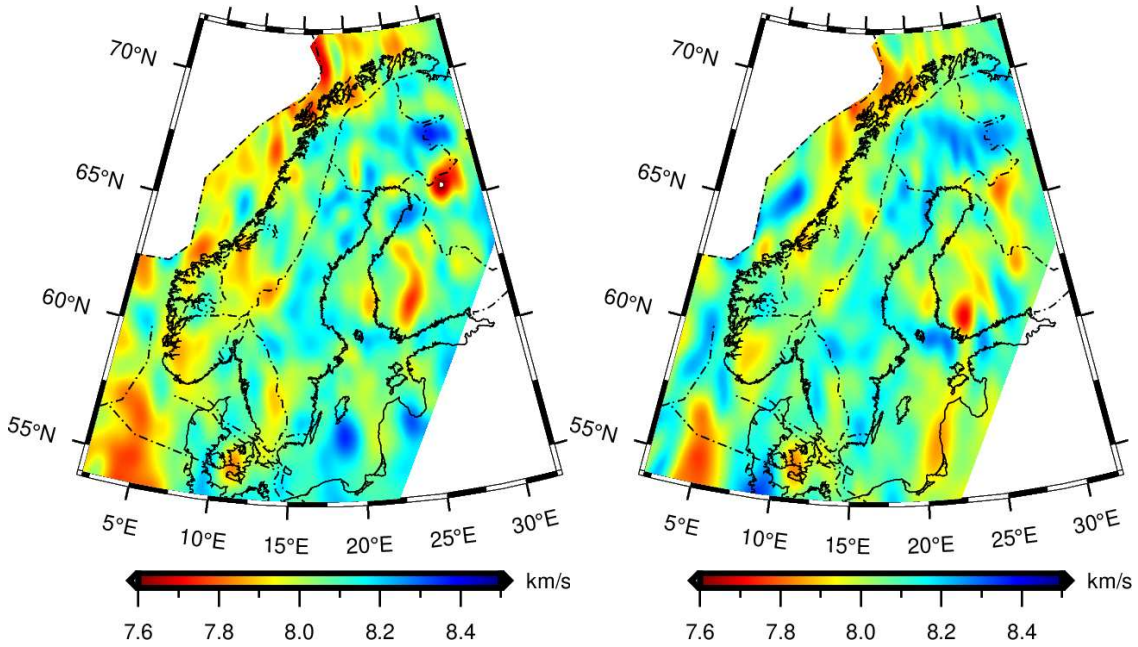

(c) 3D referenced Final Model [70 km]

(d) 1D referenced Final Model [70 km]

Figure 4.2: Final inversion results referencing 3D (a,c) and 1D (b,d) velocity models. Results are after five iterations using final model regularization. Colormaps are presented for the same 7.6 – 8.5 km/s scale. Lateral extent is clipped to areas of excellent checkerboard recovery (Figure 4.1). Black dot-dash lines are tectonic boundaries and prominent suture zones mapped crustal expressions defined in Figure 2.1.

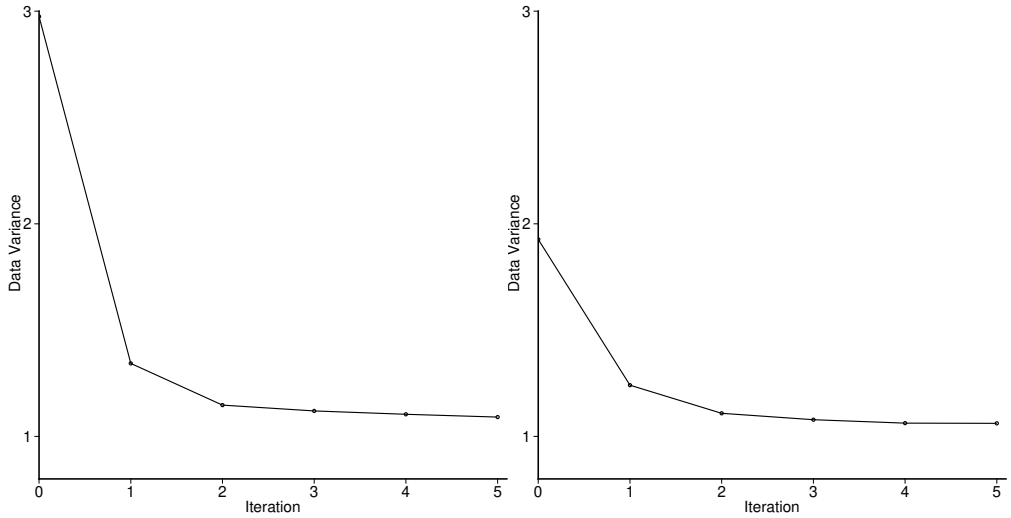

(a) 3D referenced model **(b)** 1D referenced model

Figure 4.3: Data variance reduction across five iterations. Final data variance between predicted and observed traveltimes for (a) is 1.09 s^2 and (b) 1.06 s^2.

In the North Sea ("NS", Figure 4.4) we find an elongated anomalously slow wave speed body, becoming convex with increasing depth. The body's temperatures are also quite high (>1300°C) but do not indicate the presence of partial melt. We also observe lower velocities beneath the southern Scandes in southern Norway (see southern dome outline, Figure 4.4). At 60 km, these extend towards the North Sea and along the continental margin ("CM", Figure 4.4).

Continuing northwards, similar magnitude anomalies (velocities less than 7.8 km/s) follow the continental margin at 60 km but do not appear to connect with those observed beneath the Lofoten Peninsula at 60 and 70 km. Moreover, the Caledonian Deformation Front ("CDF", Figure 4.4) clearly marks their lateral extent and transition to faster velocities east beneath the Svecofennian province. Noticeably too, within the northern dome section of the Scandes (see northern dome outline, Figure 4.4), recovered magnitudes are subdued relative to their southern counterpart and the Lofoten region.

Within Finland, we find an elongated low velocity body "ribbon" trending north-northeast and tapering with depth in both size and magnitude (see "LVR", Figure 4.4). This ribbon traverses Svecofennian to Archean lithosphere, and its northernmost extent at 60 km has velocities as low as 7.4 km/s. Otherwise, the Svecofennian province is comparatively homogeneous, especially at 70

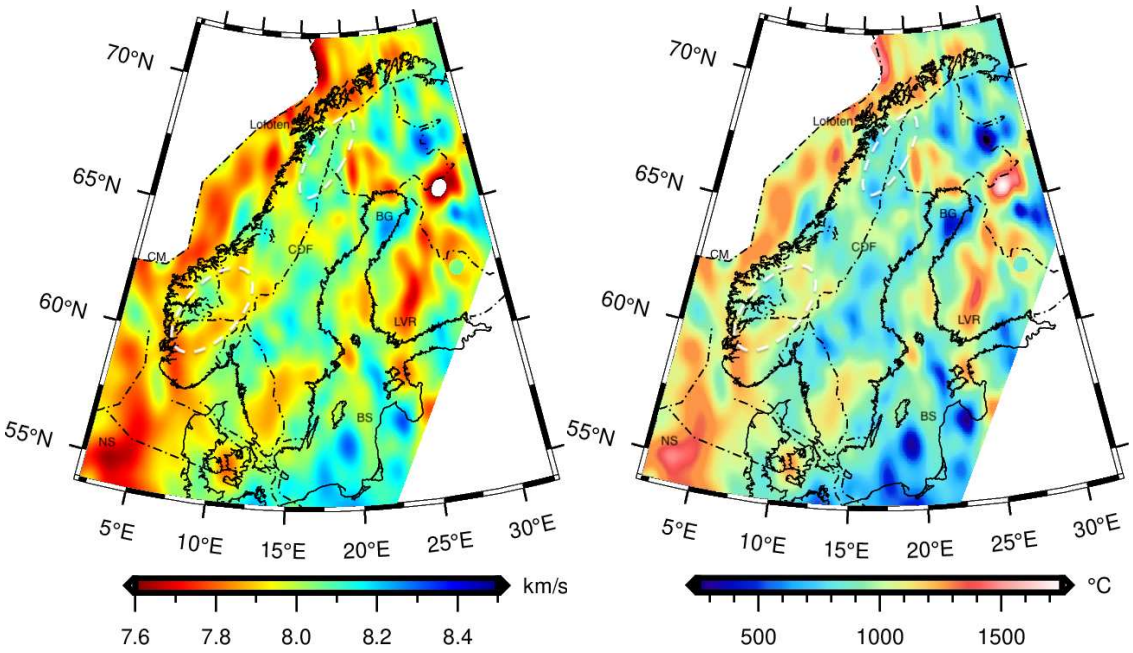

(a) V_P [60 km] **(b)** Temperature [60 km]

(c) V_P [70 km] **(d)** Temperature [70 km]

Figure 4.4: V_P and temperature results; after five iterations using final model regularization. Colormaps for V_P and temperature are presented for the same respective scales. Lateral extent is clipped to areas of excellent checkerboard recovery (Figure 4.1). Black dot-dash lines are tectonic boundaries and prominent suture zones mapped crustal expressions defined in Figure 2.1. The Scandes southern and northern domes are outlined by white hash marks. *BG = Bothnian Gulf, BS = Baltic Sea, CDF = Caledonian Deformation Front, CM = Continental Margin, LVR = low velocity ribbon, NS = North Sea.*

km with higher velocities at or near 8.15 km/s. To the northwest of the ribbon, at 60 km we observe a higher velocity body ~8.3 km/s roughly coincident with the Archean to Paleoproterozoic cover transition (marked by the black dot-dash line in Figure 4.4) in the Belomorian region. Interestingly, this body actually increases spatially and in magnitude from 60 to 70 km. Also within the covered Archean domain, just north of the Bothnian gulf ("BG", Figure 4.4), are lower velocity features imaged at 60 km not present at 70 km.

Towards the southeast of the model region, in the Baltic Sea ("BS", Figure 4.4) at 60 km, there are four spherically shaped higher velocities bodies. These appear to be higher order features overlaying a general trending southeast increase in velocity. Finally, lower velocities in the Sveconorwegian domain in southern Sweden appear to extend into the Svecofennian province at 60 km, but not at 70 km.

Chapter 5

5.1 Discussion

We first address the level of heterogeneity in our final model results that we observe within and across tectonic regions (see Figure 4.4). Generally, upper mantle P-velocities are a function of the thermal structure, though their relationship to tectonothermal ages remains somewhat controversial (e.g, Artemieva et al., 2006). Regardless, lithospheric velocities at 60 and 70 km depths are not likely to strictly follow the tectonic domain boundaries defined on the surface (i.e., the black dot-dash lines in Figure 4.4). This should be especially true for regions characterized by an over 2 Ga tectonic history of repeated reworking and subsequent stabilization. In similarly designed studies of cratonic regions, Sun and Kennett (2016a, 2016b) also find a distribution of higher order superimposed substructures from Pn. Moreover, because Pn has remarkable resolving power at depths typically smoothed over from other seismic methods, the finding of new finer-scale structures is expected (e.g., our model updates shown in Figure 3.14)

Regardless, we address the resolution capabilities of our FMTOMO model design by performing a series of checkerboard tests (see Figure 4.1). As a qualitative assessment, they showcase excellent recovery and demonstrate our results are interpretable at scales 2 x 2° or finer. Moreover, inverting for structure from a simple 1D reference velocity we find yields similar results. Thus, we assert the position, form, and magnitude of our final model structures are realistic uppermost mantle velocities.

Interpretation of Structures

The anomalous body of low-velocities/high-temperatures in the North Sea are likely related to thermal doming in the Jurassic (e.g., Underhill and Partington, 1993; see "NS", Figure 4.4). Its convex shape near the base of the Moho and location relative to broader scale upper crustal compensation (i.e., graben formation; Ziegler, 1992) all point to this interpretation.

Low velocities beneath the southern Scandes in Norway are a well-known feature across numerous seismic studies (Bannister et al., 1991; Husebye et al., 1986; Latif, 2012; Maupin, 2011; Medhus et al., 2009, 2012; Weidle & Maupin, 2008). Our V_P results further confirm this and spatially correlate well with the prior Pn tomographic images of Bannister et al. (1991) and Latif (2012), though our results present higher resolution features (Figure 5.1). Bannister et al. (1991) attribute this observation to the existence of less dense uppermost mantle material. This idea has also been championed by several gravity studies (see Ebbing et al., 2012 for review). Our converted-temperature results showing higher temperatures in the region readily confirm this and point to dynamic support of the southern Scandes topography.

The depth and lateral extents of our inversion are somewhat spatially/temporally isolated from confirming any single geodynamic mechanism. It is likely however that our observed temperatures are derived from a deeper-seated (still upper mantle) source responsible for transferring thermal energy to the uppermost mantle. We find similar temperature distribution and magnitudes of around 1100 – 1300°C as Goes et al. (2000) in the southern Scandes (Figure 5.2). Though a lower resolution tomographic study, higher temperatures found in Goes et al. (2000) extend from beneath the Moho to depths of at least 100 km. From averaged Rayleigh-wave dispersion curves, Maupin (2011) identifies this anomalous body extending from ~60 – 250 km in a 1D profile of the region. Medhus et al. (2012) finds from P-wave traveltime tomography the lower velocitites extending further southwest with increasing depth, possibly connecting to the localized North Sea anomaly at 500 – 600 km. They suggest from absolute plate motion, movement of Scandinavia over this anomalous warm upper mantle. This interpretation is unlikely though, because the 410 discontinuity has been imaged as flat (e.g., Makushkina et al., 2019).

Weidle and Maupin (2008) suggest from surface wave velocities an ~70 – 150 km depth, 400 km wide conduit connecting low velocities in the southern Scandes to that of the Iceland Plume (Figure 5.3). Latif (2012) further confirm this conduit (see Figure 5.1b), though suggest greater complexity to its proposed structure. In their global shear wave model for the upper mantle and transition zone, Schaeffer and Lebedev (2013) find similar (though more broad) lower velocities

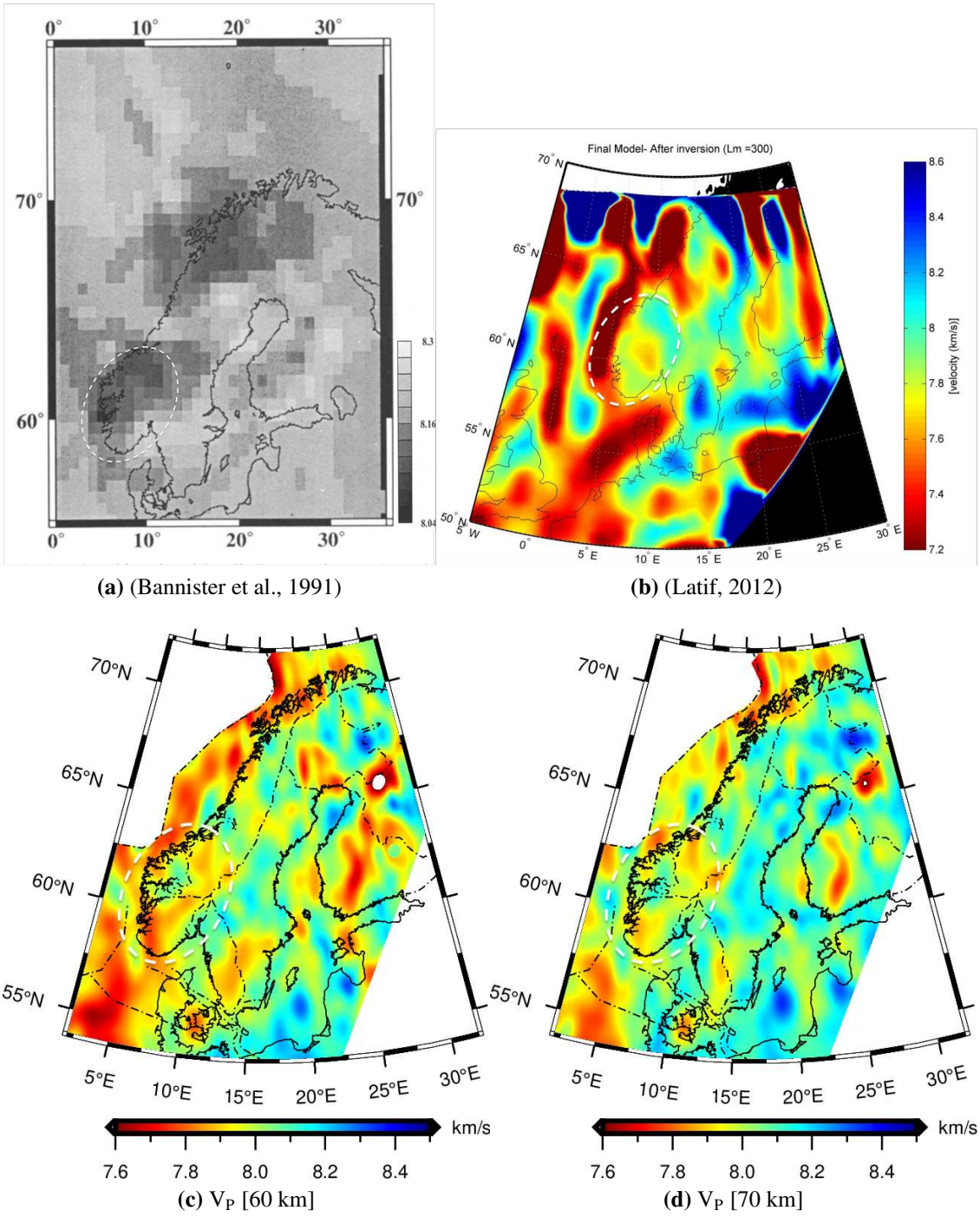

(a) (Bannister et al., 1991) **(b)** (Latif, 2012)

(c) V_P [60 km] **(d)** V_P [70 km]

Figure 5.1: V_P results comparison. (a) Reprinted from Bannister et al. (1991, Figure 7); (b) Reprinted from Latif (2012, Figure 5.1). (c,d) Our V_P results (see Figure 4.4 for full description). The southern Scandes are outlined by white hash-marks.

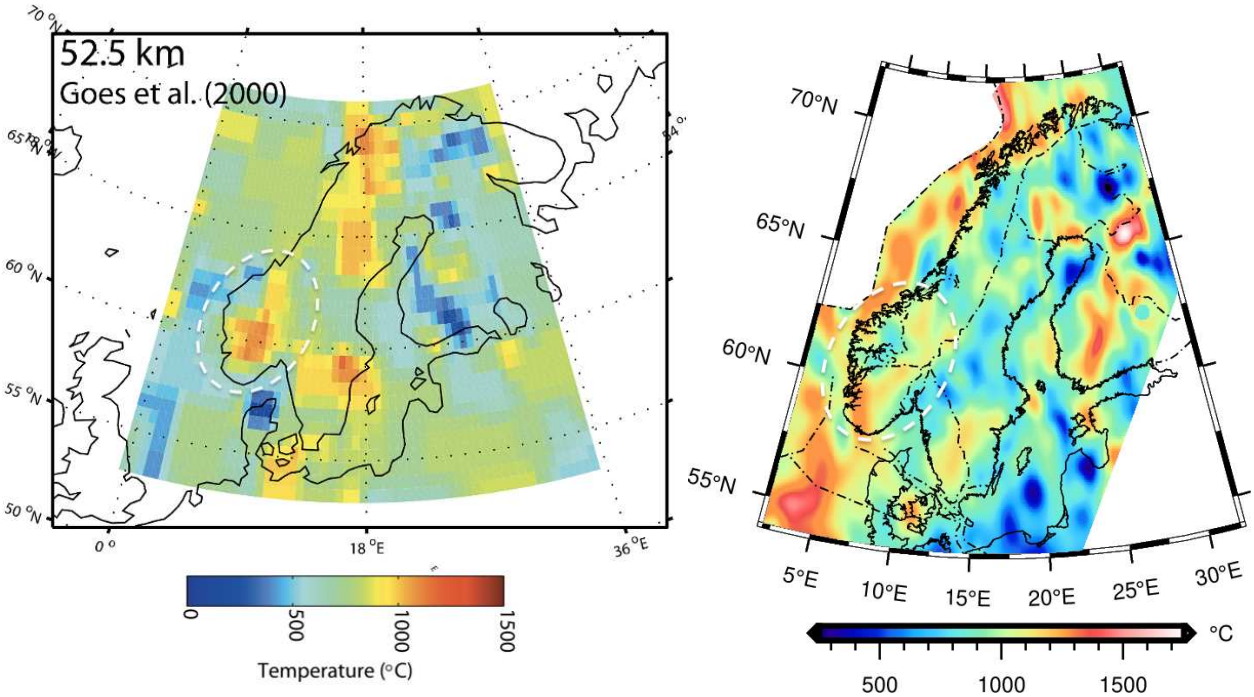

(a) (Goes et al., 2000) [52.5 km] **(b)** Temperature [60 km]

Figure 5.2: Temperature results comparison. (a) Reprinted from Barnhoorn et al. (2011, Figure 1) who show results from Goes et al. (2000); (b) Our temperature results (see Figure 4.4 for full description). The southern Scandes are outlined by white hash-marks.

extending from the Iceland plume (see Figure 5.3b). Also imaged by ambient noise and teleseismic Rayleigh waves, Mauerberger et al. (2022) suggest small-scale edge-drive convection as a mechanism for transferring the thermally buoyant asthenosphere material to the uppermost mantle (see Figure 5.3b).

We are unable to independently verify such a connection at depth to the Iceland Plume because our velocity model best resolves the uppermost mantle ~60 – 70 km. However, our results do not exist in a spatial vacuum and do connect to deeper-seated structures that are mostly un-updated values from what we input as 3D reference velocities. Beneath Scandinavia, these values reference the results from Mauerberger et al. (2022) (see Figures 3.9, 5.3b). At 60 km we do see a connection between lower velocities in the southern Scandes and those trending towards the northwest (see Figure 5.1c). These are more likely a result of Cenozoic opening of the North Atlantic because also at 60 km are similar magnitude low-velocity/high-temperatures found along the whole Continental shelf. However, we cannot rule out the possibility of a deeper seated connection to thermal material

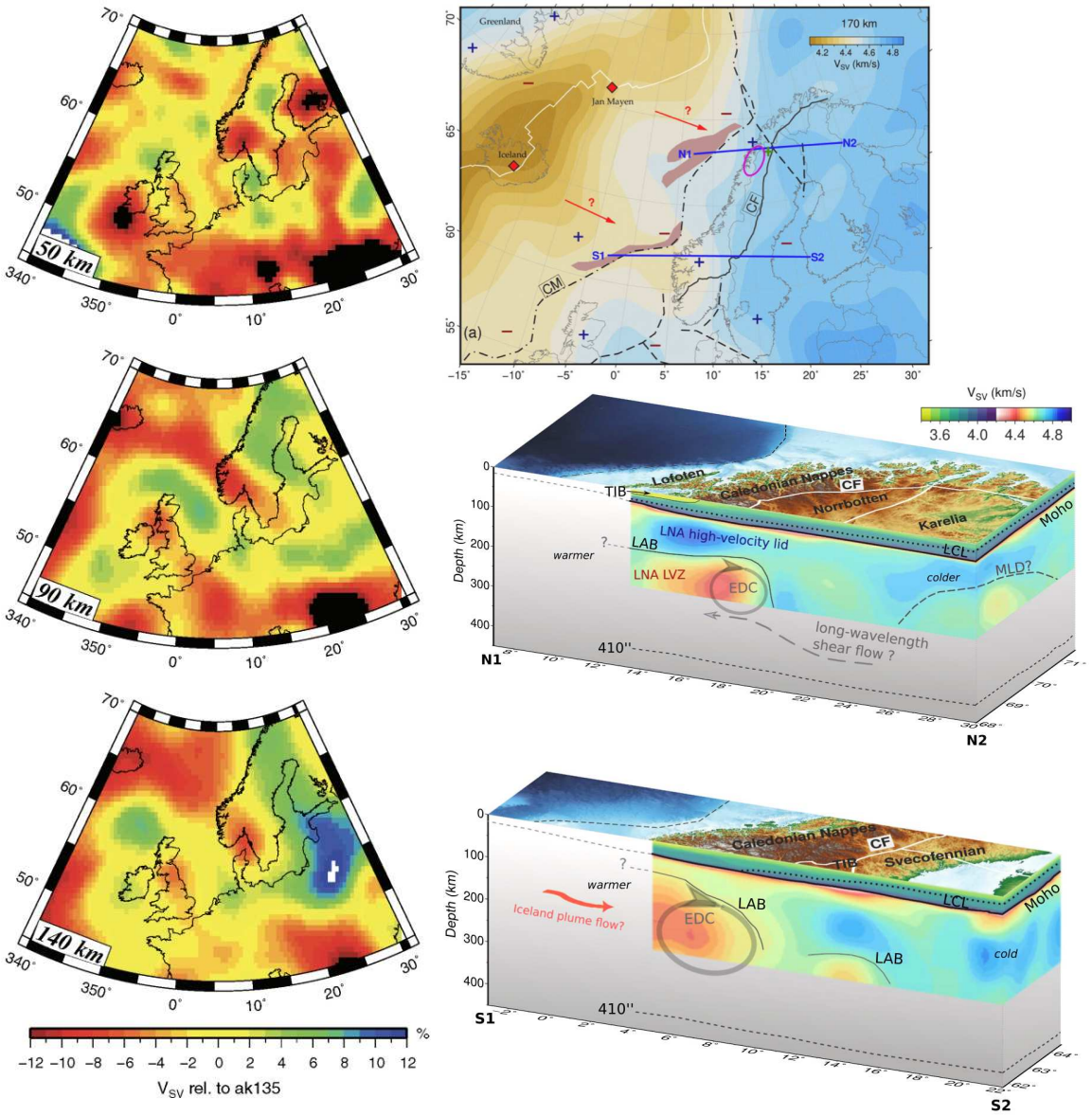

(a) (Weidle & Maupin, 2008) **(b)** (Mauerberger et al., 2022)

Figure 5.3: V_S reprinted results showing possible Iceland Plume connection. (a) Reprinted from Weidle and Maupin (2008, Figure 14); (b) Reprinted from Mauerberger et al. (2022, Figure 17) with top image showing global shear wave speeds from Schaeffer and Lebedev (2013) at 170 km depth; *CF = Caledonian [Deformation] Front, EDC = Edge-driven convection, LAB = Lithosphere Asthenosphere boundary; (ignore other entries).*

from the Iceland Plume. There is a growing body of multi-disciplinary geophysical evidence (e.g., Schoonman et al., 2017) that continue to make this interpretation quite attractive, but it has yet to shown incontrovertible.

In contrast, we do not observe a similar distribution of elevated temperatures beneath the northern Scandes as we do in the southern (Figure 5.4). This is perhaps not surprising given the body of evidence from gravity modeling that point towards primarily crustal compensation in a mixed Airy-Pratt model (e.g., Ebbing and Olesen, 2005; Ebbing, 2007), or more recently lateral variation of eclogite grade (Kahraman et al., 2025). But because we do find areas of elevated temperatures, the possibility remains for mantle contribution able to isostatically balance remaining gravity residuals. This remains speculative though. More surprising are the elevated temperatures found beneath the Lofoten region (see Figure 5.4), but the lack of high topography is considerably puzzling in this regard. Gradmann and Ebbing (2015) suggest a structural origin is most likely when considering a similar conjugate gravity anomaly in Greenland. Mauerberger et al. (2022) conversely find that upper mantle contributions are necessary to invoke with what they interpret as an eroded crustal root. Integration of our temperature results with isostatic modeling would further help to resolve this.

The higher temperature ribbon ("LVR", Figure 5.4) in the Svecofennian and Archean domain would be quite problematic if true mantle thermal structure because, unlike the Scandes, we do not observe a significant topographic expression there. We instead attribute this feature to a high density lower crustal layer unaccounted for by the Moho geometry used in the inversion. Higher velocities in the lower crust are still lower velocities than would-be mantle structures. Korja et al. (1993) propose the existence of this generally westward thickening layer from active source data ~40 – 65 km deep, where depth-to and thickness-of the layer are found to be laterally varying (Figure 5.5). Ebbing (2007) defines a similar layer in an isostatic balance of the Scandes by forward gravity modeling, and more recent tomographic imaging by Mauerberger et al. (2022) quantifying its existence too.

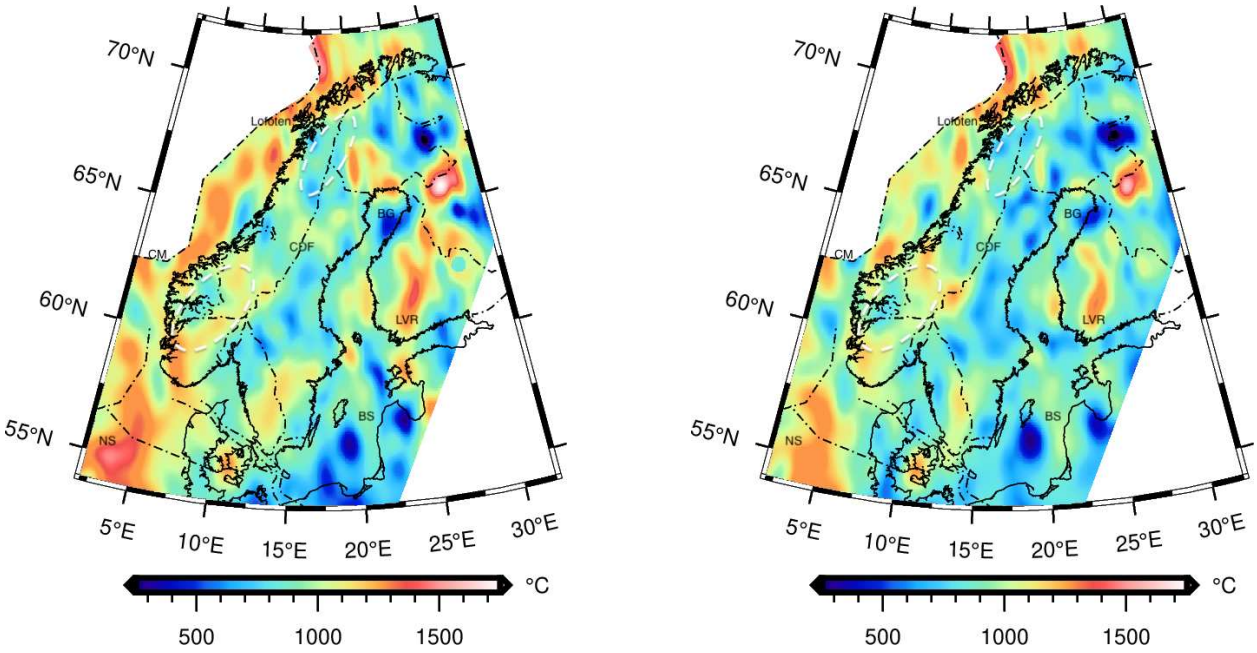

(a) Temperature [60 km] **(b)** Temperature [70 km]

Figure 5.4: Temperature results; (see Figure 4.4 for full description). The Scandes southern and northern domes are outlined by white hash marks. *BG = Bothnian Gulf, BS = Baltic Sea, CDF = Caledonian Deformation Front, CM = Continental Margin, LVR = low velocity ribbon, NS = North Sea.*

Our observed low velocities in central and northern Finland (see "LVR", Figure 5.5b) correlate well with those of Bannister et al. (1991), Bruneton et al. (2004), and Latif (2012) (Figure 5.6). Bannister et al. (1991) attribute these low velocities to variation of Poisson's ratio, because they appear more pronounced on inverted shear wave structure. Comparison with other tomographic studies utilizing shear waves or waveforms finds this lower velocity feature similarly pronounced (e.g., Weidle and Maupin, 2008; Zhu et al., 2015). However, Bruneton et al. (2004) points to a strong spatial correlation of these velocities with that of the high density lower crustal layer. Moreover, our results spatially correlate well with the "crustal modifier" term introduced by Latif (2012) (see Figure 5.6d). This term is not directly tied to layer thickness but can be interpreted from their methodology as propagation time unaccounted for by the a priori crustal structure. Again, this would suggest we are likely imaging this layer and our temperatures based on SCLM derived xenolithes not appropriate.

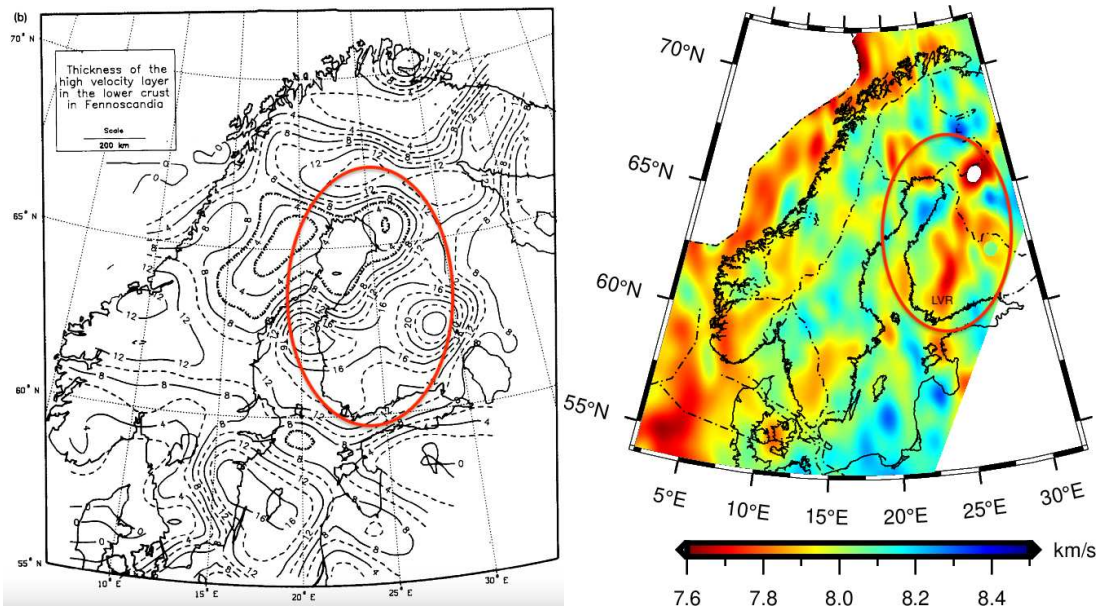

(a) (Korja et al., 1993) **(b)** V_P [60 km]

Figure 5.5: Lower crustal layer. (a) Layer thickness reprinted from Korja et al. (1993, Figure 4b). (b) Our V_P results (see Figure 4.4 for full description); *LVR = low velocity ribbon*. Red oval outline consistent with Figure 5.6.

A notable exception to our mapped thermal structure is that of Artemieva et al. (2006) (Figure 5.7). In generating a global model, they utilize surface heat flow measurements where able, but otherwise assume statistical values assigned from lithospheric ages. The latter is the case they mostly apply to Scandinavian lithosphere. Though our thermal magnitudes differ quite substantially, we do find a general agreement of colder trending temperatures towards the interior of the craton. Moreover, our results present a higher resolution and direct sampling of the Scandinavian uppermost mantle.

Finally, it is worth noting that in assuming velocities directly map to thermal structures we potentially exclude contributions from variations in composition. As Poupinet et al. (2003) points out for stabilized continental lithosphere, shorter wavelength features are unexplainable by thermal modulations. However, assessing the relative contribution of composition across regional scales is likely to prove challenging with mantle xenolithes providing only spot-like sampling. Thus, greater integration of petrological studies with seismic imaging is needed to fully characterize the highly heterogeneous uppermost mantle beneath Scandinavia.

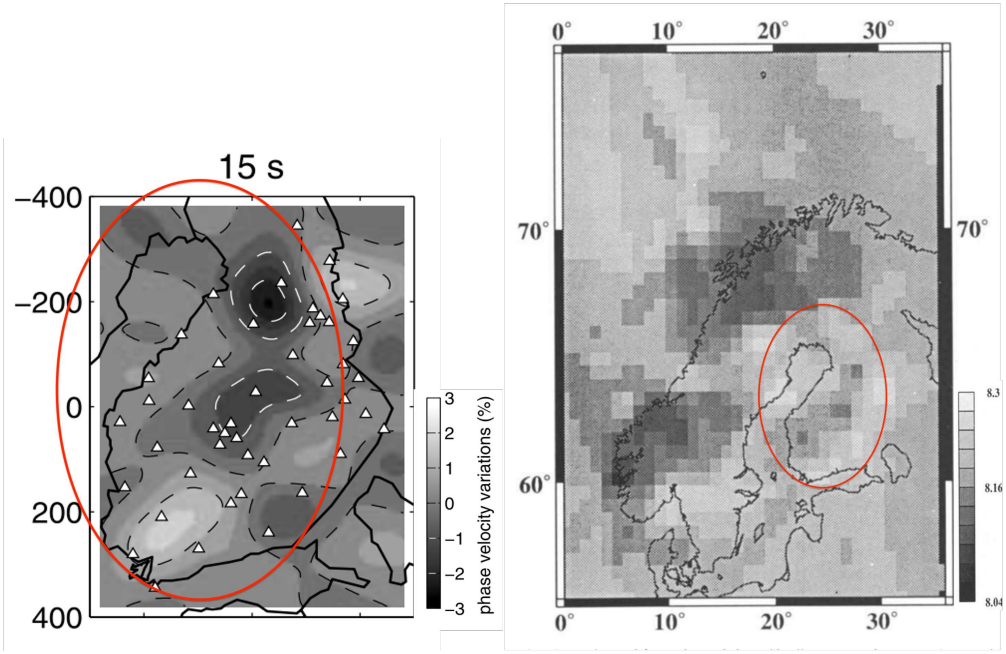

(a) (Bruneton et al., 2004) **(b)** (Bannister et al., 1991)

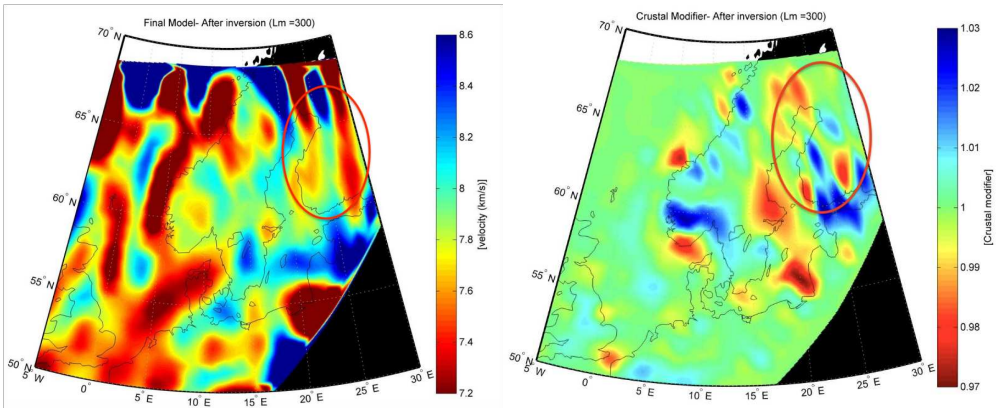

(c) (Latif, 2012) [V_P] **(d)** (Latif, 2012) [Crustal Modifier]

Figure 5.6: Results comparison. (a) Reprinted from Bruneton et al. (2004, Figure 4) (b) Reprinted from Bannister et al. (1991, Figure 7); (c) Reprinted from Latif (2012, Figure 5.1). (d) Reprinted from Latif (2012, Figure 5.6). Red oval outline consistent with Figure 5.5.

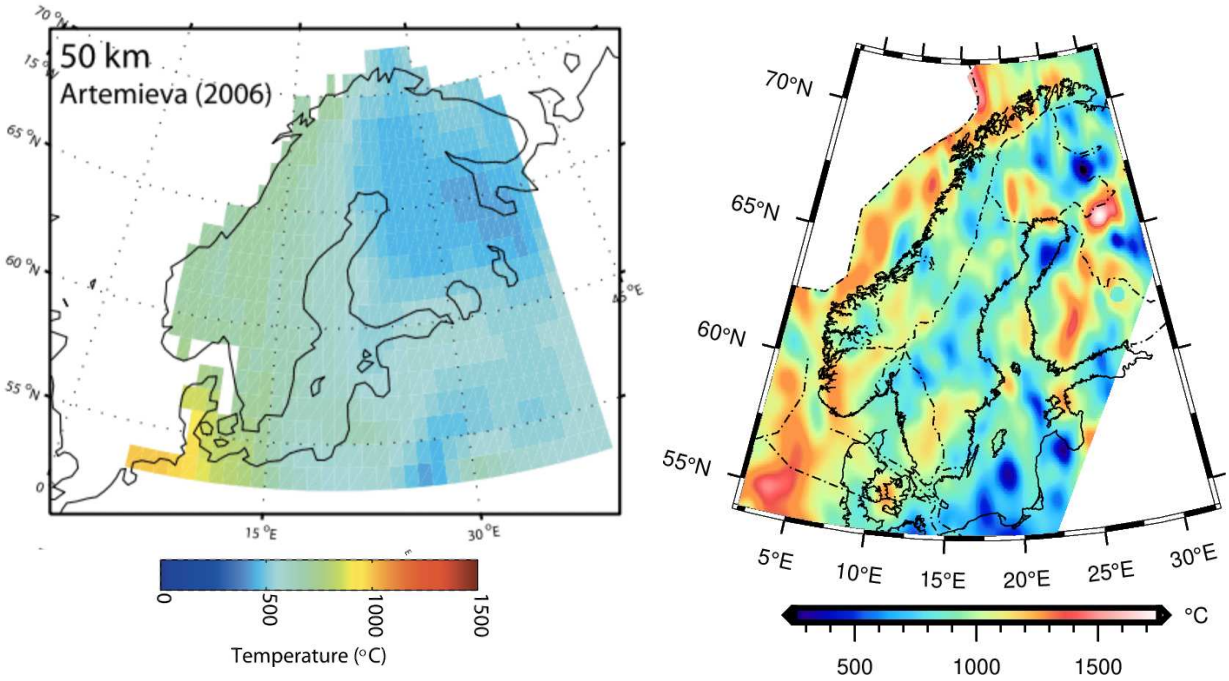

(a) (Artemieva et al., 2006) [50 km]

(b) Temperature [60 km]

Figure 5.7: Temperature results comparison. (a) Reprinted from Barnhoorn et al. (2011, Figure 1) who show results from Artemieva et al. (2006); (b) Our temperature results (see Figure 4.4 for full description).

Chapter 6

6.1 Conclusion

We present a new high-resolution tomographic image of the Scandinavian uppermost mantle from Pn traveltime tomography. We utilize 169,936 ISC Pn picks as observational data input to the Fast Marching Tomography package "FMTOMO". Across five iterative updates to a 3D reference model, we achieve a 63.3% data variance reduction. Moreover, a qualitative assessment of our model resolution from "checkerboard" tests demonstrates our final results interpretable at scales of 2 x 2° or better. Our results for V_P and derived temperature structures show remarkable heterogeneity even at uppermost mantle depths of 60 and 70 km. We confirm prior work suggesting dynamic mantle contribution to the topography of the southern Scandes and discuss implications relating the Iceland plume as a mechanism responsible. Temperatures we find beneath the northern Scandes instead indicate only minor mantle support, as has been suggested by a mixed form of Airy-Pratt Isostasy. Curiously, elevated temperatures beneath the Lofoten Peninsula require further characterization from geophysical studies. In the Svecofennian and Archean domains, we image a low velocity ribbon spatially correlated to a high-density lower crustal layer. We attribute its inclusion as being unaccounted for by the imposed Moho geometry. Finally, we find elevated temperatures relating to Jurassic doming in the North Sea and Cenozoic opening of the North Atlantic.

6.2 Future Work

This thesis presents a high resolution image of Scandinavian uppermost mantle structures. Elastic parameters of velocity and temperature are explored, but further work is needed to integrate the host of available geophysical data, models at depth, and other observations aimed at unraveling the complex tectonic history of the region.

A natural progression of this work, and likely eventual use, is integrating isostatic modeling of density structures derived from our thermal model. A study by Kahraman et al. (2025) do this itera-

tively with gravity along a 2D active source transect of the northern Scandes and find good fit with Bouguer anomalies. Gravity studies aimed at isostatic compensation of the Scandes Mountains have long called for an additional upper mantle component to explain gravity anomaly residuals (e.g., Ebbing and Olesen, 2005; Ebbing et al., 2012; Ebbing, 2007). The level of heterogeneity found and details presented in our results could contribute greatly to the ongoing conversation regarding the enigmatic topography of the Scandes and by extent other remnant fossil mountains.

Further work is needed to identify the most appropriate set of initial conditions. The extent to which an initial reference velocity model plays in the final model is explored briefly in Chapter 4 with the use of ak135, a 1D spherically averaged earth model (Kennett, 2005). FMTOMO's inversion scheme necessitates a good starting model well representing longer wavelength structures (Sun & Kennett, 2016b). Similar projects using FMTOMO for Pn tomography have instead used a global upper mantle shear wave model (e.g., Schaeffer and Lebedev, 2013) and conversion to V_P by regional empirical formulae (e.g., Sun and Kennett, 2016b). Conversion between elastic parameters therefore also contributes to the initial set of conditions.

It may be worth considering also the assumptions imposed by the Moho interface. Pn wavefronts in FMTOMO are implicitly tracked to the Moho interface and then reinitialized in the subsequent layer as a mantle head wave. The choice of interface therefore modulates the Pn critical refraction point and by consequence the model resolution capabilities. An alternative Moho model often used is that of Crust 1.0, a global 1 x 1° crustal structure model (Laske et al., 2013). Regionally, there are many smaller Moho models derived from combined data classes or interpolations between seismic lines. They all differ somewhat based on their interpretation of the Moho (e.g., seismic discontinuity, petrological, thermogenic, etc.). Given appropriate seismic phases and raypath coverage, it may be worth also inverting for the Moho as a separate parameter class.

Finally, collection and implementation of further data is always warranted. This can potentially include the addition of crustal or teleseismic phases to extend out the depth resolution of the tomographic image. Additionally, one's own arrival time picking would produce higher quality data and with known errors, likely leading to a greater convergence between predicted and observed values.

The obvious limitation to implementing these is the already heavy computational cost associated with a large volume of observational data. Running the forward solver in parallel is therefore an effective solution to mitigating long run times. A script exists to perform this but is mechanically challenging to implement with our present computer set up.

References

Anell, I., Thybo, H., & Artemieva, I. (2009). Cenozoic uplift and subsidence in the North Atlantic region: Geological evidence revisited. *Tectonophysics*, *474*(1-2), 78–105.

Artemieva, I. M., Thybo, H., & Kaban, M. K. (2006). Deep Europe today: geophysical synthesis of the upper mantle structure and lithospheric processes over 3.5 Ga. In *European lithosphere dynamics* (pp. 11–41). Geological Society of London.

Aster, R. C., Borchers, B., & Thurber, C. H. (2018). *Parameter estimation and inverse problems*. Elsevier.

Bannister, S., Ruud, B., & Husebye, E. (1991). Tomographic estimates of sub-Moho seismic velocities in Fennoscandia and structural implications. *Tectonophysics*, *189*(1-4), 37–53.

Barnhoorn, A., van der Wal, W., Vermeersen, B. L., & Drury, M. R. (2011). Lateral, radial, and temporal variations in upper mantle viscosity and rheology under Scandinavia. *Geochemistry, geophysics, geosystems*, *12*(1).

Beyer, E. E., Griffin, W. L., & O'Reilly, S. Y. (2006). Transformation of Archaean lithospheric mantle by refertilization: evidence from exposed peridotites in the Western Gneiss Region, Norway. *Journal of Petrology*, *47*(8), 1611–1636.

Brocher, T. M. (2005). Empirical relations between elastic wavespeeds and density in the Earth's crust. *Bulletin of the seismological Society of America*, *95*(6), 2081–2092.

Bruneton, M., Pedersen, H. A., Farra, V., Arndt, N. T., Vacher, P., Achauer, U., Alinaghi, A., Ansorge, J., Bock, G., Friederich, W., et al. (2004). Complex lithospheric structure under the central Baltic Shield from surface wave tomography. *Journal of Geophysical Research: Solid Earth*, *109*(B10).

Buehler, J. S., & Shearer, P. M. (2010). Pn tomography of the western United States using USArray. *Journal of Geophysical Research: Solid Earth*, *115*(B9).

Cawood, P. A., & Pisarevsky, S. A. (2017). Laurentia-baltica-amazonia relations during rodinia assembly. *Precambrian Research*, *292*, 386–397.

Celli, N. L., Lebedev, S., Schaeffer, A. J., & Gaina, C. (2021). The tilted Iceland Plume and its effect on the North Atlantic evolution and magmatism. *Earth and Planetary Science Letters*, *569*, 117048.

Connolly, J. (1990). Multivariable phase diagrams; an algorithm based on generalized thermodynamics. *American Journal of Science*, *290*(6), 666–718.

de Kool, M., Rawlinson, N., & Sambridge, M. (2006). A practical grid-based method for tracking multiple refraction and reflection phases in three-dimensional heterogeneous media. *Geophysical Journal International*, *167*(1), 253–270.

Ebbing, J., England, R., Korja, T., Lauritsen, T., Olesen, O., Stratford, W., & Weidle, C. (2012). Structure of the Scandes lithosphere from surface to depth. *Tectonophysics*, *536*, 1–24.

Ebbing, J., & Olesen, O. (2005). The Northern and Southern Scandes—structural differences revealed by an analysis of gravity anomalies, the geoid and regional isostasy. *Tectonophysics*, *411*(1-4), 73–87.

Ebbing, J. (2007). Isostatic density modelling explains the missing root of the Scandes. *Norwegian Journal of Geology/Norsk Geologisk Forening*, *87*.

Forte, A. M., & Rowley, D. B. (2022). Earth's isostatic and dynamic topography—A critical perspective. *Geochemistry, Geophysics, Geosystems*, *23*(9), e2021GC009740.

Gaál, G., & Gorbatschev, R. (1987). An outline of the Precambrian evolution of the Baltic Shield. *Precambrian research*, *35*, 15–52.

Gabrielsen, R. H., Braathen, A., Olesen, O., Faleide, J. I., Kyrkjebø, R., & Redfield, T. F. (2005). Vertical movements in south-western Fennoscandia: a discussion of regions and processes from the Present to the Devonian. In *Norwegian petroleum society special publications* (pp. 1–28, Vol. 12). Elsevier.

Goes, S., Govers, R., Vacher, & P. (2000). Shallow mantle temperatures under Europe from P and S wave tomography. *Journal of Geophysical Research: Solid Earth*, *105*(B5), 11153–11169.

Gorbatschev, R., & Bogdanova, S. (1993). Frontiers in the Baltic shield. *Precambrian Research*, *64*(1-4), 3–21.

Grad, M., Tiira, T., & Group, E. W. (2009). The Moho depth map of the European Plate. *Geophysical journal international*, *176*(1), 279–292.

Gradmann, S., & Ebbing, J. (2015). Large-scale gravity anomaly in northern Norway: tectonic implications of shallow or deep source depth and a possible conjugate in northeast Greenland. *Geophysical Supplements to the Monthly Notices of the Royal Astronomical Society*, *203*(3), 2070–2088.

Hearn, T., Beghoul, N., & Barazangi, M. (1991). Tomography of the western United States from regional arrival times. *Journal of Geophysical Research: Solid Earth*, *96*(B10), 16369–16381.

Högdahl, K., Andersson, U. B., & Eklund, O. (2004). *The Transscandinavian Igneous Belt (TIB) in Sweden: a review of its character and evolution* (Vol. 37). Geological survey of Finland Espoo.

Husebye, H., Hovland, J., Christoffersson, A., Åström, K., Slunga, R., & Lund, C.-E. (1986). Tomographical mapping of the lithosphere and asthenosphere beneath southern Scandinavia and adjacent areas. *Tectonophysics*, *128*(3-4), 229–250.

ISC. (2006-2023). International Seismological Centre. https://doi.org/10.31905/D808B830

Jackson, I., & Faul, U. H. (2010). Grainsize-sensitive viscoelastic relaxation in olivine: Towards a robust laboratory-based model for seismological application. *Physics of the Earth and Planetary Interiors*, *183*(1-2), 151–163.

Jennings, E. S., & Holland, T. J. (2015). A simple thermodynamic model for melting of peridotite in the system NCFMASOCr. *Journal of Petrology*, *56*(5), 869–892.

Kahraman, M., Thybo, H., Artemieva, I. M., Shulgin, A., Hedin, P., & Mjelde, R. (2025). Northern Scandinavian mountains supported by a low-grade eclogitic crustal keel. *Nature communications*, *16*(1), 1–13.

Kennett, B. (2005). Seismological tables: ak135. *Research School of Earth Sciences, Australian National University Canberra, Australia*, 1–289.

King, S. D., & Anderson, D. L. (1998). Edge-driven convection. *Earth and Planetary Science Letters*, *160*(3-4), 289–296.

Korja, A., Korja, T., Luosto, U., & Heikkinen, P. (1993). Seismic and geoelectric evidence for collisional and extensional events in the Fennoscandian Shield implications for Precambrian crustal evolution. *Tectonophysics*, *219*(1-3), 129–152.

Lahtinen, R., & Huhma, H. (2019). A revised geodynamic model for the Lapland-Kola orogen. *Precambrian Research*, *330*, 1–19.

Lahtinen, R., Korja, A., & Nironen, M. (2005). Paleoproterozoic tectonic evolution. In *Developments in precambrian geology* (pp. 481–531, Vol. 14). Elsevier.

Laske, G., Masters, G., Ma, Z., & Pasyanos, M. (2013). Update on CRUST1. 0—A 1-degree global model of Earth's crust. *Geophysical research abstracts*, *15*(15), 2658.

Latif, A. (2012). *Tomographic inversion of Pn waves beneath southern Scandinavia: a study to reveal the upper mantle velocity structure to explain anomalous topography of Scandinavian Mountains* [Master's thesis].

Makushkina, A., Tauzin, B., Tkalčić, H., & Thybo, H. (2019). The mantle transition zone in Fennoscandia: Enigmatic high topography without deep mantle thermal anomaly. *Geophysical Research Letters*, *46*(7), 3652–3662.

Mauerberger, A., Sadeghisorkhani, H., Maupin, V., Gudmundsson, Ó., & Tilmann, F. (2022). A shear-wave velocity model for the Scandinavian lithosphere from Rayleigh waves and ambient noise-Implications for the origin of the topography of the Scandes mountain range. *Tectonophysics*, *838*, 229507.

Maupin, V., Agostini, A., Artemieva, I., Balling, N., Beekman, F., Ebbing, J., England, R., Frassetto, A., Gradmann, S., Jacobsen, B., et al. (2013). The deep structure of the Scandes and its relation to tectonic history and present-day topography. *Tectonophysics*, *602*, 15–37.

Maupin, V. (2011). Upper-mantle structure in southern Norway from beamforming of Rayleigh wave data presenting multipathing. *Geophysical Journal International*, *185*(2), 985–1002.

Medhus, A., Balling, N., Jacobsen, B., Weidle, C., England, R., Kind, R., Thybo, H., & Voss, P. (2012). Upper-mantle structure beneath the Southern Scandes Mountains and the Northern

Tornquist Zone revealed by P-wave traveltime tomography. *Geophysical Journal International*, *189*(3), 1315–1334.

Medhus, A., Balling, N., Holm Jacobsen, B., Kind, R., & England, R. W. (2009). Deep-structural differences in southwestern Scandinavia revealed by P-wave travel time residuals. *Norwegian Journal of Geology/Norsk Geologisk Forening*, *89*(3).

Molnar, P., England, P. C., & Jones, C. H. (2015). Mantle dynamics, isostasy, and the support of high terrain. *Journal of Geophysical Research: Solid Earth*, *120*(3), 1932–1957.

Neumann, E.-R., Wilson, M., Heeremans, M., Spencer, E. A., Obst, K., Timmerman, M. J., & Kirstein, L. (2004). Carboniferous-Permian rifting and magmatism in southern Scandinavia, the North Sea and northern Germany: a review. *Geological Society, London, Special Publications*, *223*.

Nielsen, S. B., Gallagher, K., Leighton, C., Balling, N., Svenningsen, L., Jacobsen, B. H., Thomsen, E., Nielsen, O. B., Heilmann-Clausen, C., Egholm, D. L., et al. (2009). The evolution of western Scandinavian topography: a review of Neogene uplift versus the ICE (isostasy–climate–erosion) hypothesis. *Journal of Geodynamics*, *47*(2-3), 72–95.

Nordmann, A. (2007). *Refraction - Huygens-Fresnel principle*.[Photograph]. Wikipedia. https://en.wikipedia.org/wiki/Huygens%E2%80%93Fresnel_principle

O'Reilly, S. Y., & Griffin, W. (2013). Moho vs crust–mantle boundary: Evolution of an idea. *Tectonophysics*, *609*, 535–546.

Pharaoh, T., England, R., Verniers, J., & Żelaźniewicz, A. (1997). Introduction: geological and geophysical studies in the Trans-European Suture Zone. *Geological Magazine*, *134*(5), 585–590.

Poupinet, G., Arndt, N., & Vacher, P. (2003). Seismic tomography beneath stable tectonic regions and the origin and composition of the continental lithospheric mantle. *Earth and Planetary Science Letters*, *212*(1-2), 89–101.

Rawlinson, N., de Kool, M., & Sambridge, M. (2006). Seismic wavefront tracking in 3D heterogeneous media: applications with multiple data classes. *Exploration Geophysics*, *37*(4), 322–330.

Rawlinson, N., Reading, A. M., & Kennett, B. L. (2006). Lithospheric structure of Tasmania from a novel form of teleseismic tomography. *Journal of Geophysical Research: Solid Earth*, *111*(B2).

Rawlinson, N., & Sambridge, M. (2003). Seismic traveltime tomography of the crust and lithosphere. *Advances in geophysics*, *46*, 81–199.

Rawlinson, N., & Urvoy, M. (2006). Simultaneous inversion of active and passive source datasets for 3-D seismic structure with application to Tasmania. *Geophysical Research Letters*, *33*(24).

Rawlinson, N., & Sambridge, M. (2004a). Multiple reflection and transmission phases in complex layered media using a multistage fast marching method. *Geophysics*, *69*(5), 1338–1350.

Rawlinson, N., & Sambridge, M. (2004b). Wave front evolution in strongly heterogeneous layered media using the fast marching method. *Geophysical Journal International*, *156*(3), 631–647.

Rawlinson, N., & Spakman, W. (2016). On the use of sensitivity tests in seismic tomography. *Geophysical Journal International*, *205*(2), 1221–1243.

Roberts, D. (2003). The Scandinavian Caledonides: event chronology, palaeogeographic settings and likely modern analogues. *Tectonophysics*, *365*(1-4), 283–299.

Rohrman, M., & van der Beek, P. (1996). Cenozoic postrift domal uplift of North Atlantic margins: an asthenospheric diapirism model. *Geology*, *24*(10), 901–904.

Sambridge, M. (1990). Non-linear arrival time inversion: constraining velocity anomalies by seeking smooth models in 3-D. *Geophysical Journal International*, *102*(3), 653–677.

Saunders, A., Fitton, J., Kerr, A., Norry, M., & Kent, R. (1997). The North Atlantic Igneous Province. *Large Igneous Provinces: Continental, Oceanic, and Planetary Flood Volcanism*, *100*, 45–93.

Schaeffer, A., & Lebedev, S. (2013). Global shear speed structure of the upper mantle and transition zone. *Geophysical Journal International*, *194*(1), 417–449.

Schoonman, C., White, N., & Pritchard, D. (2017). Radial viscous fingering of hot asthenosphere within the Icelandic plume beneath the North Atlantic Ocean. *Earth and Planetary Science Letters*, *468*, 51–61.

Schutt, D. L., & Lesher, C. E. (2006). Effects of melt depletion on the density and seismic velocity of garnet and spinel lherzolite. *Journal of Geophysical Research: Solid Earth*, *111*(B5).

Schutt, D. L., & Lesher, C. E. (2010). Compositional trends among Kaapvaal Craton garnet peridotite xenoliths and their effects on seismic velocity and density. *Earth and Planetary Science Letters*, *300*(3-4), 367–373.

SEG. (2014). *The eikonal equation*. SEG Wiki. https://wiki.seg.org/wiki/The_eikonal_equation

Sethian, J. A. (1996). A fast marching level set method for monotonically advancing fronts. *proceedings of the National Academy of Sciences*, *93*(4), 1591–1595.

Sethian, J. A. (2006). *Level Set Methods: An initial value formulation*. math.berekeley.edu. https://math.berkeley.edu/~sethian/2006/Explanations/level_set_explain.html

Shomali, Z. H., Roberts, R. G., Pedersen, L. B., Group, T. W., et al. (2006). Lithospheric structure of the Tornquist Zone resolved by nonlinear P and S teleseismic tomography along the TOR array. *Tectonophysics*, *416*(1-4), 133–149.

Smelror, M., Dehls, J., Ebbing, J., Larsen, E., Lundin, E. R., Nordgulen, Ø., Osmundsen, P. T., Olesen, O., Ottesen, D., Pascal, C., et al. (2007). Towards a 4D topographic view of the Norwegian sea margin. *Global and Planetary Change*, *58*(1-4), 382–410.

Smit, J., van Wees, J.-D., & Cloetingh, S. (2016). The Thor suture zone: from subduction to intraplate basin setting. *Geology*, *44*(9), 707–710.

Storchak, D. A., Schweitzer, J., & Bormann, P. (2003). The IASPEI standard seismic phase list. *Seismological Research Letters*, *74*(6), 761–772.

Stratford, W., Thybo, H., Faleide, J. I., Olesen, O., & Tryggvason, A. (2009). New Moho map for onshore southern Norway. *Geophysical Journal International*, *178*(3), 1755–1765.

Sun, W., & Kennett, B. (2016a). Uppermost mantle structure beneath eastern China and its surroundings from Pn and Sn tomography. *Geophysical Research Letters*, *43*(7), 3143–3149.

Sun, W., & Kennett, B. (2016b). Uppermost mantle structure of the Australian continent from Pn traveltime tomography. *Journal of Geophysical Research: Solid Earth*, *121*(3), 2004–2019.

Svenningsen, L., Balling, N., Jacobsen, B., Kind, R., Wylegalla, K., & Schweitzer, J. (2007). Crustal root beneath the highlands of southern Norway resolved by teleseismic receiver functions. *Geophysical Journal International*, *170*(3), 1129–1138.

Underhill, J. R., & Partington, M. (1993). Jurassic thermal doming and deflation in the North Sea: implications of the sequence stratigraphic evidence. *Geological Society, London, Petroleum Geology Conference Series*, *4*(1), 337–345.

Vidale, J. (1988). Finite-difference calculation of travel times. *Bulletin of the seismological society of America*, *78*(6), 2062–2076.

Weidle, C., & Maupin, V. (2008). An upper-mantle S-wave velocity model for Northern Europe from Love and Rayleigh group velocities. *Geophysical Journal International*, *175*(3), 1154–1168.

Wylegalla, K., Bock, G., Gossler, J., Hanka, W., Group, T. W., et al. (1999). Anisotropy across the Sorgenfrei–Tornquist Zone from shear wave splitting. *Tectonophysics*, *314*(1-3), 335–350.

Zhu, H., Bozdağ, E., & Tromp, J. (2015). Seismic structure of the European upper mantle based on adjoint tomography. *Geophysical Journal International*, *201*(1), 18–52.

Ziegler, P. (1992). North Sea rift system. *Tectonophysics*, *208*(1-3), 55–75.

Appendix A

FMTOMO Documentation

The goal for this documentation is to detail the choices we make in the Fast Marching Tomography package FMTOMO and how to similarly achieve them. Credit for FMTOMO belongs to de Kool et al. (2006), Rawlinson, de Kool, and Sambridge (2006), and Rawlinson and Urvoy (2006). Additionally contained in the distribution of FMTOMO software is an instructions manual containing generic input files, parts of which we include in subsequent documentation. We also include MATLAB and Bash scripts that are our own.

A.1 Documentation: FMTOMO Directory Set up

Overview: The goal of this documentation is to provide an overview for how to execute FMTOMO commands with a *run.bash* script.

Example Directory Structure

We find a *Base-, Root-,* and *Run-* directory structure optimal for consistency across model runs and updated input files. We present an example of our directory set-up in Figure A.1. To be able to execute FMTOMO commands from any directory, open or create an "*.rc*" file and type "*setenv PATH $PATH:/usr/local/ bin/grid3dg*". This will place all needed FMTOMO commands in your */usr/local/bin/*.

X2Go

X2Go is a remote access desktop for accessing Linux computers. We perform all of our runs on CSU's Warner College computers which require constant connection. We use X2Go to connect to their remote desktops and from there open a command terminal to run FMTOMO. The remote desktops remain running once called, which is important for FMTOMO runs that last for days.

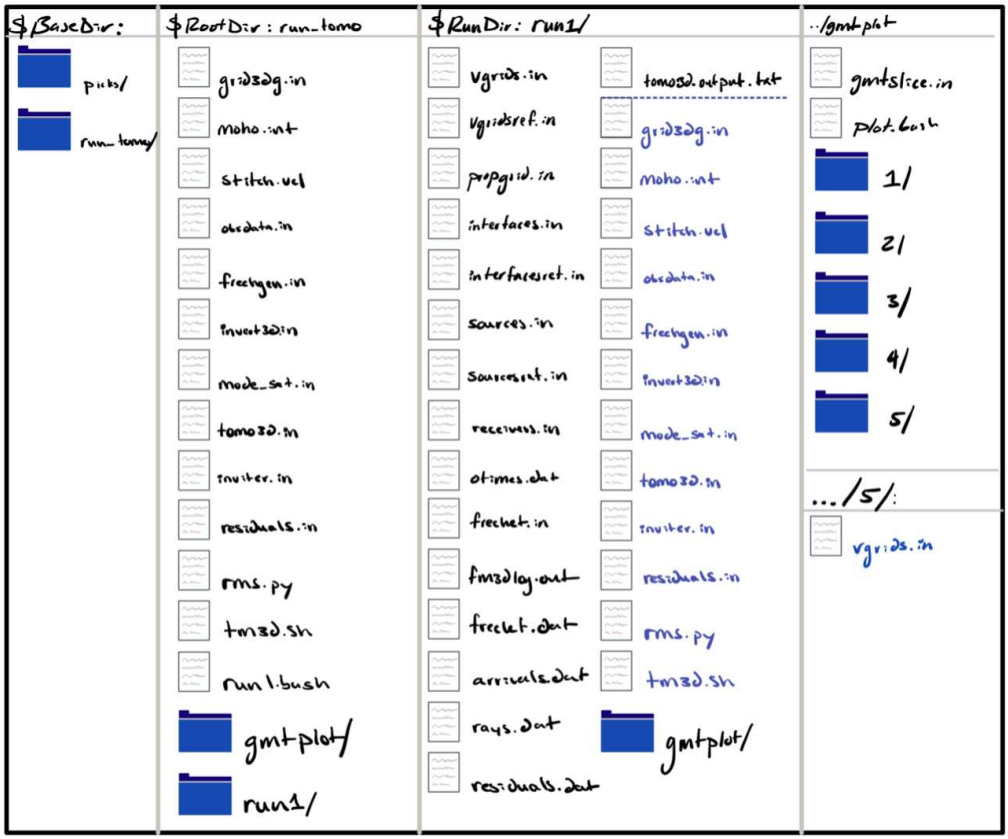

Figure A.1: Example directory set up following a *Base-, Root-, and Run-* file tree structure. Input files (black color labels) in the *Base-* and *Root-* directory, and output files (blue color labels) in the *Run-*directory are explained throughout the Appendix.

X2Go also has Gedit which makes manipulating input files much easier than in the command line environment.

run.bash

The motivation behind a *run.bash* script is to automate FMTOMO inputs and direct outputs to an appropriate directory. When running simultaneous runs we find it desirable to copy in variations of input files as their default file name found in the FMTOMO manual. An example of *run.bash* is shown below. In your *Base-*directory enter the command "*chmnod +x run.bash*" to convert it to an executable. Then enter "*./run.bash*".

It is also best practice to begin with a simple design and then modify the script to greater complexity. Test that the *run.bash* script by inputting manually each line to the terminal and

viewing the output. Start with less data to more quickly test the functions and use the built-in model parameters like the 1D gradient velocity and flat interface generator before testing input files. Test at a courser resolution and for less iterations while building your debugging intuition.

```
#!/bin/bash -vx
RootDir="/data/geo/seismo/Research/josh_pn"
BaseDir="$RootDir/run_tomo"
RunDir="$BaseDir/run1"

rm -rf $RunDir
[ ! -d "$RunDir" ] && mkdir "$RunDir"
cd $RunDir

#
cp $BaseDir/grid3dg.in $RunDir
cp $BaseDir/moho.int $RunDir
cp $BaseDir/stitch.vel $RunDir
grid3dg # this produces vgrids.in, propgrid.in, interfaces.in

cp vgrids.in vgridsref.in
cp interfaces.in interfacesref.in

#
cp -r $RootDir/picks_switched_sm $RunDir/picks
cp $RunDir/picks/sourcespn.in $RunDir
cp $BaseDir/obsdata.in $RunDir
obsdata  # this creates otimes.dat, sources.in ,and receivers.in

cp $RunDir/sources.in $RunDir/sourcesref.in

#
cp $BaseDir/frechgen.in $RunDir
cp $BaseDir/invert3d.in $RunDir
cp $BaseDir/mode_set.in $RunDir
cp $BaseDir/tomo3d.in $RunDir
cp $BaseDir/inviter.in $RunDir
cp $BaseDir/residuals.in $RunDir
cp $BaseDir/rms.py $RunDir
cp -r $BaseDir/gmtplot $RunDir

cp $BaseDir/tm3d.sh $RunDir
./tm3d.sh >& tomo3d.output.txt
```

A.2 Documentation: Data Scrubbing & Culling

Overview: The goal of this documentation is to provide details for reading in an ISC data text file and outputting FMTOMO input files.

MATLAB functions and scripts

Our script *data_FMTOMO.m* reads in ISC data as a table with the function *ISC_ToTable.m* and updates the workspace variables with the function *T_up.m*. The table format accounts for the variety of data-types present (double, categorical, datetime, etc.) and also updates by *T_up.m*. This keeps the working variables separate from the updated ones.

ISC_ToTable.m

```
%% ISC_ToTable.m
function [T] = ISC_ToTable()
    % Set up the Import Options and import the data
    opts = delimitedTextImportOptions("NumVariables", 28);

    % Specify range and delimiter
    opts.DataLines = [1, Inf]; %start on first line, no header
    opts.Delimiter = ",";

    % Specify column names and types
    opts.VariableNames = ["EVENTID", "TYPE", "REPORTER", "STA", "NET", "LAT",
        "LON", "ELEV", "CHN", "DIST", "BAZ", "ISCPHASE", "REPHASE", "DATE", "
        TIME", "RES", "TDEF", "AMPLITUDE", "PER", "AUTHOR", "DATE1", "TIME1",
        "LAT1", "LON1", "DEPTH", "AUTHOR1", "TYPE1", "MAG"];

    opts.VariableTypes = ["double", "categorical", "categorical", "categorical
        ", "categorical", "double", "double", "double", "categorical", "double
        ", "double", "categorical", "categorical", "datetime", "datetime", "
        double", "categorical", "double", "double", "categorical", "datetime",
         "datetime", "double", "double", "double", "categorical", "categorical
        ", "double"];

    % Specify file level properties
    opts.ExtraColumnsRule = "ignore";
    opts.EmptyLineRule = "skip";

    % Specify variable properties
```

```
    opts = setvaropts(opts, ["TYPE", "REPORTER", "STA", "NET", "CHN", "
        ISCPHASE", "REPHASE", "TDEF", "AUTHOR", "AUTHOR1", "TYPE1"], "
        EmptyFieldRule", "auto");
    opts = setvaropts(opts, "DATE", "InputFormat", "yyyy-MM-dd");
    opts = setvaropts(opts, "TIME", "DatetimeFormat", "HH:mm:ss.SS");
    opts = setvaropts(opts, "DATE1", "InputFormat", "yyyy-MM-dd");
    opts = setvaropts(opts, "TIME1", "DatetimeFormat", "HH:mm:ss.SS");

    % Import the data
    T = readtable("~/data_concat.txt", opts);

    %Clear temporary variables
    clear opts
end
```

T_up.m

```
%% T_up.m
%defines/updates variables from table T
function [enum,sname,slat,slon,sELEV,dist,sdate,stime,edate,etime,elat,elon,
    edepth,Pn_time,dist_km] = T_up(T)
    %ARRIVAL DATA (s-staion)
    enum=T.EVENTID;
    sname=T.STA;
    slat=T.LAT; %[dec deg]
    slon=T.LON; %[dec deg]
    sELEV=T.ELEV./1000;  %convert from m to km
    dist=T.DIST; %epicentral dist [dec deg]
    sdate=T.DATE; %[yyyy-MM-dd]
    stime=T.TIME; %[HH:mm:ss.SS]

    %ORIGIN DATA (e-event)
    edate=T.DATE1; %[yyyy-MM-dd]
    etime=T.TIME1; %[HH:mm:ss.SS]
    elat=T.LAT1; %[dec deg]
    elon=T.LON1;%[dec deg]
    edepth=T.DEPTH; %[km]

    % since Pn_time is calculated without the days, need to add 3600*24 to
    % negative cases, where the observed_time looks like it is less than the
    % origin_time, because it occurred on the day previous.
    Pn_time = seconds(stime - etime);
    Pn_time(Pn_time<0)=Pn_time(Pn_time<0)+86400;
```

```
    wgs84 = wgs84Ellipsoid("km");
    dist_km = distance(T.LAT,T.LON,T.LAT1,T.LON1,wgs84);
end
```

data_FMTOMO.m

The Scrubbing and culling procedure we implement in *data_FMTOMO.m* is:

a. Scrub empties & repeats

b. Cull to latitude and longitude boundaries defined in *grid3dg.in*

c. Cull events originating below the Moho

d. Cull to epicentral distances 1.8 – 15°

e. Cull within ±6 s reduced travel time

f. Cull to 5+ event-station ratio

```
%% data_FMTOMO.m
% A note: this script is meant to be run by section advance
%% I -grab data from ~/data.concat
clear;
T = ISC_ToTable; %reads in ISC csv files to Table w/ data types
[enum,sname,slat,slon,sELEV,dist,sdate,stime,...
    edate,etime,elat,elon,edepth,Pn_time,dist_km] = T_up(T);
%% II -delete empties in relevant fields
% (data improperly recorded)
cull = isnan(enum)|isnan(slat)|isnan(slon)|isnan(sELEV)| ...
    isnan(elat)|isnan(elon)|isnan(edepth)|isnan(Pn_time)| ...
    isnat(stime)|isnat(etime);
T(cull,:) = [];
fprintf('Number of empties culled: %d\n ', length(find(cull==1)));
%update vars
[enum,sname,slat,slon,sELEV,dist,sdate,stime,...
    edate,etime,elat,elon,edepth,Pn_time,dist_km] = T_up(T);
%% III -delte repeats (keep first arrival time only)
% (multiple travel times recorded for event-station pairs)
unique_events = unique(enum,"stable"); %unique events
cull=zeros(size(Pn_time));
```

```
for i=1:length(unique_events) %for each event
    index=find(enum==unique_events(i)); %index locations for each event
    k=0; %counter num of picks for each event
    clearvars dumvar_sname;
    %write stations at unique event index loc to dummyvar to work on
    for j= min(index):max(index)
        k=k+1;
        dumvar_sname(k) = sname(j);
    end

    %now look through dumvar
    unique_stations=unique(dumvar_sname,'stable'); %unique sta

    %keep only first arrival time
    for j = 1:length(unique_stations) %for each station
        sta_index = find(dumvar_sname==unique_stations(j)); %sta index
            locations w/in dummyvar
        if length(sta_index)>1 %if sta has multiple entries
            Pn_time_at_sta_index = Pn_time(min(index)+sta_index-1); %grab Pn
                values at sta_index
            keep_pick = min(Pn_time_at_sta_index); %keep the minimum value
            %cull from the main table T index values
            cull(min(index) + -1 + min(sta_index) -1 + find(
                Pn_time_at_sta_index~=keep_pick)) =1;
            %if multiple picks with the same minimum value
            if length(find(Pn_time_at_sta_index==keep_pick)) >1
                %cull to only one entry
                a = find(Pn_time_at_sta_index==keep_pick); %where equal to the
                    same minimum value
                amin = min(a); %the first instance
                cull(min(index) + -1 + min(sta_index) -1 + a(a~=amin)) =1;
            end
        end
    end
end

cull = logical(cull);
T(cull,:) =[];
fprintf('Number of non-first arrivals culled: %d\n ', length(find(cull==1)));
%update vars
[enum,sname,slat,slon,sELEV,dist,sdate,stime,...
    edate,etime,elat,elon,edepth,Pn_time,dist_km] = T_up(T);
%% IV -cull boundary conditions (lat/lon)
cull=zeros(size(elat));
%events
cull(elat<=49|elat>=85 )=1;
```

```
cull(elon<=-37|elon>=41 )=1;
%stations
cull(slat<=49|slat>=85 )=1;
cull(slon<=-37|slon>=41 )=1;
cull = logical(cull);
T(cull,:) =[];
fprintf('Number of lat/lon boundary conditions culled: %d\n ', length(find(
    cull==1)));
%update vars
[enum,sname,slat,slon,sELEV,dist,sdate,stime,...
     edate,etime,elat,elon,edepth,Pn_time,dist_km] = T_up(T);
%% V -cull events beneath the Moho
cull=zeros(size(edepth)); %(+) down
load("F_GRAD_moho.mat"); %(-) down
moho=-F_GRAD_moho(elat,elon);
cull(edepth+1>moho)=1; %added a 1km buffer
cull = logical(cull);
T(cull,:) =[];
fprintf('Number of arrivals from events below the crust culled: %d\n ', length
    (find(cull==1)));
%update vars
[enum,sname,slat,slon,sELEV,dist,sdate,stime,...
     edate,etime,elat,elon,edepth,Pn_time,dist_km] = T_up(T);
%% VI -cull epicentral distance to [1.8-15deg]
cull=zeros(size(dist));
cull(dist < 1.8 | dist > 15 )=1;
cull = logical(cull);
T(cull,:) =[];
fprintf('Number of arrivals from epicentral distances outside 1.8-15deg culled
    : %d\n ', length(find(cull==1)));
%update vars
[enum,sname,slat,slon,sELEV,dist,sdate,stime,...
     edate,etime,elat,elon,edepth,Pn_time,dist_km] = T_up(T);
%% VII -cull +/- 6s traveltime residual about straight line fit
c = polyfit(dist,Pn_time,1); %y = mx+b; c(1) = m, c(2) = b;
Pn_lsqr = polyval(c,dist); %least square value for each dist recording
Pn_misfit = Pn_lsqr - Pn_time; %misfit to the straight line fit
cull=zeros(size(Pn_misfit));
cull(abs(Pn_misfit) >= 6)=1;
cull = logical(cull);
T(cull,:) =[];
fprintf('Number of traveltime residuals outside +/-6s about a straight line
    fit culled: %d\n ', length(find(cull==1)));
%update vars
[enum,sname,slat,slon,sELEV,dist,sdate,stime,...
     edate,etime,elat,elon,edepth,Pn_time,dist_km] = T_up(T);
```

```
%% VIII -cull to 5+ event-station ratio
while ~isempty(find(cull==1, 1))
    %perform this search iteratively until both stations and events 5+
    %ratio is satisfied b/c both logics update independantly
    cull=zeros(size(Pn_time));

    %cull events "enum" which recorded less than 5 travelimes
    unique_events = unique(enum);
    for i=1:length(unique_events)
        n=find(enum==unique_events(i)); %number of travel times recorded for
            an event
        if(length(n)<5)
            cull(n)=1;
        end
    end

    %cull stations which recroded less than 5 events
    unique_stations = unique(sname);
    for i=1:length(unique_stations)
        n=find(sname==unique_stations(i)); %number of events recroded by a
            station
        if(length(n)<5)
            cull(n)=1;
        end
    end

    cull=logical(cull);
    cull = logical(cull);
    T(cull,:) =[];
    fprintf('Number of arrivals culled because of inadequate recording: %d\n '
        , length(find(cull==1)));
    %update vars
    [enum,sname,slat,slon,sELEV,dist,sdate,stime,...
        edate,etime,elat,elon,edepth,Pn_time,dist_km] = T_up(T);
end
%%
save("final_data_table","T");
%% IX -output to FMTOMO & GMT
%Make switched source-receiver files
elat_switched = slat;
elon_switched = slon;
edepth_switched = -sELEV; %make negative to maintain consitency w/ orientation
enum_switched = sname;
slat_switched = elat;
slon_switched = elon;
sELEV_switched = edepth;
```

```
% create sources file.
[status,result]=system('rm ./picks_switched/sourcespn.in');
[status,result]=system('rm ./picks_switched/*.pn');
disp(status)
disp(result)
fid=fopen('picks_switched/sourcespn.in','w');
[C]=unique(enum_switched);
num_events = length(C);
fprintf(fid,'%10d \n',num_events);
for n = 1:num_events
    i = find(enum_switched==C(n));
    fprintf(fid,'%10.6f        %10.6f         %8.2f\n',elat_switched(i(1)),
       elon_switched(i(1)),edepth_switched(i(1)));
    fprintf(fid,'1 \n');
    fname=['pick',num2str(n),'.pn'];
    fprintf(fid,'1 1 %10s \n',fname);

    % create pick files
    fid_pick = fopen(['picks_switched/',fname],'w');
    num_stations = length(i);
    fprintf(fid_pick,'%6d \n',num_stations);
    for in = 1:length(i)
        fprintf(fid_pick,'%10.6f    %10.6f     %8.2f     %8.2f    0.15\n',
           slat_switched(i(in)),slon_switched(i(in)),sELEV_switched(i(in)),
           Pn_time(i(in)) );
    end
    fclose(fid_pick);
end
```

Output to *picks/*

The script *data_FMTOMO.m* outputs to the directory *picks/* the files *sourcespn.in* and *picks.pn*. We have also switched source and receiver geometry because computation time scales with the number of sources. This has no effect on the resolved structures because the raypaths are the same. The computation run-time difference for large amounts of event data like ours is weeks in the normal configuration versus a day in the switched. The orientation for these inputs is negative above the surface and positive with depth.

When writing to output, we find it important to pay attention to the spacing delimiters in the FMTOMO generic input files. Each field will contain a certain number of allowable character

spaces that FMTOMO is expecting to read in. A common mistake is over-writing the decimal places which will cause a FORTRAN floating-point exception with the message "ieee_invalid _flag" displaying in the terminal.

sourcespn.in:

```
       694
 60.178000         19.993600            -0.01
1
1 1   pick1.pn
 50.965300         12.572100            -0.20
1
1 1   pick2.pn
 49.879700          7.546700            -0.62
1
1 1   pick3.pn
 63.929500         38.285300            -0.05
1
1 1   pick4.pn
...
 49.438900         14.192300            -0.38
1
1 1 pick694.pn
```

The first line in *sourcespn.in* lists the total number of "sources" (now stations) to be read in from this file. The next line lists the station's latitude, longitude, and depth [km, -up]. After that is the count of picks files associated with this station and then a line that reads "following the first ray path sequence in *obsdata.in*, this is the first type of ray path being assigned and can be read in from *pick1.pn*". The information is somewhat redundant given our set-up but exists to allow for more complicated input configurations. Each station lists these three lines.

pick1.pn:

```
680
 57.578800      7.394200         0.00       106.07    0.15
 57.432300     21.413400         0.00        47.83    0.15
 67.780000     15.183500        10.00       114.45    0.15
 59.340900     27.200100         0.00        61.92    0.15
 ...
```

```
67.058500      20.941300          0.00        102.38     0.15
```

For the above example *pick1.pn* file, the first line lists the total number of events to be read in. Each line after constitutes an event recorded at the station for which the pick file corresponds. The information then lists the event latitude, longitude, depth [km, +down], trave time [s], and an estimate of uncertainty [s]. We give an uncertainty of 0.15 s for all ISC picks as a reasonable estimate. The ISC does not publish uncertainty values.

A.3 Documentation: grid3dg.in

Overview: The goal of this documentation is to provide context for our chosen input values to *grid3dg.in*.

Model Parametrization in FMTOMO

FMTOMO's model space is composed of sub-horizontal layers separated by interfaces. For a Pn tomography problem we are only interested in the crust and upper mantle as layers bounded by interfaces for the surface, the Moho, and a lower limit. The resolution of the model is defined by the inversion grid *vgrids.in* which is iteratively updated with the FMTOMO function *invert3d*. For the forward traveltime prediction, a propagation grid *propgrid.in*, discretely samples *vgrids.in* and so is necessary to maintain a finer resolution than *vgrids.in*. Executing *grid3dg* in the presence of *grid3dg.in* will produce FMTOMO input files *vgrids.in*, *interfaces.in*, and *propgrid.in*.

For the model volume, there is only ever one propagation grid, but the velocity grid of any given layer spans the whole model space. This means no discontinuities in the velocity grid if an interface is inverted-for and updates to a new depth. In our inversion scheme, we do not invert for any interface or parametrize the layer resolutions uniquely. Therefore, our *vgrids.in* for layers one and two is redundant

grid3dg.in (annotated)

```
ccccccccccccccccccccccccccccccccccccccccccccccccccccccccccccccc
c Specify number of layers (= number of interfaces -1)
ccccccccccccccccccccccccccccccccccccccccccccccccccccccccccccccc
2                       c: Number of layers in model
1                       c: Number of vel grid types(1 or 2)
0.2                     c: Pinchout distance (km) (>=0.0)
vgrids.in               c: Output velocity grid file
interfaces.in           c: Output interface grid file
-12325                  c: Seed random number generation (int)
0.20                    c: Minimum permitted velocity (km/s)
```

From the above parameter block, we define our two layers (the crust and upper mantle) and only invert for one velocity field type ("type 1", V_P). P- and S-wave velocity fields are calculated

separately to facilitate phase conversions (e.g., SmP). Subsequent lines are self-explanatory from the comments.

```
ccccccccccccccccccccccccccccccccccccccccccccccccccccccccccccccccc
c Set 3-D grid size and location. Note that all layer
c velocity grids have the same spatial dimension, but can
c have different node densities. Interface grids have the
c same node distribution.
ccccccccccccccccccccccccccccccccccccccccccccccccccccccccccccccccc
5    -195.0       c: Radial range (top-bottom) of grid (km)
86   48      c: Latitudinal range (N-S) of grid (degrees)
-38   42    c: Longitudinal range (E-W) of grid (degrees)
6371.0               c: Earth radius
```

This above parameter block defines the model volume. All source-receiver pairs must be contained within the model volume. "5" km above the surface of the Earth was chosen to be sufficiently encompassing of stations at elevation. Pn rays in FMTOMO also travel deeper than a first-order mantle headwave, so "-195" km was selected. The ranges for longitude and latitude were determined based on our data distribution. Boundary inputs are (left) north-most, (right) south-most, next line (left) west-most, and (right) east-most. Negative-west values are consistent throughout FMTOMO.

```
ccccccccccccccccccccccccccccccccccccccccccccccccccccccccccccccccc
c Set up propagation grid file
ccccccccccccccccccccccccccccccccccccccccccccccccccccccccccccccccc
propgrid.in           c: Name of propagation grid file
26    381    401        c: Number of points in rad lat, long
5     10             c: Refine factor & no. of local cells
0.04                 c: Cushion factor prop grid (<<1)
```

Line one of the above block lists the filename *propgrid.in*, generated in *grid3dg.in* for consistency. You will likely not need to edit the *propgrid.in* file. The grid size ratio for "rad, lat, and long" of the propagation grid should be ~1 and finer resolution than the *vgrids.in* (next parameter block). A ratio ~1 is especially difficult to achieve in polar regions, but greatly improves the success of the forward solver. In the output file *arrivals.dat* (generated from *fm3d*), rays that fail display a "-1" for their travel times. Prior to implementing this, 40 - 50% of our rays were failing while after only ~5% failed. Dicing the radial range into 26 nodes yields a vertical length of 8 km;

(195 - -5)/(26-1) = 8. You subtract 1 from the denominator because one of the nodes is an end point. It is not necessary to keep distances as whole integers but we do for reporting consistency. Latitude distances do not change with respect to longitude, so 38° of coverage with "381" points equally dices into 0.1° or 11 km spaced nodes. Longitude however varies significantly with latitude. For the 50 – 72° latitude range, 0.2° grid node spacing for longitude varies from 15 – 7 km respectively. The refinement numbers describe a local set of finer grid nodes about the source. For ±"10" global grid cells, each divide into "5" local cells. Across three dimensions, that equals (5 * 10 * 2)^3 = 1,000,000 refined grid points. For faster testing, we have also used values of 5 and 5. The refinement numbers and cushion factor we inherit from the manual.

```
ccccccccccccccccccccccccccccccccccccccccccccccccccccccccccccccc
c Set velocity grid values layer 1
ccccccccccccccccccccccccccccccccccccccccccccccccccccccccccccccc
21          12          c: Number of radial grid points (type1&2)
77          12          c: Number of grid points in theta (N-S)
161          12          c: Number of grid points in phi (E-W)
0                       c: Use model (0) or constant gradient (1)
P                       c: Use P or S velocity model
stitch.vel               c: Velocity model (option 0)
3                       c: Dimension of velocity model(1=1-D,3=3-D)
5.4        3.0          c: Velocity at origin (km/s) (option 1)
7.0        5.0          c: Velocity at max depth(option 1)
```

The above parameter block defines *vgrids.in* with a resolution of 0.5° x 0.5° x 10 km. This is consistent with courser resolution than the propagation grid. The "type 2" values are not read in but exist for FMTOMO's text delimiters. We activate the switch for using a starting model by entering the value of 0 on line four and will use a 3D starting velocity model *stitch.vel*. For the layer-two velocity, we will enter the same inputs as all the above.

```
ccccccccccccccccccccccccccccccccccccccccccccccccccccccccccccccc
ccccccccccccccccccccccccccccccccccccccccccccccccccccccccccccccc
c Now, set up the interface grids
ccccccccccccccccccccccccccccccccccccccccccccccccccccccccccccccc
ccccccccccccccccccccccccccccccccccccccccccccccccccccccccccccccc
381                     c: Number of grid points in theta (N-S)
801                     c: Number of grid points in phi (E-W)
ccccccccccccccccccccccccccccccccccccccccccccccccccccccccccccccc
c Set up interface grid interface 1
```

```
ccccccccccccccccccccccccccccccccccccccccccccccccccccccccccccccccccccc
0                c: Obtain grid from external file (0=no,1=yes)
interface1.z          : External interface grid file (option 1)
4.8                    c: Height of NW grid point (option 0)
4.8                    c: Height of NE grid point (option 0)
4.8                    c: Height of SW grid point (option 0)
```

After all the velocity layers, the interface parameters are defined. All the interfaces contain the same x-y number of grid nodes. We determined that number from the resolution of our Moho input model (0.1 x 0.1°), which is read in as an external file for interface-two. Both the upper and lower interfaces must be set within the *vgrids.in* boundaries defined above.

A.4 Documentation: moho.int

Overview: The goal of this documentation is to explain how to design the input file *moho.int* for FMTOMO.

FMTOMO pseudocode

```
DO i=0,nvt+1
    DO j=0,nvp+1
        READ interface depth value
    ENDDO
ENDDO
```

It is important to understand how FMTOMO reads in the interface files to determine how to re-grid an input model. The above pseudocode block comes from the FMTOMO manual. It reads that there is only one interface depth value per line, and the value at i = j = 1 corresponds the southwestern corner; nvt and nvp are latitude and longitude counters respectively. Cushion nodes also need to be added when creating an externally read-in file. Generating an interface in *grid3dg.in* will automatically include them. Cushion nodes are simply an extra value placed the same grid node spacing from the edges of the model so it can update to the full extent.

moho_FMTOMO.m

Running *moho_FMTOMO.m* will produce the input interface file *moho.int*. The primary goal of this script is to read in interface geometry data and simply re-organize it to an FMTOMO readable format. We accomplish this by defining the same interface grid nodes used in *grid3dg.in*, adding cushion nodes, and re-gridding our chosen input model from Grad et al. (2009) with a linear interpolation function. Longitude values must be in degrees of east, and down is oriented negative.

```
%% moho_FMTOMO.m
%Read in Grad et al., (2009) Moho interface and regrid to FMTOMO format
%Model aviable at https://www.seismo.helsinki.fi/mohomap/
clear all;
```

```
%Text file with longitude, latitude, moho depth[km], uncertainty[km] in 0.1 x
    0.1 degree grid:
GRAD_moho = load('GRAD_moho.txt');
lon = GRAD_moho(:,1);
lat = GRAD_moho(:,2);
depth = GRAD_moho(:,3); %+[km]

%convert GRAD_moho longitudes into +/- degrees east
lon(lon >180) = lon(lon >180)-360;
%convert GRAD_moho depths to negative-down oriented values
depth = -1*depth;

%define a linear interpolation function, no extrapolation beyond model bounds
F_GRAD_moho=scatteredInterpolant(lat,lon,depth,'linear','none');

% Write the moho interface file:
ny=381; nx=801; % number of grid points in phi and theta in grid3dg.in
latlim=[48,86]; lonlim=[-38, 42];
% need to add cushion nodes
lat_diff=(latlim(2)-latlim(1))/(ny-1);
lon_diff=(lonlim(2)-lonlim(1))/(nx-1);
lat_i = [latlim(1)-lat_diff:lat_diff:latlim(2)+lat_diff];
lon_i = [lonlim(1)-lon_diff:lon_diff:lonlim(2)+lon_diff];

%Following the pseudo Fortran code for FMTOMO
fid_FMTOMO=fopen('FMTOMO_inputs/GRAD_moho.int','w+'); %FMTOMO output
fid_GMT=fopen('../GMT/GRAD_moho_gmt.txt','w+'); %output for plotting in GMT
for n_ny = 1:length(lat_i)
    for n_nx = 1:length(lon_i)
        depth_i = F_GRAD_moho(lat_i(n_ny),lon_i(n_nx));
        fprintf(fid_FMTOMO,'%10.5f\n',depth_i);
        fprintf(fid_GMT,'%10.5f %10.5f %10.5f\n',lon_i(n_nx),lat_i(n_ny),
           depth_i);
    end
end
fclose(fid_FMTOMO);
fclose(fid_GMT);
%save linear interpolant function
save("F_GRAD_moho","F_GRAD_moho");
```

A.5 Documentation: stitch.vel

Overview: The goal of this documentation is to detail creating our 3D reference velocity file *stitch.vel* for input to FMTOMO.

VsVp.m

All three of our reference velocity models are V_S structure which needs to be converted to V_P. To do this, we convert crustal velocities using the empirical relationship by Brocher (2005), and upper mantle velocities through depth dependent functions relating elastic parameters. Executing *VsVp.m* will produce linear interpolation functions for re-gridding in *Vp_stitch.m*.

```
%% VsVp.m
clear;

%% Read in Mauerberger et. al., (2022) Vs model and convert to Vp
%Model aviable at https://dataservices.gfz-potsdam.de/panmetaworks/showshort.
   php?id=b5a519b7-b65d-11ec-a8b4-7d2338b1cdf0
%longitude, latitude, depth (km), Vs (km/s)
BayHunterVSmean = load('BayHunter_VS_mean.xyz'); %model name
lon = BayHunterVSmean(:,1);
lat = BayHunterVSmean(:,2);
depth = BayHunterVSmean(:,3); %(+)0-400km
vs = BayHunterVSmean(:,4); %[km/s]

load('F_GRAD_moho.mat'); %Moho interface function from moho_FMTOMO.m
%lat,lon(+/-deg East),-depth [km]

%SubContinental Mantle Lithosphere (SCLM)
load('SCLM_functions.mat','F_Vs_to_VpVs');
%function made with convert_perplex_to_lookup
F_Vs_to_VpVs.ExtrapolationMethod = 'boundary';

for i = 1:length(vs)
    if depth(i) < abs(F_GRAD_moho(lat(i),lon(i))) %crust
        %Empirical relationship from Brocher (2005)
        vp(i,1) = 0.9409 + 2.0947*vs(i) - 0.8206*vs(i)^2 + 0.2683.*vs(i)^3 -
            0.0251.*vs(i)^4;
        %Brocher relationship is olnly valid for crustal rocks w/ Vs<4.5km/s
        if vs >4.5
            disp('alarm!'); break;
        end
    else %SCLM
```

```
        Vp_VsRatio = F_Vs_to_VpVs(depth(i),vs(i)); % (+[km], [km/s])
        vp(i,1) = Vp_VsRatio*vs(i);
    end
end
F_Vp_Mauerberger = scatteredInterpolant(lat,lon,depth,vp,'linear','none');
%save linear interpolant function
save("F_Vp_Mauerberger","F_Vp_Mauerberger");

%% Read in Celli et al., (2021) Vs model and convert to Vp
%Model aviable at https://nlscelli.wixsite.com/ncseismology/copy-of-af2019
clear;

NAT2021_file = importdata('NAT2021_vsvp.txt', ' ' ,1); %remove file header
%[lon lat depth Vp_abs Vp_ref dVp Vs_abs Vs_ref dVs]
NAT2021 = NAT2021_file.data; %model name
lon = NAT2021(:,1);
lat = NAT2021(:,2);
depth = NAT2021(:,3);
%(+)[0:1:20 25:5:60 70:10:100 120:20:660], but variable laterally & vertically
vs = NAT2021(:,7)./1000; %[m/s]->[km/s]

load('F_GRAD_moho.mat'); %Moho interface function from moho_FMTOMO.m
%lat,lon(+/-deg East),-depth [km]

%SubContinental Mantle Lithosphere (SCLM)
load('SCLM_functions.mat','F_Vs_to_VpVs');
%function made with convert_perplex_to_lookup
F_Vs_to_VpVs.ExtrapolationMethod = 'boundary';

%cull to model values w/in my region, otherwise F_Vp_Celli calls will be huge
%get these bounds from grid3dg.in
depthlim = 210; %adding +/-15km buffers
latlim=[46 88]; %adding +/- 2deg buffers
lonlim = [-40 44]; %adding +/- 2deg buffers
cull = zeros(length(lat),1);
cull(lat < latlim(1) | lat > latlim(2) | lon < lonlim(1) | lon > lonlim(2) |
   depth > depthlim)=1;
cull=logical(cull);
lat(cull) = []; lon(cull) = []; depth(cull) = []; vs(cull) =[];

for i = 1:length(vs)
    if rem(i,20000)==0
      disp(['working on ',num2str(i),' of ',num2str(length(vs))]);
    end
    if depth(i) < abs(F_GRAD_moho(lat(i),lon(i))) %crust
        %Empirical relationship from Brocher (2005)
```

```
        vp(i,1) = 0.9409 + 2.0947*vs(i) - 0.8206*vs(i)^2 + 0.2683.*vs(i)^3 -
            0.0251.*vs(i)^4;
        %Brocher relationship is olnly valid for crustal rocks w/ Vs<4.5km/s
        if vs >4.5
            disp('alarm!'); break;
        end
    else %SCLM
        Vp_VsRatio = F_Vs_to_VpVs(depth(i),vs(i)); % (+[km], [km/s])
        vp(i,1) = Vp_VsRatio*vs(i);
    end
end
F_Vp_Celli=scatteredInterpolant(lat,lon,depth,vp,'linear','none');
%save linear interpolant function
save("F_Vp_Celli","F_Vp_Celli");

%% Read in Zhu et al., (2015) Vs model and convert to Vp
%Model aviable in the Supplemental data at: https://academic.oup.com/gji/
   article/201/1/18/724841#86405283
clear;

%Long(deg) / Lat(deg) / Depth(km) / Iso Vp(km/s) / Iso Vp perturbation(%) /
% Iso Vs(km/s) / Iso Vs perturbation(%) / radial anisotropy / Q value /
EU60 = load('ZMODEL_M60.dat'); %model name
lon = EU60(:,1);
lat = EU60(:,2);
depth = EU60(:,3); %(+)[km]
vs = EU60(:,6); %[km/s]

load('F_GRAD_moho.mat'); %Moho interface function from moho_FMTOMO.m
%lat,lon(+/-deg East),-depth [km]

%SubContinental Mantle Lithosphere (SCLM)
load('SCLM_functions.mat','F_Vs_to_VpVs');
%function made with convert_perplex_to_lookup
F_Vs_to_VpVs.ExtrapolationMethod = 'boundary';

%cull to model values w/in my region, otherwise F_Vp_Zhu calls will be huge
%get these bounds from grid3dg.in
depthlim = 210; %adding +/-15km buffers
latlim=[46 88]; %adding +/- 2deg buffers
lonlim = [-40 44]; %adding +/- 2deg buffers
cull = zeros(length(lat),1);
cull(lat < latlim(1) | lat > latlim(2) | lon < lonlim(1) | lon > lonlim(2) |
   depth > depthlim)=1;
cull=logical(cull);
lat(cull) = []; lon(cull) = []; depth(cull) = []; vs(cull) =[];
```

```
for i = 1:length(vs)
    if depth(i) < abs(F_GRAD_moho(lat(i),lon(i))) %crust
        %Empirical relationship from Brocher (2005)
        vp(i,1) = 0.9409 + 2.0947*vs(i) - 0.8206*vs(i)^2 + 0.2683.*vs(i)^3 -
            0.0251.*vs(i)^4;
        %Brocher relationship is olnly valid for crustal rocks w/ Vs<4.5km/s
        if vs >4.5
            disp('alarm!'); break;
        end
    else %SCLM
        Vp_VsRatio = F_Vs_to_VpVs(depth(i),vs(i)); % (+[km], [km/s])
        vp(i,1) = Vp_VsRatio*vs(i);
    end
end
F_Vp_Zhu = scatteredInterpolant(lat,lon,depth,vp,'linear','none');
%save linear interpolant function
save("F_Vp_Zhu","F_Vp_Zhu");
```

FMTOMO pseudocode

```
DO i=0,nvr+1
    DO j=0,nvt+1
        DO k=0,nvp+1
            READ velocity value
        ENDDO
    ENDDO
ENDDO
```

The above pseudocode block comes from the FMTOMO manual. It reads that there is only one velocity value per line and the value at i = j = k = 1 corresponds the bottommost-southwestern corner; nvr, nvt, and nvp are radius. latitude, and longitude counters respectively. Cushion nodes will also need to be added when reading in external files.

Vp_stich.m

Running *Vp_stitch.m* will produce the FMTOMO input-file *stitch.vel* from the three linear interpolation functions output from *VsVp.m* by:

a. Defining the *grid3dg* space and add cushion nodes

b. Defining individual model boundaries (lateral and vertical)

c. Designing a logic tree to appropriately determine stitched model values

d. Applying a Gaussian smooth function across model boundaries

e. Outputing according to FMTOMO pseudocode

```
%% Vp_stitch.m
clear;
load("F_Vp_Mauerberger.mat");
load("F_Vp_Celli.mat");
load("F_Vp_Zhu.mat");
%input format: lat, lon, (+)depth; output: Vp [km/s]
%% grid3dg input
depthlim = [-195 5];
latlim=[48 86];
lonlim = [-38 42];
nx = 161; ny = 77; nr = 21; % number of grid points phi, theta, r

% need to add cushion nodes
lat_diff=(latlim(2)-latlim(1))/(ny-1);
lon_diff=(lonlim(2)-lonlim(1))/(nx-1);
depth_diff=(depthlim(2)-depthlim(1))/(nr-1);
lat_i = [latlim(1)-lat_diff:lat_diff:latlim(2)+lat_diff];
lon_i = [lonlim(1)-lon_diff:lon_diff:lonlim(2)+lon_diff];
depth_i = [depthlim(1)-depth_diff:depth_diff:depthlim(2)+depth_diff]; %(-down)

%% Define the stitiching_m
%the "patch" is the 2D extent of interpolated model
%the depth index 21 is chosen arbitratily witihin the interpolated volume
for n_ny = 1:length(lat_i)
        for n_nx = 1:length(lon_i)
            patch(n_ny,n_nx) = F_Vp_Mauerberger(lat_i(n_ny),lon_i(n_nx),-1.*
                depth_i(21));
        end
end

%stitching is defined to be +2 grid cells (0.5x0.5deg) about the patch border
%stitch will not work on the boundaries of grid i.e. x,y = 1,1 or end,end
stitching_m = zeros(size(patch));
for y = 1:size(patch,1)
    for x = 1:size(patch,2)
        if x>2 && x<size(patch,2)-1 %endcase
```

```
            if y>2 && y<size(patch,1)-1 %endcase
                if isnan(patch(y,x)) && (isnan(patch(y,x-1))==false ||  isnan(
                    patch(y,x+1))==false) %left and right case
                     stitching_m(y,x-2:x+2) = 1;
                elseif isnan(patch(y,x)) && (isnan(patch(y-1,x))==false ||
                    isnan(patch(y+1,x))==false) %down and up case
                     stitching_m(y-2:y+2,x) = 1;
                end
            end
        end
    end
end
%QDP figure showing the stitch, SW corner of my region
heatmap((stitching_m(:,85:end)));
stitching_m = logical(stitching_m);

%% Define the stitiching_c
%the "patch" is the 2D extent of interpolated model
%the depth index 19 is chosen arbitratily witihin the interpolated volume
for n_ny = 1:length(lat_i)
        for n_nx = 1:length(lon_i)
            patch(n_ny,n_nx) = F_Vp_Celli(lat_i(n_ny),lon_i(n_nx),-1.*depth_i
                (19));
        end
end
figure; %QDP of Celli Vp value "patch" extent in SW corner of my region
heatmap((patch(:,85:end)));

%Celli's model curves at its model boundary extent
%MATLAB's linear interpolation function fails to NOT extrapolate beyond the
%curve, the following is a brutish mask to delete the extraneous values
%which produce weird oscillations
x = [1 6.5 18.5 23.5 26 35 40]-2; %read from Celli lon plot values
y = [43.5 51.5 61.5 63 64 65.5 67.5]; %read from Celli lat plot values
a = polyfit(x,y,2);
x = linspace(1,42,79);
y = polyval(a,x); %approximated boundary curve

l1 = meshgrid(lat_i(1):lat_diff:lat_i(end)); %all lat "nodes"
l2 = meshgrid(lon_i(85):lon_diff:lon_i(end)); %all lon "nodes"

figure; %QDP of "nodes"/"values" in/out of boundary curve
plot(x,y,'g','LineWidth',2); %approximated boundary curve
hold on;
plot(l2,l1','k.'); %all "nodes"
```

```
coneofsilence = zeros(size(patch));
for i = 1:length(l1)
    for j = 1:length(l2)
        if  l1(j,i) < y(j)
            plot(l2(i,j)-2,l1(j,i),'b*'); %visualize "out of curve" nodes
            coneofsilence(i,j+84) = 1; %write "out of curve" nodes to var
        end
    end
end
coneofsilence = logical(coneofsilence);
patch(coneofsilence)= NaN; %delete "out of curve" "grid nodes" from patch

%stitching is defined to be +2 grid cells (0.5x0.5deg) about the patch border
%stitch will not work on the boundaries of grid i.e. x,y = 1,1 or end,end
stitching_c = zeros(size(patch));
for y = 1:size(patch,1)
    for x = 1:size(patch,2)
        if x>2 && x<size(patch,2)-1 %endcase
            if y>2 && y<size(patch,1)-1 %endcase
                if isnan(patch(y,x)) && (isnan(patch(y,x-1))==false ||  isnan(
                   patch(y,x+1))==false) %left and right case
                    stitching_c(y,x-2:x+2) = 1;
                elseif isnan(patch(y,x)) && (isnan(patch(y-1,x))==false ||
                   isnan(patch(y+1,x))==false) %down and up case
                    stitching_c(y-2:y+2,x) = 1;
                end
            end
        end
    end
end


figure;%QDP figure showing the stitch, SW corner of my region
heatmap((stitching_c(:,85:end)));
stitching_c = logical(stitching_c);

%% Define the quiltpatch_m
%goal is to not have a model's sittching inside another model's region
stitching = stitching_c +stitching_m;
figure; %QDP figure showing the combined stitch, SW corner of my region
heatmap((stitching(:,85:end)));

%order of velocity value assignment is as follows:
%1)F_Vp_Mauerberger 2)F_Vp_Celli 3)F_Vp_Zhu
%need to remove stitching_c from the Mauerberger model region
```

```
%the following is a brutish mask to define the Mauerberger model region
%w.r.t the MATLAB indexing values associated with lat/lon
quiltpatch_m = zeros(size(patch));
x1 = [10 10 10 9 9 9 8 8 8 7 7 7 6 6 7 8 9 10 12 13 14 15 16 17 19 21 24
    26]+84;
x2 = [32 35 38 41 43 46 49 52 52 53 53 53 54 54 54 55 55 56 56 57 57 57 57 57
    57 57 57 57]+84;
y = [19 20 21 22 23 24 25 26 27 28 29 30 31 32 33 34 35 36 37 38 39 40 41 42
    43 44 45 46];

k = 1;
for i =1:(size(patch,1))
    if k<=length(y) & i ==y(k)
        clearspaces = linspace(x1(k),x2(k),x2(k)-x1(k)+1);
        quiltpatch_m(y(k),clearspaces) = 1;
        k= k+1;
    end
end
figure; %QDP figure showing the quiltpatch_m, SW corner of my region
heatmap((quiltpatch_m(:,85:end)));
quiltpatch_m = logical(quiltpatch_m);
%Delete quitlpatch from stitching
stitching_c(quiltpatch_m)=0;
figure; %QDP figure showing the new Celli stitch, SW corner of my region
heatmap((double(stitching_c(:,85:end))));

%% vel stitch output
fid_vel_gmt=fopen('../GMT/vel_stitch_gmt.xyz','w+'); %GMT plotting output
fid_vel=fopen('FMTOMO_inputs/stitch.vel','w+');
%Following the pseudo Fortran code for FMTOMO
%The functions will only return interpolated values within the model
%volume, so "if NaN" logic can be interpretted as moving to the next model
%region in the heirarchy scheme
for n_nr = 1:length(depth_i) %depth loop
    disp(depth_i(n_nr));
    for n_ny = 1:length(lat_i) %lat loop
        for n_nx = 1:length(lon_i) %lon loop
            vel = F_Vp_Mauerberger(lat_i(n_ny),lon_i(n_nx),-1.*depth_i(n_nr));

            if isnan(vel) %patch w/ Celli
                vel = F_Vp_Celli(lat_i(n_ny),lon_i(n_nx),-1.*depth_i(n_nr));
                if coneofsilence(n_ny,n_nx) %if outside model curve boundary
                    vel = NaN;
                end
            end
```

```
        if isnan(vel) %patch w/ Zhu
            vel = F_Vp_Zhu(lat_i(n_ny),lon_i(n_nx),-1.*depth_i(n_nr));
        end

        %depth fixes
        if depth_i(n_nr)==-5 %%depth patch, Zhu tops out at -10, cast up
            if isnan(vel)
                vel = F_Vp_Zhu(lat_i(n_ny),lon_i(n_nx),-1.*depth_i(n_nr-1)
                    );
            end
            vel_depth_slice_top(n_ny,n_nx) = vel;
        end
        if depth_i(n_nr)>=-5
            vel_depth_slice = vel_depth_slice_top; %cast up "-15km" values
            stitching = stitching + stitching_c;
        else
            vel_depth_slice(n_ny,n_nx) = vel;
            if isnan(vel)
                disp('still have NaNs :(');
            end
        end
    end
end
%QDP figure showing the combined stitch, SW corner of my region
figure(1);
stitching = logical(stitching);
heatmap(double(stitching(:,85:end)));

%QDP figure showing the combined but un-stitched velocity values, SW
   corner of my region
figure(2);
surf(l2,l1',vel_depth_slice(:,85:end));
view(2);
colormap default;
colorbar;

%Gaussian stitch
thread_vel = NaN(size(stitching));
thread_vel(stitching) = vel_depth_slice(stitching);
%2D Gaussian smooth function across 1.5deg (0.75degrees on each side)
needle_vel = smoothdata2(thread_vel,"gaussian",3,"omitnan");
vel_depth_slice(isnan(needle_vel)==false) = needle_vel(isnan(needle_vel)==
   false);

%QDP figure showing the stitched velocity values, SW corner of my region
figure(3);
```

```
    surf(l2,l1',vel_depth_slice(:,85:end));
    view(2);
    colormap default;
    colorbar;
    pause(2);

    %to output
    for n_ny = 1:length(lat_i)
        for n_nx = 1:length(lon_i)
            fprintf(fid_vel,'%10.5f\n',vel_depth_slice(n_ny,n_nx));
            fprintf(fid_vel_gmt,'%10.5f %10.5f %10.5f %10.5f\n',lon_i(n_nx),
               lat_i(n_ny),depth_i(n_nr),vel_depth_slice(n_ny,n_nx));
        end
    end
end
fclose(fid_vel_gmt);
fclose(fid_vel);
```

A.6 Documentation: obsdata.in

Overview: The goal of this documentation is to provide details for producing input files *sources.in*, *receivers.in*, and *otimes.dat* from the ISC data in */picks/*.

obsdata.in (annotated)

```
ccccccccccccccccccccccccccccccccccccccccccccccccccccccccccccccc
sources.in                c: Output source file
receivers.in              c: Output receiver file
sourcederivs.in           c: Output source derivative file
picks/                 c: Directory of input receiver files
1                         c: Number of input source files
1                         c: Extract traveltimes (0=no, 1=yes)
otimes.dat                c: File of extracted traveltimes
```

The comments in the above block are fairly self-explanatory. The output file names should remain consistent throughout. For every n-source input file, there needs to be n-parameter blocks. We only use one source file for our Pn sources. We set traveltimes to be extracted and produce the file *otimes.dat*. For the inversion, *invert3d* seeks to match these observed trvaltimes by minimizing their difference with the traveltimes produced by *fm3d*.

```
ccccccccccccccccccccccccccccccccccccccccccccccccccccccccccccccc
c first input source file and associated path information
ccccccccccccccccccccccccccccccccccccccccccccccccccccccccccccccc
sourcespn.in            c: Input source file
0                       c: Local (0) or teleseismic sources (1)
0                       c: Compute source derivatives(0=no,1=yes)
1                       c: Number of paths from these sources
3                       c: Number of path segments
c: Path sequence information plus velocity fields below
0 2   2 3    2 1
1     1      1
```

The above block corresponds to the n^{th} source file, *sourcespn.in*. We set all the sources as "local" meaning they must exist within the model volume space. The Pn raypath re-initializing in subsequent layers necessitates a local model design. More precise hypocenter location was not a goal for this project. Also, our sources and receivers are switched for faster computation.

From each "source" we define only one ray path, the Pn ray composed of three segments. In FMTOMO, that path sequence is described by the integer combination 02 23 21 with "type 1" (P-wave) velocities along each segment.

Understanding outputs: *sources.in*, *receivers.in*, and *otimes.dat*

Executing *obsdata* in the presence of *obsdata.in* and *sourcespn.in*, will produce the FMTOMO input files *sources.in*, *receivers.in*, and *otimes.dat*. Although it is usually unnecessary/ill-advised to manually edit these files, we have found it beneficial to understand their contents when troubleshooting why a particular run is giving unexpected results.

sources.in (with comments):

```
 694 | total # of "sources"
   0 |designates local source
-9.99999978E-03   60.1780014       19.9936008 | depth lat lon
   1    | # of paths
   3    | # of path-segments, path sequnce below
   0           2           2           3           2           1
   1           1           1      | path velocity type
   0
-0.200000003       50.9653015       12.5720997
   1
   3
   0           2           2           3           2           1
   1           1           1
   0
...
0
-0.379999995       49.4389000       14.1922998
   1
   3
   0           2           2           3           2           1
   1           1           1
```

receivers.in (with comments):

```
      169936    | total # of "receivers"
   0.00000000       57.5788002       7.39419985  | depth lat lon
```

```
           1    | # ray paths from source
           1    | corresponding source #
           1    | velocity type
   0.00000000       57.4323006       21.4134007
           1
           1
           1
   10.0000000       67.7799988       15.1835003
           1
           1
           1
...
0.00000000       51.4762993       16.0359001
           1
         694
           1
```

otimes.dat **(with comments):**

```
169936 |# of raypaths
1       1       1       0   106.070000      0.150000006
2       1       1       0   47.8300018      0.150000006
3       1       1       0   114.449997      0.150000006
...
169936     694       1       0   39.6899986      0.150000006
|ray-#, source-#, ray count-#, 0-normal path, time[s], error[s]
```

A.7 Documentation: frechgen.in & invert3d.in

Overview: The goal of this documentation is to provide details for making the FMTOMO input file *frechet.in* from *frechgen.in* and *invert3d.in*.

frechgen

Executing the FMTOMO function *frechgen* in the presence of *frechgen.in* and *invert3d.in* will produce the file *frechet.in* containing arguments for which Fréchet derivatives to solve for. FMTOMO designs this file generation with a two-factor switch. The primary "on/off" key is in *invert3d.in* since there is no point in spending computer power calculating partial derivatives for which there is no inversion paramter defined. The file *frechgen.in* offers further refinement in targeting specific layers.

frechgen.in:

```
invert3d.in          c: Input file invert3d
frechet.in           c: File specifying derivatives to fm3d
vgridsref.in         c: File containing refe velocity grid
sourcesref.in        c: File containing ref source locations
-1                   c: Velocity derivatives (>0=subset, -1=all)
1                    c: If all, type 1(1), type 2(2) or both(3)
2                    c: Indices of velocity grids (subset chosen)
1                    c: Velocity types in inversion (1 or 2)
1                    c: Interface derivatives (>0=subset, -1=all)
2                    c: Indices of interface grids (subset chosen)
-1                   c: Source derivatives (>0=subset, -1=all)
sourcederivs.in      c: File specifying sources in inversion
                      (subset chosen)
```

From the above paramter block, file names should remain consistent throughout. Following the primary-key switches in *invert3d.in* (listed as line one above and shown below), velocities are the only parameter inverted for. The above *frechgen.in* file instructs *fm3d* to solve for the velocity derivatives in all layers for "type-1" (P-waves). The subsequent velocity grid related lines are not invoked by selecting "all" on line five. The interface and source derivative related lines are also switched "off" in *invert3d.in*.

***invert3d.in*:**

```
ccccccccccccccccccccccccccccccccccccccccccccccccccccccccccccccccccccc
c This file contains all required input parameters and files
c to the inversion program "invert3d.f90"
ccccccccccccccccccccccccccccccccccccccccccccccccccccccccccccccccccccc
vgridsref.in                c: Reference velocity grid
vgrids.in                   c: Current velocity grid
interfacesref.in            c: Reference interface grid
interfaces.in               c: Current interface grid
sourcesref.in               c: Reference source coords
sources.in                  c: Current source coordinates
stimes.dat                  c: Current source time perturbations
receivers.in                c: Receiver coordinates
otimes.dat                  c: Observed traveltimes
mtimes.dat                  c: Model traveltimes
rtimesnec.dat               c: Reference teleseismic traveltimes
frechet.in                  c: Frechet derivative parameters
frechet.dat                 c: Frechet derivatives
inviter.in             c: File indicating current inversion step
propgrid.in            c: File containing propgrid parameters
0.07                   c: Minimum distance between interfaces(km)
0.5                    c: Minimum permitted velocity (km/s)
0            c: Remove mean from predicted teleseisms(0=no,1=yes)
1  1.0  1.0      c: Velocity inversion(0=no,1=yes),damp,smooth
0  0.5  0.02     c: Interface inversion(0=no, 1=yes),damp,smooth
0  1.0  1.0      c: Source inversion(0=no, 1=yes),damp1,damp2
20               c: Subspace dimension (max=50)
50.0             c: Global damping factor (epsilon)
1                c: Apply second derivative smoothing(0=no,1=yes)
50.0                    c: Global smoothing factor (eta)
6371.0                  c: Earth radius in km
```

The file *invert3d.in* mostly contains directory set-up information. The minimum distance, permitted velocities, and subspace dimensions are values recommended in the FMTOMO manual to keep *invert3d* from failing and save on computational cost. The mean-removal switch is never invoked because we do not read in any teleseismic events. We only set the velocity inversion switch to "on". The subsequent values on the velocity inversion line are the pre-multiplication damping and smoothing factors by the global values (i.e., 1.0 * 50.0,1.0 * 50.0). The global damping and smoothing values were determined through a series of data-model misfit curves. We also apply second derivative smoothing to make the objective function more stable.

***frechet.in* (with comments):**

```
1            | "yes" collect Frechet derivatives
2            | # of velocity grids to perform calculations
1      2     | layers id's
1      1     | velocity types
0            | # of interface grids to perform calculations
0            | # of source positions to perform calculations
```

A.8 Documentation: FMTOMO iterative solver

Overview: The goal of this documentation is to provide an overview of input files needed to iteratively execute the inversion scheme in FMTOMO with shell script *tm3d.sh*.

mode_set.in

```
F   file_mode
T   no_pp_mode
F   parallel_mode
F   display_mode
T   save_rays_mode
F   save_timefields_mode
```

The file *mode_set.in* allocates memory storage. Full descriptions can be found in the FM-TOMO manual, but essentially *no_pp_mode* performs ray tracing for an individual source and once complete de-allocates said memory from RAM. Toggling on *save_rays_mode* produces the *file rays.dat* at not much greater computational cost, and is useful for visualizing how and where rays are propagating.

tomo3d.in

```
5
0
0

In order we have
c: Number of inversion iterations
c: Begin from starting model (0) or current iteration (1)
c: If above equals 1, then start with inversion (0) or forward
   step (1)
```

The file *tomo3d.in* prescribes the number of inversion iterations to perform and from which starting point. Determining an appropriate number of iterations to perform was done by looking in the file *residuals.dat* (shown below) and determining after which iteration no significant changes to the model are made. The only instance to switch line two to "1", is if you have run five-inversions and want to perform more without re-running those five.

residuals.in

```
otimes.dat                    c: Observed times
mtimes.dat                    c: Model times
sourcesref.in                 c: Source file
rtimesnec.dat                 c: Reference teleseismic times
invert3d.in                   c: Inversion parameters
                                (indicates yes/no mean is
                           to be removed from teleseismic
                           traveltimes)
```

The file *residuals.in* lists the file names used in calculating travel time residuals and should remain consistent throughout. Executing the command *residuals* in the presence of *residuals.in* will produce *residuals.dat*. Given our model design, the last three parameters in *residuals.in* are read over.

residuals.dat

```
1724.81 2.97497 132.22021
1159.03 1.34337 59.70489
1071.02 1.14709 50.98159
1058.14 1.11966 49.76241
1050.64 1.10386 49.05995
1044.41 1.09080 48.47983
```

The output in *residuals.dat* are the root mean square "RMS", variance [s^2], and χ^2 between current model traveltimes *mtimes.dat* and the observed traveltimes *otimes.dat*. Six lines are output from the reference plus five subsequent iterations. From column two above, the overall reduction in data variance is 63.3%. Between iterations (rows) four and five, variance reduction is only 1.2%. It is important to check that the residuals are reducing significantly, otherwise the model is not updating. Failed rays do not contribute to these calculations.

tm3d.sh pseudocode

```
if starting with the forward solver:
        make reference files the current model (*ref.in to *.in)
        frechgen
```

```
                #produces frechet.in
        Iter_count = 1; print Iter_count >! Inviter.in
        fm3d >! fm3dlog.out
                #produces arrivals.dat, frechet.dat, and rays.dat
                cp arrivals.dat to mtimes.dat
        residuals >! residuals.dat
end

while Iter_count <= line-one tomo3d.in
        invert3d  >> tomo3d.output.txt;
            #updates vgrids.in
        fm3d >! fm3dlog.out
                #produces arrivals.dat, frechet.dat, and rays.dat
                cp arrivals.dat to mtimes.dat
        cp updated model files to directory: /Iter_count/
        residuals >> residuals.dat
        Iter_count++; print Iter_count >! Inviter.in
end
```

The shell script *tm3d.sh* runs the iterative forward and subsequent inversion process with input files contained in the *Run*-directory where *tm3d.sh* is located. *tm3d.sh* is a modified script of the general version *tomo3d* distributed with FMTOMO. It will also produce several output files helpful for troubleshooting.

tomo3d.output.txt

A successful inversion will produce the output: "PROGRAM invert successfully completed!!". An unsuccessful run will terminate *invert3d* and produce the following message:

```
Error termination. Backtrace:
#0  0x7f0c82215171 in ???
#1  0x7f0c82215d19 in ???
#2  0x7f0c82216521 in ???
#3  0x7f0c8241a288 in ???
#4  0x7f0c8241a58c in ???
#5  0x401edc in ???
#6  0x402692 in ???
#7  0x7f0c8167f7e4 in ???
#8  0x400b0d in ???
#9  0xffffffffffffffff in ???
Traceback (most recent call last):
 ...
```

Most often the line after "Traceback" will list a file name. This typically means that file was not located in the *Run*-directory as necessary.

```
PAUSE No convergence in svdcmp!
To resume execution, type go. Other input will terminate the job.
go
RESUMED
PAUSE No convergence in svdcmp!
To resume execution, type go. Other input will terminate the job.
go
RESUMED
PAUSE No convergence in svdcmp!
To resume execution, type go. Other input will terminate the job.
ctrl+C
>>
```

If the above message is output instead, we have found that no amount of "resuming execution" leads to a successful inversion. We receive this error from negative traveltimes in our *otimes.dat* file or by *arrivals.dat* having wildly divergent values. Negative values can happen when generating a purely synthetic travel time data set containing failed rays. In the instance where rays are propagating through a very low velocity medium (the FMTOMO manual identifies sedimentary basins and volcanic regions as examples), arrival times can near zero (or negative). This is supposed to be mitigated by the "minimum permitted velocity" value input to *inver3d.in*, but if the user has designed the velocity field in such a way, it may exacerbate the non-linearity of the inversion. From experience, prescribing an egregiously high amplitude spike test does this.

```
cp: cannot stat 'arrivals.dat': No such file or directory
At line 115 of file residuals.f90 (unit = 20)
Fortran runtime error: Cannot open file 'mtimes.dat': No such
   file or directory
Error termination. Backtrace:
. . .
```

Errors like the above message are a cascading failure from *fm3d* not producing the necessary *invert3d* input files. This requires looking through *fm3dlog.out* with typically the last line of the file able to identify the issue.

fm3dlog.out

fm3dlog.out is quite verbose and is intended to keep the terminal from clogging up. Generally, most of our failures can be attributed to local designated source/receiver positions existing outside the model volume. A successful run will end with "finished reading receivers". Tracing back the *tomo3d.output.txt* error from above, the final line in *fm3dlog.out* reads:

```
receiver     5998  does not lie in final time field of path     1
```

arrivals.dat

```
1      1      1      0      104.156948     F     F
2      1      1      0       47.630336     F     F
3      1      1      0      115.538278     F     F
...
5023     34      1      0       50.812884     F     F
5024     34      1      0       -1.000000     F     F
5025     34      1      0      144.106746     F     F
...
151127    621      1      0      100.818157     F     T
151128    621      1      0      103.684911     F     F
151129    621      1      0      100.440572     F     T
...
169934    694      1      0       42.327016     F     F
169935    694      1      0       42.551306     F     F
169936    694      1      0       40.084870     F     F
```

The file *arrivals.dat* is produced from the forward solver *fm3d*. It contains fields "raypath-#, source-#, ray-count, 0-meaning "normal path", time [s], logical-occurrence of diffraction, and logical-occurrence of a head wave. Failed rays output "-1" in column five. Counting the number of failed rays gives an indication of model performance. We find considerably less rays returning a "true" logic for containing a head wave as would be expected for Pn. However, given the complexity of the imposed Moho interface and 3D varying velocity structure, it is not too surprising most rays lack the conditions necessary to produce a first-order head wave.

A.9 Documentation: mprop

Overview: The goal of this documentation is to provide details for using the FORTRAN function *mprop* to determine the velocity model roughness and variance.

Compile *mprop.f90*

The FORTRAN function *mprop* does not come standard with the FMTOMO package. This code was sent by Nick Rawlinson to assist in making smoothing and damping parameter trade-off curves. To make *mprop.f90* executable, in the terminal type "gfortran mprop.f90 -o mprop".

mprop.in:

```
ccccccccccccccccccccccccccccccccccccccccccccccccccccccccccccccccc
vgrids.in                   c: Input file of velocity vertices
vgridsref.in                c: Reference velocity field
interfaces.in               c: File containing interface info
1                              c: Target layer
1    1    1                    c: Dicing level in r,theta,phi
6371.0                         c: Earth radius in km
```

Executing *mprop* in the presence of *mprop.in* and the above-listed input files will output model roughness and variance. *mprop* will need to be executed for each layer, and then the outputs weighted based on the respective number of nodes. Since both layers in the model contain the same *vgrids.in* spacing, we use a simple average. Dicing level increases the accuracy of the measurement, but we find that for larger *vgirds.in* this will tend to cause a floating-point error. Regardless the accuracy does not affect the overall shape of the trade-off curve. The output will appear in the terminal unless piped to a text file.

```
Model variance in (km/s)**2 is    4.3196772695190669E-003
Model roughness in (kms)**(-1) is    1.6943635581912348E-004
```

A.10 Documentation: Checkerboard Tests

Overview: The goal of this documentation is to provide details for generating a series of synthetic checkerboard tests.

Generating synthetic data

There are a couple of input files containing parameter blocks that need to be switched on/off to produce synthetic traveltimes.

```
ccccccccccccccccccccccccccccccccccccccccccccccccccccccccccccccccc
c Optionally apply checkerboard to layer 1
ccccccccccccccccccccccccccccccccccccccccccccccccccccccccccccccccc
1                       c: Add checkerboard (0=no,1=yes)
0.16                     c: Maximum perturbation of vertices
6                       c: Checkerboard size (NxNxN)
0                       c: Use spacing (0=no,1=yes)
ccccccccccccccccccccccccccccccccccccccccccccccccccccccccccccccccc
```

In *grid3dg_cb.in*, a variation of the *grid3dg.in* file (shown above), switch on "add checkerboard" for each layer. The maximum perturbation value we chose to be +/- 2% of ak135 at 60 km depth equal to 0.16 km/s (Kennett, 2005). Too large a value risks the assumption of local linearity. A good first approach is to determine your model's relative velocity change and stay within those bounds. For context, for us that approach produced a value of 0.2 for depths of ~70 km. The checkerboard "size" can be understood as 6 * (0.5° x 0.5° x 10 km). Activating "spacing" makes the checkerboard sparse.

Also, in the file *obsdata_cb.in* (a variation of *obsdata.in*), switch "extract traveltimes" to "off". The reason for this is we only want use the *obsdata* function to produce the files *sources.in* and *receievers.in*, the true data coverage. We will then use *synthdata* to write our "observed" traveltimes from the *arrivlas.dat* file generated by running *fm3d* through the checkerboard. Executing *synthdata* requires the input file *synthdata.in* in the *Run*-directory. In *synthdata.in*, we also add a data covariance value of 0.15 s similar to the ISC data used in the regular inversion.

synthdata.in:

```
arrivals.dat                c: Input observed times
0.15                        c: Data covariance (s)
otimes.dat                  c: Output file
sourcesref.in               c: Source file
rtimes.dat                  c: Reference teleseismic times
0.0                         c: DC offset to traveltimes
0                 c: Add noise to synthetic times(0=no,1=yes)
0.100             c: Standard deviation added noise(local)
0.077             c: Standard deviation added noise(teleseismic)
1                 c: Weight w/ standard deviation(1) or noise(2)
99827374                    c: Random seed noise generation
```

run_cbsyn.bash:

Following our directory set-up (see Figure A.1), executing *run_cbsyn.bash* will read in the necessary files and output the generated data to a *Run*-directory.

```
#!/bin/bash -vx
RootDir="/data/geo/seismo/Research/josh_pn"
BaseDir="$RootDir/run_tomo"
RunDir="$BaseDir/cb_syn3x3"

rm -rf $RunDir
[ ! -d "$RunDir" ] && mkdir "$RunDir"
cd $RunDir

#
cp "$BaseDir/grid3dg_cb.in" "$RunDir/grid3dg.in"
cp $BaseDir/moho.int $RunDir
cp $BaseDir/ak135.vel $RunDir
grid3dg # this produces vgrids.in, propgrid.in, interfaces.in

cp vgrids.in vgridsref.in
cp interfaces.in interfacesref.in

#
cp -r $RootDir/picks_switched_sm $RunDir/picks
cp $RunDir/picks/sourcespn.in $RunDir
cp "$BaseDir/obsdata_cb.in" "$RunDir/obsdata.in"
obsdata  # this creates sources.in ,and receivers.in

cp $RunDir/sources.in $RunDir/sourcesref.in

#
cp $BaseDir/frechgen.in $RunDir
```

```
cp $BaseDir /invert3d.in $RunDir
cp $BaseDir/mode_set.in $RunDir

frechgen
fm3d >& fm3dlog.out # this produces arrivals.dat
cp $BaseDir/synthdata.in $RunDir
```

Executing *run_cbsyn.bash* in your *Base*-directory will produce a *Run*-directory with synthetic traveltimes contained in *arrivals.dat*. Some rays will likely fail producing a "-1" traveltime in column-five of *arrivals.dat*. In the presence of "-1's", *synthdata* outputs "-100's" which breaks the inversion program. To mitigate this, we remove the failed rays in *arrivals.dat* and the source-receiver combination that produced them in *receivers.in* to maintain consistency with the ray-numbering count. We achieve this using the script *rm_failedrays.m* which produces the files *new_arrivals.dat* and *new_receivers.in*. After some simple file-edits *synthdata* is executed producing *otimes.dat*.

```
%% rm_failedrays.m
%cull -1's from arrivals.dat, update receivers.in accordingly
%load arrivals.dat manually as string array, no changes
%load receivers.in manually as string array, no changes
%determine -1 (failed ray) indexes
ar_idx = find(double(arrivals(:,5)) ==-1);

%% new_arrivals.dat
%rm arrivals at -1 indexes, shift column 1 numbers up one
k=1;
for i = 1: length(arrivals)
    if ~ismember(i,ar_idx)
        new_arrivals(k,:) = arrivals(i,:);
        new_arrivals(k,1)= k;
        k = k+1;
    end
end

%to output
fid=fopen('new_arrivals.dat','w+');
for i = 1:length(new_arrivals)
    fprintf(fid,'%6.0f%6.0f%6.0f%6.0f%15.6f    %s    %s\n',[new_arrivals(i,1),
        new_arrivals(i,2),new_arrivals(i,3),new_arrivals(i,4),new_arrivals(i
       ,5), new_arrivals(i,6),new_arrivals(i,7)]');
end
```

```
fclose(fid);
%% new_receivers.in
%rm receivors at -1 indexes (4 lines each)
%this may take a while
re_idx = ar_idx +1;
j = [1,2,3,4];
k=0;l=0;
for i = 1:length(arrivals)
    if ~ismember(i,ar_idx)
        new_receivers(k+j(1):k+j(4),1:3) = receivers(l+j(1)+1:l+j(4)+1,1:3);
        k= k+j(4);
    end
    l = l+j(4);
end

%to output
fid=fopen('new_receivers.in','w+');
for i = 1:length(new_receivers)
    if mod(i,4)==1
        if contains(new_receivers(i,3),'-') %miscellaneous patch for (-)lons
            fprintf(fid,'   %s       %s      %s    \n',[new_receivers(i,1),
               new_receivers(i,2),new_receivers(i,3)]');
        else
            fprintf(fid,'   %s       %s       %s    \n',[new_receivers(i,1),
               new_receivers(i,2),new_receivers(i,3)]');
        end
    else
        fprintf(fid,'   %9.0f \n',[new_receivers(i,1)]');
    end
end
fclose(fid);
%IMPT! need to go in and add '        #sources' to first line, rename file
```

(old) arrivals.dat

```
...
    17      1      1      0       47.394085     F     F
    18      1      1      0       83.535779     F     F
    19      1      1      0       -1.000000     F     F
    20      1      1      0       44.843258     F     F
    21      1      1      0       44.739182     F     F
    22      1      1      0       44.976802     F     F
...
```

new_arrivals.dat

```
...
    17      1      1      0      47.394085    F    F
    18      1      1      0      83.535779    F    F
    19      1      1      0      44.843258    F    F
    20      1      1      0      44.739182    F    F
    21      1      1      0      44.976802    F    F
...
```

The file *receivers.in* is somewhat lengthier with four lines per arrival. A quick line-count (in the terminal: "cat new_receivers.in | wc -l") should confirm this file has been correctly updated. That number should equal: (4 x number of rays) + 1. The "+1" is for the first line in *receivers.in* that should contain a value that matches the number of rays.

run_cbfinal.bash

The checkerboard inversion run-script is very simialr to the regular *run.bash* script. The main difference is that rather that reading in *~/picks/* and executing *obsdata*, the "observed" data comes from the synthetically generated *otimes.dat*. This must remain consistent with the counting in *receivers.in* to produce *arrivals.dat*, which can then be inverted for.

```
#!/bin/bash -vx
RootDir="/data/geo/seismo/Research/josh_pn"
BaseDir="$RootDir/run_tomo"
SynDir="$BaseDir/cb_syn3x3"
RunDir="$BaseDir/cb3x3"

rm -rf $RunDir
[ ! -d "$RunDir" ] && mkdir "$RunDir"
cd $RunDir

cp $BaseDir/grid3dg.in $RunDir # grid3dg w/no CB
cp $BaseDir/moho.int $RunDir
cp $BaseDir/ak135.vel $RunDir
grid3dg # this produces vgrids.in, propgrid.in, interfaces.in
cp vgrids.in vgridsref.in
cp interfaces.in interfacesref.in

#
```

```
cp $SynDir/sources.in $RunDir
cp $SynDir/receivers.in $RunDir
cp $SynDir/otimes.dat $RunDir
cp $RunDir/sources.in $RunDir/sourcesref.in

#
cp $BaseDir/frechgen.in $RunDir
cp $BaseDir /invert3d.in $RunDir
cp $BaseDir/mode_set.in $RunDir
cp $BaseDir/tomo3d.in $RunDir
cp $BaseDir/inviter.in $RunDir
cp $BaseDir/residuals.in $RunDir
cp $BaseDir/rms.py $RunDir
cp -r $BaseDir/gmtplot $RunDir

cp $BaseDir/tm3d.sh $RunDir
./tm3d.sh >& tomo3d.output.txt
```